Monitoring Earth Using the Software Defined Radio (SDR) Earth Imager

by

Radwan N. K. Sharif

B.Sc., University of Zawia, 1998

M.Sc., University of Tripoli, 2010

A Dissertation Submitted in Partial Fulfillment of the Requirements for the Degree of

DOCTOR OF PHILOSOPHY

in the Department of Mechanical Engineering

University of Victoria

Supervisory Committee

Monitoring Earth Using the Software Defined Radio (SDR) Earth Imager

by

Radwan N. K. Sharif

B.Sc., University of Zawia, 1998

M.Sc., University of Tripoli, 2010

Supervisory Committee

Dr. Rodney Herring, Main Supervisor
(Department of Mechanical Engineering, University of Victoria, BC, Canada)

Dr. Brad Buckham, Departmental Member
(Department of Mechanical Engineering, University of Victoria, BC, Canada)

Dr. Geoffrey Steeves, Outside Member
(Department of Physics & Astronomy, University of Victoria, BC, Canada)

Dr. Peter F. Driessen, Outside Member
(Department of Electrical and Computer Engineering, University of Victoria, BC, Canada)

Abstract

The ionosphere, which is the highest region of Earth's atmosphere, contains waves created from both space and Earth disturbances. The ionosphere is considered the largest sensor on Earth and has been the subject of study since the 1920s, primarily through the use of ionosondes. A Software Defined Radio (SDR) Earth Imager has been devised to obtain information about these Earth disturbances. This research is divided into four stages: 1) engineering of the SDR Earth Atmosphere Imager, 2) imaging of waves that exist within the ionosphere, 3) determining the location of the earth disturbance that created the waves, and 4) measuring the power of the ionospheric waves.

The Earth Imager device functions similarly to a camera by utilizing an antenna array to create images of the ionosphere and its waves. The radio wave, i.e., the carrier wave of the ionosphere information, is transmitted up through the atmosphere at a near-vertical incidence from the Earth's surface. It reflects off the ionosphere back down to the Earth's surface, where it is detected by an antenna array to produce a phase image of the ionosphere.

The proof of concept of the SDR Earth Imager occurred at the University of Victoria, Victoria, BC, Canada, and was initially constructed at the Dominion Radio Astrophysical Observatory (DRAO), Penticton, BC, Canada. From the DRAO data analysis, two types of waves were found: one with a constant frequency, possibly originating from power losses in transmission lines, and another with a single sharp spike, potentially caused by earthquakes or lightning.

Further experiments at the University of New Mexico, utilizing Long Wavelength Array (LWA-1 and LWA-SV) antennae arrays, served as a high-resolution radio wave camera. The datasets from the LWA-1 and LWA-SV sites provided results showing the wavevector directions of one set of ionospheric waves, i.e., the strongest sets of waves, which have a spatial frequency of 0.06 cycle/m. The wavevectors were used to identify the location of the generation of the ionospheric waves and, thus, the likely source of the disturbance.

This Ph.D. research thesis shows a correlation between the waves in the ionization layer and Earth's disturbing events, including man-made disturbances such as the electromagnetic radiation emitted by power lines and electrical grids, which generate waves within the ionosphere. Further, this research illustrated how the phase image, not the amplitude image, determined from Fourier

analysis is critical to characterizing these waves. The phase image enables the characterization of these waves by providing information about their phase shifts, frequencies, and wave vectors.

This research demonstrates a clear relationship between waves within the ionosphere and disturbing events occurring on Earth. One significant finding of this dissertation is the deduction that all power generated and consumed by humans is not completely dissipated but rather transformed and captured by the Earth's ionosphere. This fact may assist climate modelers in gaining a better understanding of climate change.

Table of Contents

List of Figures

List of Tables

Abbreviations

Acronym

AC	Alternating Current
DRAO	Dominion Radio Astrophysical Observatory
EUV	Extreme Ultraviolet
GPS	Global Positioning System
HF	High Frequency
IEC	International Electrotechnical Commission
LSL	LWA Software Library
LWA	Long Wavelength Array
LWA-SV	Long Wavelength Array At Sevilleta
PLE	Power Line Emission
PLHR	Power Line Harmonic Radiation
SDR	Software Defined Radio
SED	Storm-Enhanced Density
STFT	Short Time Fourier Transform
TEC	Total Electron Content,
TIDs	Traveling Ionosphere Disturbances
UViip	University of Victoria Ionospheric Imaging Project

Variables

Dx	Length of Rectangle
H_v	Virtual Height
C	Capacitance
d	Distance between plates
Δd	Change on Distance Between the Plates
A	Surface Area Illuminated on Ionosphere
Dy	Width of Rectangle
NmF2	F2-layer peak electron density
u and υ	Spatial Frequencies
Δd	Ionosphere Phase Shift

Greek Symbols

φ	Phase
$\Delta\varphi$	Phase Difference
L	Path Length of Radio Wave
C	Capacitance
K	Relative Permittivity
ϵ_0	Permittivity of Free Space
ΔC	Change in Capacitance
AC	Alternating Current
ΔV	Change in Voltage Across Capacitor
P	Initial Power of Wave
R	Radius of Traveling Wave

K	Relative Permittivity
Q	Maximum Electron Densities
ω_p	Plasma Frequency
λ	Wavelength
T	Period
f	Frequency
a(t)	Amplitude of Wave
ω	Angular Frequency of Wave
Δt	Phase Shift in Time
μ	Mass Density
k	Wavenumber
v	Wave Speed
c	Speed of Light
H_v	Virtual Height
fc	Critical Frequency
ϵ_0	Permittivity of dielectric
P	Power
I	Current
S	Power Density
A	Area of Plate
A_t	Antenna Array
r	Radius of Wave
Ic	Coupled Power
d(x)	Damping
Ir	Remaining Power
I_p	Proportional Power of Wave

Acknowledgments

My sincere gratitude goes to my Ph.D. advisor, Dr. Rodney Herring, for his guidance, encouragement, perceptive feedback, and constructive comments throughout my Ph.D. research journey.

I also wish to express my appreciation to Dr. Peter Driessen and Nicholas Bruce. Dr. Peter coordinated the DRAO and LWA data experiments and the Earth Imager processor.

Nicholas Bruce is the one who made several significant contributions by setting up the antennae masts and working with Dr. Stephen Harrison and myself in taking the measurements, particularly DRAO data. I would also like to thank Dr. Gokhun Tanyer, who took time out of his schedule to discuss the possibility of the innovation, and Dr. Ahmed Youssef, who answered my questions related to Earth Imager.

I would like to convey my sincere thanks to the funding sources of the Libyan government that made my doctoral studies feasible. I am also very thankful for the Natural Science and Engineering Research Council of Canada (NSERC) grants and the chance to participate in the User Support Program of LWA-1 and LWA-SV at the University of New Mexico.

I primarily want to express my heartfelt gratitude to my mother for her profound love, unwavering support, and constant encouragement throughout my life. I am also extremely grateful to my wife for always being patient and supportive during my Ph.D. study and to all my family for the beautiful times spent and their support, which always inspired and energized me to return to my studies. There are no adequate words to convey my love and gratitude for them.

Finally, I would also like to thank the doctors who make up my supervising committee and all committee members.

Chapter 1 Introduction

1.1 Introduction

The ionosphere is defined as a layer of particles in the atmosphere that become ionized due to solar radiation. It plays a critical role in radio communication and navigation systems, and its behavior is directly linked to space, weather, and climate.

This region holds significant importance as it acts as a sensitive terrestrial entity and serves as a mantle surrounding the Earth, making it a valuable tool for observing both terrestrial and space phenomena. It serves as a repository for diverse data types that hold significance for academic research and practical applications. It encompasses various important pieces of information, including electron density, total electron content, ionospheric waves, and space weather effects. Consequently, scientists have been studying the ionosphere since the 1920s using instruments called ionosondes[1], [2]. These instruments measure the ionosphere starting from an altitude of approximately 50 km up to over 500 km. The ionosphere region is divided into three layers: D, E, and F, which exhibit varying ionization densities based on factors such as solar radiation, time of day, seasons, and solar activity. This includes solar flares and solar winds- streams of charged particles that are emitted by the sun's corona [3].

Within the ionosphere, a variety of disturbances and waves can emerge. It is crucial to clarify the exact relationship between a disturbing event and its impact on the ionosphere. The association between meteorological events on Earth and the ionosphere has been extensively studied. Researchers have investigated different types of disasters in order to establish a connection between disturbing events and the resulting ionospheric responses. The literature extensively reports a potential link between ionospheric disturbances and meteorological phenomena, which supports the overarching hypothesis of meteorological influence. The surfaces of the ionization layers are not flat and can be disturbed by various factors, including solar activity, geomagnetic conditions, and meteorological states. For instance, Rishbeth explored the possibilities of different waves being generated by dynamic climate patterns and atmospheric storms [2].

Another instance, gravity waves can be generated by weather systems, atmospheric turbulence, or seismic activity. Moreover, the ionosphere can contain data pertaining to acoustic waves, also known as infrasound waves, which meteor impacts, volcanic eruptions, or other atmospheric

disturbances can produce. Furthermore, the ionosphere holds important information and data related to Travelling Ionospheric Disturbances (TIDs): TIDs are wave-like perturbations that can propagate horizontally through the ionosphere. Various factors, such as atmospheric waves, geomagnetic activity, and solar events, can cause them.

By imaging the ionosphere, researchers can gain insights into how space and Earth disturbances impact Earth's atmosphere. By utilizing Earth Imager technology, which enables flexible signal processing and waveform generation through software, designing a system capable of capturing and imaging ionospheric waves using an antenna array as a camera becomes feasible. An appropriately designed antenna system, including the optimal distances between antennas, is essential for effectively capturing ionospheric waves.

This thesis proposes a Software-Defined Radio Earth Imager that aims to capture information about ionospheric waves by utilizing radio signals transmitted through the atmosphere at near-vertical incidence from the Earth's surface. These signals are reflected off the ionosphere and received back on the Earth's surface, where the phase information is utilized to generate a phase image of the ionosphere using an antenna array camera. The processed data can further be used for generating images or visual representations of the ionospheric waves. Techniques such as tomographic reconstruction or mapping the received signals onto a two-dimensional grid can be employed for this purpose.

Using the Software Defined Radio, thesis focuses on measuring the phase shifts, frequencies, and wave vectors of the ionospheric waves and establishing their correlation with power, energy, and location of origination. Notably, the research also explores the correlation between the power generated and consumed by the largest nearby city, Albuquerque, with a strong, high-amplitude set of waves.

1.2 Problem Description

Research endeavors aimed at imaging ionospheric disturbances have been ongoing for many years, but tangible outcomes have yet to be achieved. Currently, numerous prominent research groups are dedicated to addressing this challenge. Scientists have extensively studied the interconnections between the responses of the atmosphere, the Earth, and the space-disrupting occurrences using different methods. One notable research endeavor that stands out was the approach utilizing ionosondes [4]. Ionosondes are instruments specifically designed to probe the

ionosphere and gather information about its characteristics at different altitudes. While ionosondes primarily provide measurements of ionospheric parameters, including electron density, electron temperature, and ion composition. They have also been used to visualize the ionosphere's structure and behavior. One commonly used imaging technique with ionosondes is called ionogram imaging.

Previous studies using ionosondes have demonstrated that ionospheric waves are generated by various events such as earthquakes, volcanic eruptions, hurricanes, tsunamis, solar flares, and other space events, including man-made disturbances. These disturbances create measurable waves within the ionization layers of the ionosphere [3]. Ionosondes have been able to detect those waves generated by these disturbances; however, they can only provide information about a single reflected point from the ionosphere and lack wave vector information necessary for determining the location of the disturbing event within the ionosphere.

Another notable research effort involves the use of weather balloons; however, weather balloons are not suitable for this approach because they can only reach a maximum altitude of approximately 53 km [5].

Another method would be to use multiple satellites to identify the ionization layers [6]. In addition, HF Doppler radar and Over the Horizon radar [6, 7] have succesfuly identified Rayleigh waves generated by earthquakes. The method (Doppler shift) measures earthquake signatures converted into the corresponding ground displacement by a transfer function. They provide a broader perspective on the topic of lithosphere-atmosphere-ionosphere-magnetosphere coupling and the potential generation of pre-earthquake signals. Nevertheless, Doppler imaging of radio wave formation has limited sensitivity. It can only detect disturbances greater than 7 Richter scale [7], and is unable to give enough information about the ionization layers and their corresponding disturbing events on the Earth.

One noteworthy endeavor is taking place at the LWA (Long Wavelength Array) observatory in New Mexico. LWA1 serves as the initial installation among a series of planned antenna arrays specifically designed for cosmic observation, comprises 256 phase-coherent dipole antennas. The size and capabilities of the LWA array offer promise in detecting and studying phenomena such as lightning discharges, atmospheric disturbances, and other geophysical events using long-wavelength radio waves [8].

The problem addressed in this study is the development and exploration of a straightforward method for imaging the ionosphere that should have the capability to depict the ionospheric waves and complements certain existing approaches. An ionospheric imager using SDR technology could provide the means to capture and observe various types of waves in the ionosphere making it possible to build an Earth Imager based imager having the capability to image waves existing in the ionosphere, as illustrated in Figure 1.1. An Software Defined Radio would allow for flexible and programmable processing of radio wave signals, making it suitable for capturing and manipulating the data necessary for ionospheric imaging.

An Earth Imager can expect to see various types of waves in the ionosphere. These waves might include gravity, planetary, and ionospheric disturbances caused by solar and meteorological phenomena. The specific types of waves that can be observed will depend on the frequency range and antenna configuration of the imager.

The characteristics of the waves imaged by the Earth Imager requires separating the varying waves of amplitudes, frequencies, and wavevectors. The amplitudes and frequencies of the waves provide information about their power and energy, respectively. The wavevectors, which represent the direction and magnitude of wave propagation, may also be determined from the imaged waves.

By imaging one set of waves at two different locations using parallax imaging, the SDR imager should be able to determine the location of an ionospheric disturbance. By comparing the wavevectors of the imaged waves at the two locations, it becomes possible to calculate the direction of the disturbance, thus determining its location.

The technology utilized in a radio wave camera to generate images includes Software Defined Radio (SDR) and GPS timing as shown in Figure 1.1. Earth Imager enables the flexible and programmable processing of radio wave signals, allowing for the capture and manipulation of data necessary for image generation. GPS timing provides precise synchronization and timestamping of the received signals, ensuring accurate spatial and temporal information for constructing the phase images. These technologies work in tandem to enable the functionality and image generation capabilities of a radio wave camera.

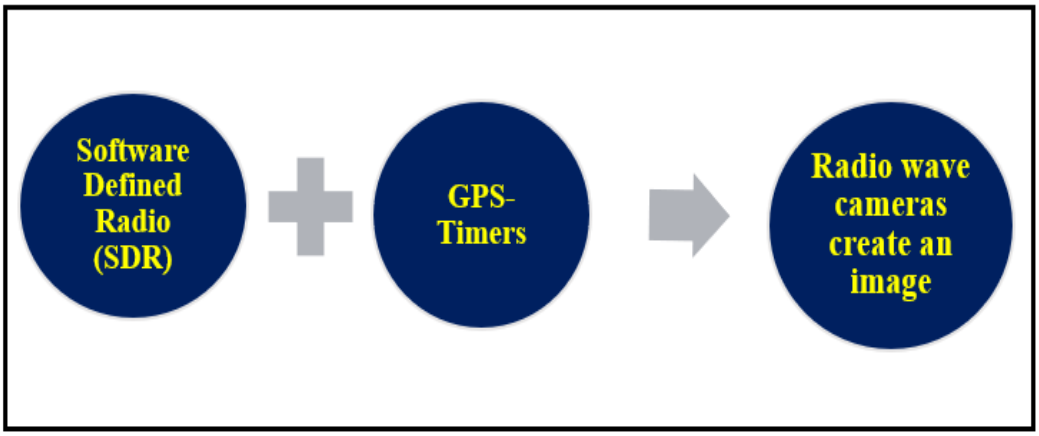

Figure 1.1 Software-defined radio with GPS timers making a Radio wave camera that creates an image.

1.3 Research Objective

The main objective of this research is to measure the phase shifts, frequencies, and wave vectors of the waves within the ionization layers and relate them to the physical events causing them. One of the key features of this thesis was to construct a radio wave transmitter and a two-dimensional array of passive receivers used to image the shape of the waves existing within the ionosphere. By doing so, the power, energy, direction of the wave motion, and location of creation could be determined.

Each antenna or receiver of the atmosphere Imager represents one pixel in its image. Due to the location of the array antenna, the reflected radio waves carrying information from the ionosphere reach different antenna locations at different times. The difference in the path and the time that a radio wave carrier takes from a transmitter to a receiver path is important to determine the phase shift between each emitted and received radio wave. The phase shift creates an image of the ionospheric waves. Each set of waves in a phase image will have a different frequency and wavevector and will thus be separated from each other using Fourier analysis, which produces a Fourier image. Based on antenna configurations, I intend to measure the relative phase information about the ionospheric waves. The energy of the ionospheric waves is directly proportional to their frequency. The power of these waves can be measured by the square of their phase shift. As a result, both power and energy are linked to height squared and frequency. Although power and energy are related to separate physical quantities, they are intimately connected through the

ionospheric wave's amplitude, i.e., its phase shift in the phase image and its frequency. Also, the unique direction of motion of the ionospheric wave will be measured by using two SDR Earth Imagers located at different places. A set of ionospheric waves with the same frequency has a different wave vector at the two locations whose crossover determines the location of the disturbance. Hence, for the analysis and interpretation of the data, the Fourier transform approach will be used to analyze the phase images. Measuring the properties of the waves existing within the ionization layers will help us learn more about meteorological events that can influence climate and weather conditions. Various approaches can be employed to measure the properties of waves on the surface of the ionization layer, including power, energy, direction of movement, and the location of atmospheric disturbances.

1.4 Research Motivation

The ionosphere can experience disturbances due to various geophysical phenomena. These disturbances can generate waves that propagate through the ionosphere. For example, geomagnetic storms, solar flares, and coronal mass ejections can cause ionospheric disturbances, resulting in waves such as ionospheric plasma waves or traveling ionospheric disturbances (TIDs). An ionospheric imager can capture these waves and provide insights into the dynamics and behavior of the ionosphere under such perturbations.

The SDR Earth Atmosphere Imager has been a research collaboration between the Mechanical (Professor Rodney Herring) and Electrical (Professor Peter Driessen) Engineering Departments at the University of Victoria. This research will use relatively new Earth Imager radio wave technology to monitor and characterize the waves within the ionosphere caused by space and Earth disturbance. Experiments were designed to do this.

This research is noteworthy because it will offer novel insights into the imaging of waves within the ionosphere and their correlation with Earth-disturbing events that trigger them. The data obtained from this research, which is associated with physical events, has the potential to enhance monitoring capabilities and potentially contribute to the prediction of Earth-disturbing events. The SDR Earth Imager and its associated signal processing methodology is unique. The system has been prototyped by University of Victoria researchers at the Dominion Radio Astrophysical Observatory (DRAO) in Penticton, BC and at the LWA and LWA-SV stations in central New Mexico, USA. At both locations, high resolution phase images were obtained. These

measurements provide valuable data for studying the waves in the ionosphere. The insights gained from studying these disturbances may contribute to our understanding of various phenomena, including man-made disturbances, as well as potentially shedding light on other areas such as earthquakes, storms, and extreme local and global weather events.

1.5 Research Contributions

The new device, the SDR Earth Imager, focuses on extracting the phase information representative of the ionosphere and its disturbances, whether from Earth or space. Such a device is needed to obtain specific information about human-made disturbances, including power losses from electricity generation plants as well as natural Earth disturbances such as earthquakes, volcanic eruptions, hurricanes, tsunamis, tornadoes, etc., both during their occurrence and potentially during the preparation phase before these events. Hence, the SDR Earth Imager was researched and developed. If premonitory signs of a disaster can be identified prior to its occurrence, these indicators have the potential to mitigate the loss of human lives and property significantly. The application of the SDR Earth Imager is not only to measure and monitor the solar, geomagnetic, and meteorological Earth disturbing events but also to use it for climate change understanding, enabling plans to mitigate it.

Climate change primarily results from long-term variations in Earth's temperature pattems caused by factors such as greenhouse gas emissions, deforestation, and changes in land use. While human activities, including power generation, can contribute to greenhouse gas emissions and climate change, the direct influence of energy generation, conversion and use on climate change might be minimal compared to these broader factors. In the future, it may be possible to use the Earth Imager for detection of earlier earthquakes and volcanos signatures that are not possible now. Moreover, it may become possible, but not included in this thesis research project, to use the Earth Imager to measure the atmosphere's refractive indices from the ionosphere to the terrestrial surface, which would help predict local to global daily weather [4]. This could be accomplished using a low pass filter to obtain the low frequencies, that is, small phase shifts, associated with the Earth's Atmosphere’s temperatures, pressures, and compositional gradients.

1.6 Conducting Experiments and Data Analysis: Challenges and Considerations

The experiments in this work follow four stages;

- The first stage was mechanical, where the researchers built a Earth imager at DRAO. The idea of this activity was planned for over a year and then executed at DRAO. Over the course of three days, several data-collection sessions were held.
- In the second stage, the DRAO data was analyzed based on having used a linear antennae array. Each passive antenna used as a receiver detecting the phase information separately. All of the phase measurements were then used to make a phase image based on the position of the antenna within the array. In this phase image, each receiver is essentially a pixel within the image. The difference in phase between each pixel measures a phase shift. The phase shifts, which are periodic like a wave, symbolize the frequencies of a set of ionospheric waves from their periodicity that was mathematically analyzed using the Fourier transform to produce a Fourier image. A preliminary data analysis of the dataset was performed in order to test whether the phased array could image the ionosphere. A novel method was applied to the data involving the orientation of the linear antennae array with respect to the direction of wave propagation, which was successful. This method was considered the proof of concept for being able to actually image the ionospheric waves. This study was limited due to the lack of antennas at DRAO. Thus, these experiments were relocated to New Mexico to take advantage of the long-wavelength radio wave arrays offering high-resolution imaging capabilities.
- The third stage imaged and measured the wavevector of a strong set of ionospheric waves using two LWA-1 and LWA-SV radio wave arrays that had 256 radio wave antennae. This stage included developing a novel technique for detecting the source of disturbances. The analysis of their datasets illustrated that many sets of ionospheric waves exist, with roughly 170 sets of waves found at both stations.
- The final stage of this research was to provide a relatively simple method based on a capacitor model to measure the power of the ionospheric waves. It was determined that the measured power corresponds to the local power generated from electric power generating stations and consumed by Albuquerque. It may be concluded that the power consumed has not been lost but instead captured by Earth's ionization layer. This observation may be crucial in

comprehending the man-made dynamics of global climate change. Human activities, including electricity production, may not be directly responsible for climate change, but they can significantly contribute to greenhouse gas emissions, which in turn have an impact on climate change.

- Several obstacles were encountered while conducting DRWO (Directional Radio Wave Observations) and LWA (Long Wavelength Array) experiments. In the DRWO experiments, one of the challenges faced was the limited area for antenna distribution due to the occasional presence of cattle herds beyond the fence. This posed a potential risk of trampling and damaging the coax cables. Another challenge arose from the need for careful movement while setting up the antennas due to the presence of rattlesnakes, which resulted in increased setup time. Additionally, the limited resources restricted the spatial resolution of the 2D images formed by rotating the antennae to only four linear antennae.
- In the LWA experiments, it was challenging to distinguish the complete cycle of waves due to the non-linear nature of the antennas used for LWA and LWA-SV. However, a positive aspect was that having 256 antennae resulted in a higher number of pixels. In addition, there were instances where one or two antennas malfunctioned, necessitating their exclusion from the experiments. Moreover, certain frequencies transmitted during the experiments did not reflect from the ionosphere sufficiently. The data's complex structure and the carrier wave extraction posed additional difficulties. Additionally, the tasks of finding the correct time sequences of the data and developing Python codes to read and process them proved to be time-consuming.
- Finally, the results of the data interpretation unveiled waves that presented a challenging task for my PhD research in establishing their relationship with their source of disturbance.
- The datasets collected at DRAO were obtained by collaborating with Dr. Stephen Harrison, Nickolas Bruce (a fellow student) now employed by DRAO, and by myself, setting up the antennae array and collecting data. I also applied the idea of imaging the ionospheric waves and implemented the entire analysis. The New Mexico data was taken via a team of LWA scientists, although I was the sole analyzer of the data and sole investigator of the source of disturbances using two locations of the antennae array. My main contribution was using the antennae array as a camera to produce images of the ionospheric waves and relate them to their Earth disturbance using the measured phase shifts, frequencies, and wave vectors associated with a set of ionospheric waves.

1.7 Dissertation Outline

This dissertation has been assembled through a compilation of previously published manuscripts as well as unique background material. It is structured into the following six chapters.

Chapter 2 contains a synopsis of atmospheric and ionospheric structure. It covers a series of investigations by researchers on ionospheric disturbances, how the ionosphere responds to varied disturbances, and some background information related to ionospheric waves and their characteristics. Moreover, a brief overview of radio waves and a Software Defined Radio Block Diagram has been presented.

Three chapters of this dissertation contain the following publications:

Chapter #3: The initial publication regarding the research concept applied at DRAO, which successfully imaged the ionospheric waves, can be found in the Journal of Atmospheric and Solar-Terrestrial Physics [9]. Additional information for data collection and analysis has been provided in this chapter, but is not included in the publication.

Chapter 3 illustrates the method and the experiments carried out at DRAO, Penticton, BC. The prototype of the SDR imaging device was tested at DRAO to generate images of the ionospheric waves existing within Earth's F ionization layer. Only four linear array antennae were utilized. They were rotated to form 2D images. The data analysis resulted in revealing the existence of moving waves linked to Earth's F ionization layer.

Chapter #4: The Earth Imager was shown to locate the source of the ionospheric disturbance, Atmospheric Remote Sensing Journal [10].

Chapter 4 presents a technique of analysis to determine the source or location of the ionospheric disturbance using the Earth Imager. For this study, the two Long Wavelength Array (LWA), LWA-1 and LWA-SV, New Mexico, were employed to capture the radio wave signals reflected from Earth's F ionization layer. They enabled the location of the disturbance to be identified from the intersection point of the wavevectors measured at the two sites. The study here focused on detecting the wavevectors, frequencies, and phase changes of the ionization layer wave.

Chapter #5: This manuscript focuses on providing a method to measure the power of a set of ionospheric waves and then relate it to the Earth disturbance responsible for its creation, Journal of Imaging [11].

Chapter 5 focuses on measuring the phase shifts, frequencies, and wave vectors of the waves within the ionization layer and correlating these waves to their Earth disturbing event. This

includes the power generating stations and their transmission line losses. The observed data analysis of their power and the estimated power loss from adjacent Albuquerque power sources agreed with the mathematical model and experimental measurements.

Chapter 6 highlights the essential findings and contributions and suggests potential future work.

Chapter 2 Research background and Literature Review

2.1 Research Background

2.1.1 Electromagnetic Waves, Including Radio Waves

Electromagnetic waves can transfer energy from one place to another through a vacuum as well as a medium. They travel through electrical and magnetic fields generated by charged particles. Instances of electromagnetic waves include radio waves, visible light waves, microwaves, infrared waves, visible light, ultraviolet rays, and X-rays. Electromagnetic waves of low energy and frequency are long wavelengths, such as radio, as shown in Figure 2.1 [12].

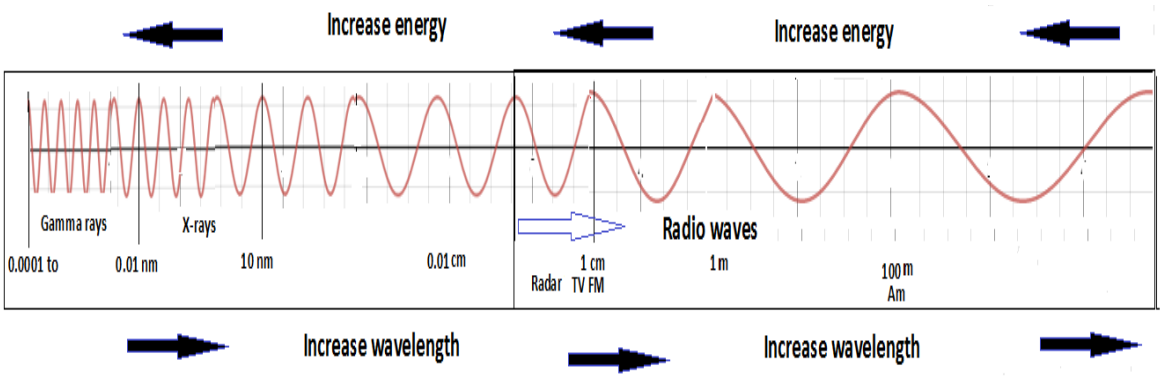

Figure 2.1 Electromagnetic spectrum [13].

Since radio waves are electromagnetic, traveling at the speed of light with no mass or charge, they easily pass through the Earth's ionosphere. The radio wave is a combination of both changing electric and magnetic fields, as depicted in Figure 2.2, enabling its coupling to electrons in the ionosphere.

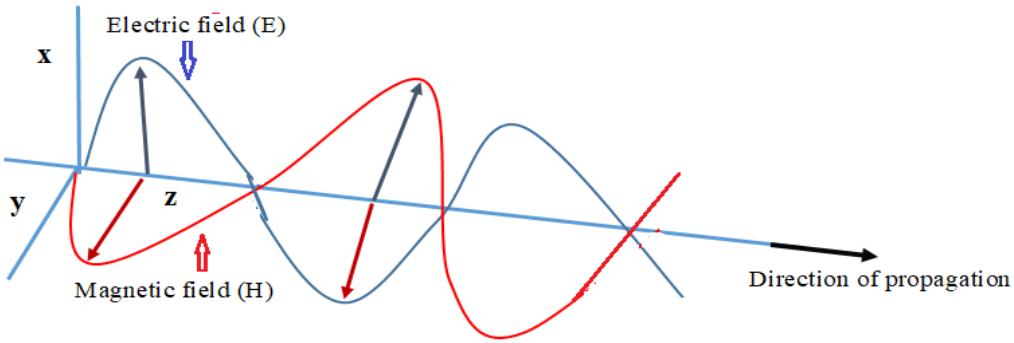

Figure 2.2 Electric and magnetic waves.

2.1.2 Ionospheric Waves

It is widely acknowledged that Earth disturbances generate atmospheric waves that travel through the atmosphere and reach the upper atmosphere, resulting in the formation of traveling ionospheric disturbances (TIDs). Seismic events, geomagnetic storms, man-made disturbances, etc., can generate waves that propagate through the atmosphere and affect the ionosphere. Those waves have mass and charge, and they are able to travel at different speeds in the ionosphere. The speed of the ionospheric wave generated by a Nepal earthquake was 2000 m/s [14]. Solar flares and coronal mass ejections that happen in the space environment surrounding the Earth are also considered as space disturbances [15].

2.1.3 Properties of Waves and Wave Graph

Many properties describe waves, including amplitude, phase, frequency, wavelength, speed, and period. For example, Figure 2.3 shows that the vertical axis represents the amplitude of the wave, whereas the horizontal axis can be either time or distance.

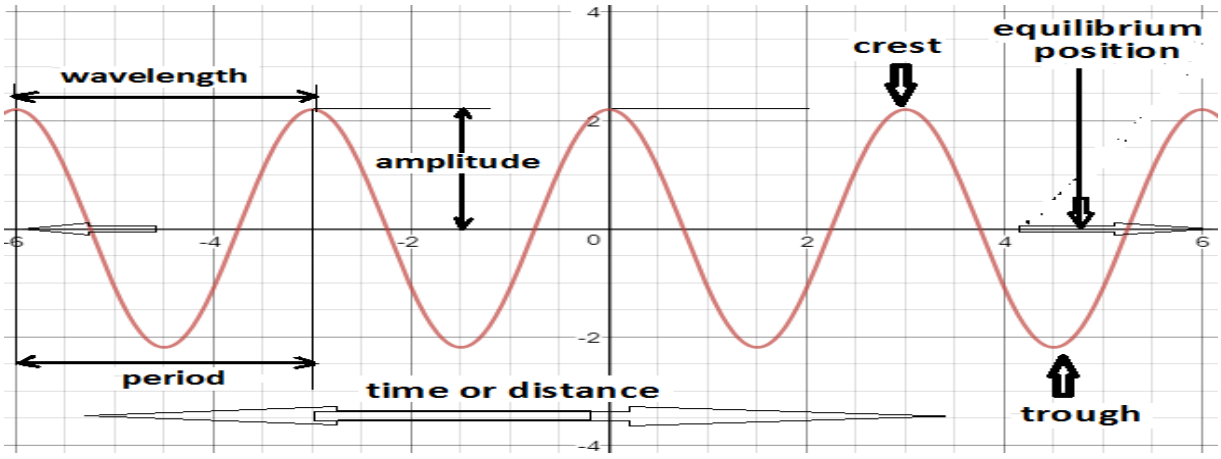

Figure 2.3 Period, wavelength, and frequency of a wave.

The amplitude is the largest distance that the wave particles move up and down between the rest position of the wave and the crest or trough, as seen in the graph below [15]. The wave strength is measured by the amplitude property. For example, the amplitude of the wave in vibration measurements for rotating equipment is the main factor in describing the severity of the vibration. In addition, the amplitude of sound waves measures the loudness of the sound which can be controlled. There is a significant relationship between the amplitude of a wave and the amount of energy it carries. A wave with a larger amplitude carries more energy compared to a wave with a smaller amplitude of the same type. However, when considering waves of different kinds (e.g., different frequencies or wavelengths), comparing their amplitudes alone does not provide a meaningful measure of their energy content. A wavelength is a distance between two consecutive points on the one-cycle wave that represents the wavelength of two peaks or crests, as shown in Figure 2.3. However, in a longitudinal wave, the wavelength (λ) can be determined by the space between either two compressions or rarefactions. A smaller wavelength carries more energy than a large wavelength. This relationship is opposite to large amplitude, which carries more energy.

The wave period T is the time interval between observation of two successive crests, or troughs, at a single location. In contrast, the frequency of a wave is the number of wavelengths that pass per second in wave cycles. The symbol of frequency is f, measured in Hertz or cycles per second. The frequency of a wave and its period is shown in the following formula [15]. However, the speed of a wave can be influenced by the medium and the type of the wave.

$$\text{period} = \frac{1}{\text{frequency}} \rightarrow \mathbf{T} = \frac{\mathbf{1}}{\mathbf{f}} \qquad (2.\ 1)$$

$$Speed = \frac{wavelength}{period} \rightarrow v = \frac{\lambda}{T} \qquad (2.\ 2)$$

2.1.3.1 Phase

The phase of a wave is one of the essential parameters that provide information about a particular point in time of a sinusoidal wave. The unit of phase measurement is degrees or radians. A complete cycle is 360 degrees or 0 to 2π in radian measurements.

The term phase shift refers to the difference in the phase angle of a waveform cycle. Phase shift occurs when the phase angle of a waveform changes. Shifting the position of the phase angle to a horizontal axis is shown in Figure 2.4. A vertical shift indicates that the function changes from zero position on the vertical axis.

The description of the wave oscillation in time is given by:

$$S(t) = A(t)\cos(\omega t \pm \Phi) \qquad (2.\ 3)$$

A (t) is the amplitude of the wave, ω (radian/sec) is the angular frequency of the wave, and Φ (degrees or radians) is the phase angle.

The phase difference Φ in time for a sinusoidal wave, which is the delay time, is equal to the phase shift, which is the phase delay. The phase difference of a sinusoidal wave is shown in Figure 2.4. Two sinusoidal waves have the same frequency, representing a time difference Δt. A phase shift is shown for the shift in time. The amplitude, period, phase shift, and vertical shift of waves are shown in Figure 2.5.

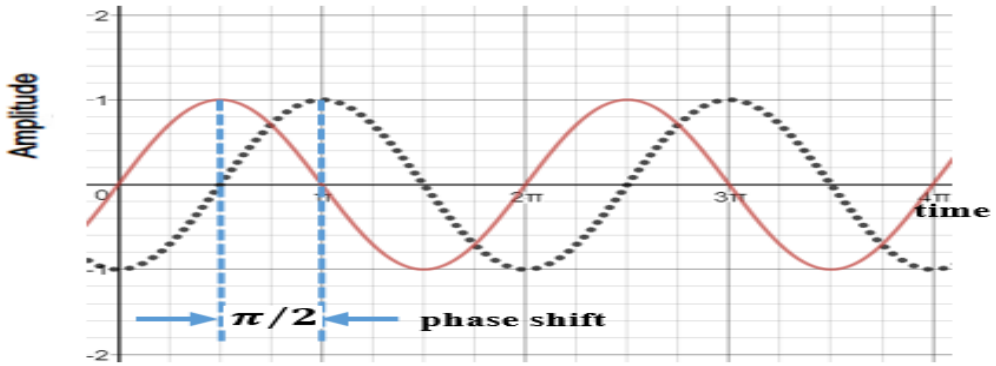

Figure 2.4 The phase difference of a sinusoidal wave on the X-axis.

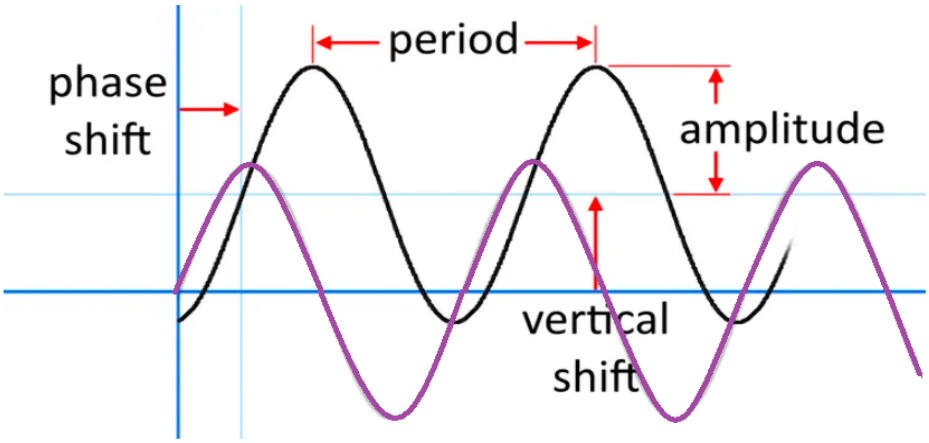

Figure 2.5 Amplitude, period, phase shift, and vertical shift.

The phase shift is determined by a shift in time. Δt multiplies the frequency of the wave and 2π radian, as seen in Figure 2.6. T = 1/f

$$\Delta\Phi = 2\pi.f.\ \Delta t, \qquad (2.\ 4)$$

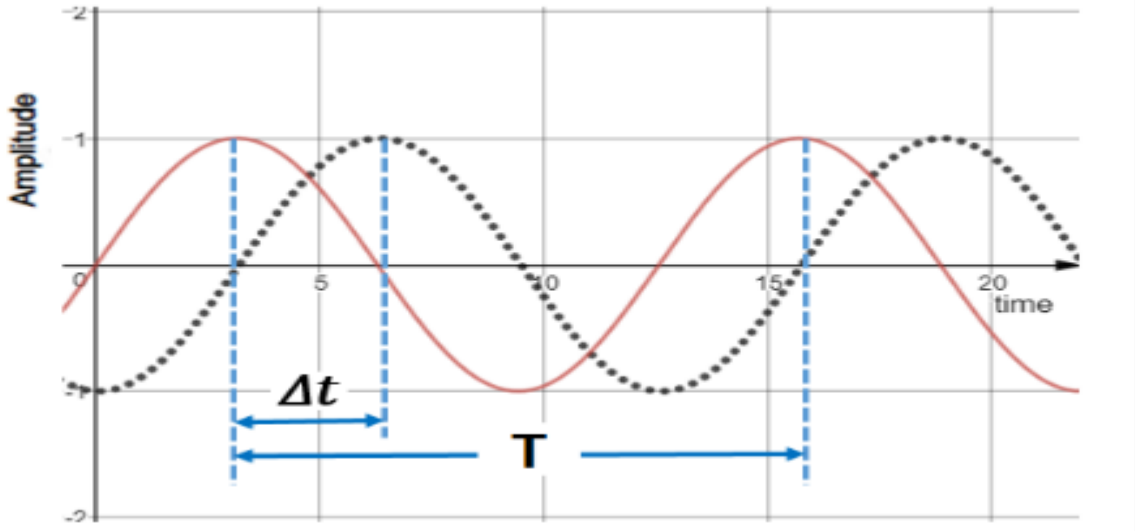

Figure 2.6 The phase shift in time.

The path length of a radio wave (L) thatpropagates from the transmitter to the receiving array antenna, equals total phase variation. The phase difference $\Delta\varphi$ is the delay in the arrival of the radio wave signal.

$$\Delta\varphi = 2\pi\ (\ \Delta L/\lambda\ ) = 2\pi\ f\ (\Delta L/c\ ) \qquad (2.\ 5)$$

where $\Delta\varphi$ is the phase variation from transmission to reception, f is the frequency, λ is the wavelength, and c is the speed of light.

The SDR Earth Imager measures the amplitude of the ionospheric waves by measuring the phase shift created by the difference in path length from the top to the bottom of the ionospheric wave. This difference in path length creates a difference in phase recorded at each antenna using the quadrature, the hardware method, as well as a difference in time each antenna receives the radio wave, the software-defined radio method. Each method, i.e., hardware and software, produces the same measurement of the phase shift representative of the size of the ionospheric wave.

Phase wrapping maps the principal value of phase angle to the range of $-\pi$ and π. This means that if the phase is greater than pi+delta, the wrapped phase will wrap around to -(pi-delta). However, the wrapped phase does not display a complete cycle of a wave. To betterillustrate wave cycles the unwrapped phase is used, which ensures that all upcoming wrapped phase values add up to a phase offset - 2π or 2π. Figure 2.7 shows examples of wrapped and unwrapped phases [16], [17].

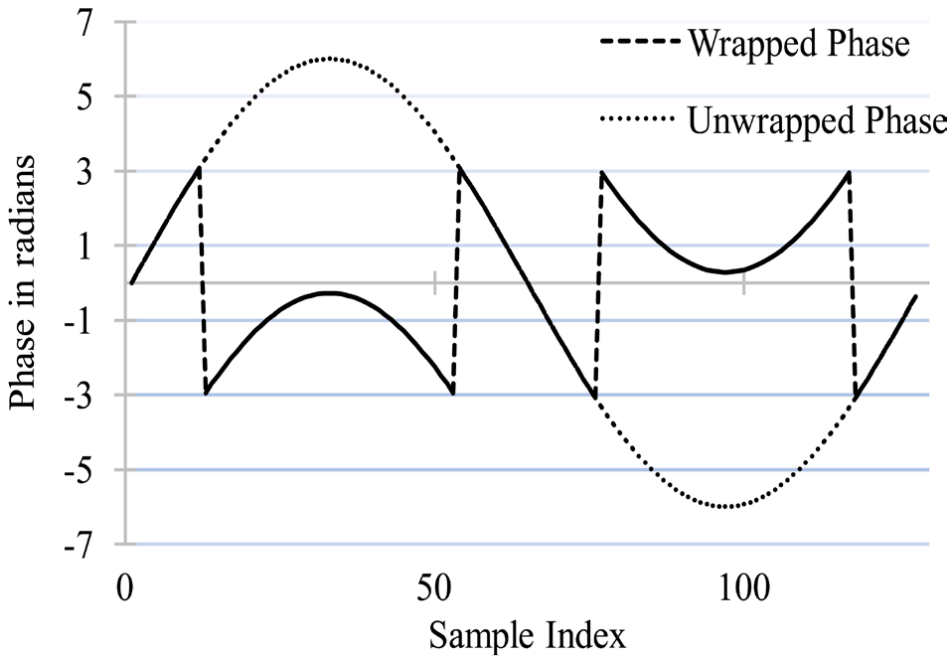

Figure 2.7 Wrapped phase and unwrapped phase [16].

2.1.4 Imaging Ionospheric Waves Using Radio Waves

Several imaging techniques are utilized to observe the characteristics of ionospheric waves, including ionogram imaging, ionospheric tomography, incoherent scatter radar, and SDR Earth Imager as illustarted in this dissertation.

Each technique allows for the creation of visual representations of the ionospheric waves. The concept of imaging the ionospheric waves using radio waves involves transmitting a radio wave at nearly vertical incidence from one location, which then travels through the lower atmosphere to the upper atmosphere and into the ionosphere, where it is reflected back to Earth and received at a second location by an array of radio wave antennas. Due to the waves within the ionosphere causing reflection of the radio wave at different points within the ionosphere, each antenna receiver receives the radio wave at a different time. The phase shift can be derived from the differences in the time of reception at each antennae. A hardware method of measuring the phase using the quadrature of the transmitter and the quadrature of the receiving antenna was often employed. Each receiver in the array producing a phase measurement appears as one pixel in the phase image. The size of the array determines the pixel count of the image and may determine the resolution of the phase image The greater the number of antennas we have, the greater the potential to image the waveform of the ionospheric waves necessary to measure their phase shift, frequency, and wave vector. Another factor that could determine phase image resolution includes the quality of the radio wave signal, i.e., its peak to background or noise level.

Figure 2.8 illustrates an example of an array of four antennas arranged in a square configuration, measuring cross-polarization to image the wave. The ability to measure the wave vector of the surface waves depends on the orientation of the antenna, as illustrated in Figure 2.9 and Figure 2.10. The wave front is possible to be measured when the antennas are oriented in the same direction as the wave vector.

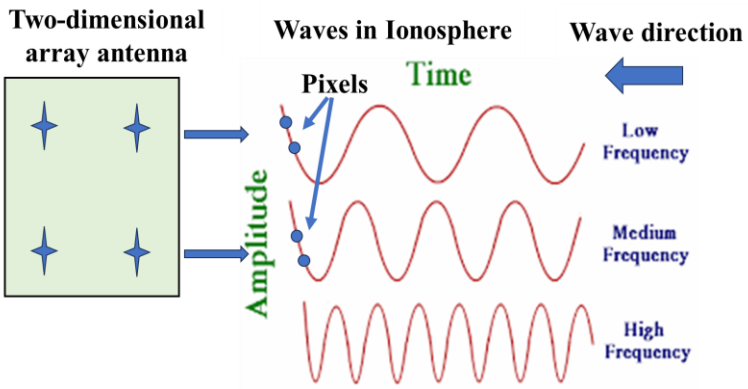

Figure 2.8 Array of four antennas as a square measuring the cross-polarization.

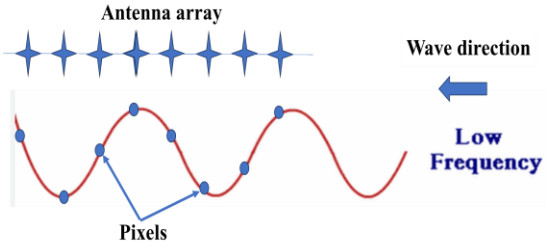

Figure 2.9 The array of eight antennas parallel to the wave vector.

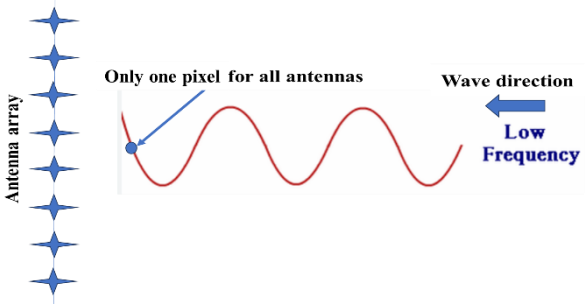

Figure 2.10 The array of eight antennas perpendicular to the wave vector.

2.1.5 Fourier Transform

A Fourier transform converts a signal from the time domain or spatial domain to the frequency domain. This technique allows splitting complex signals into a number of frequencies, as shown in Figures 2.11 and 2.12. Understanding the fundamentals of the Fourier transform will assist in separating mixed waves from data collection of the ionosphere by analyzing the phase image.

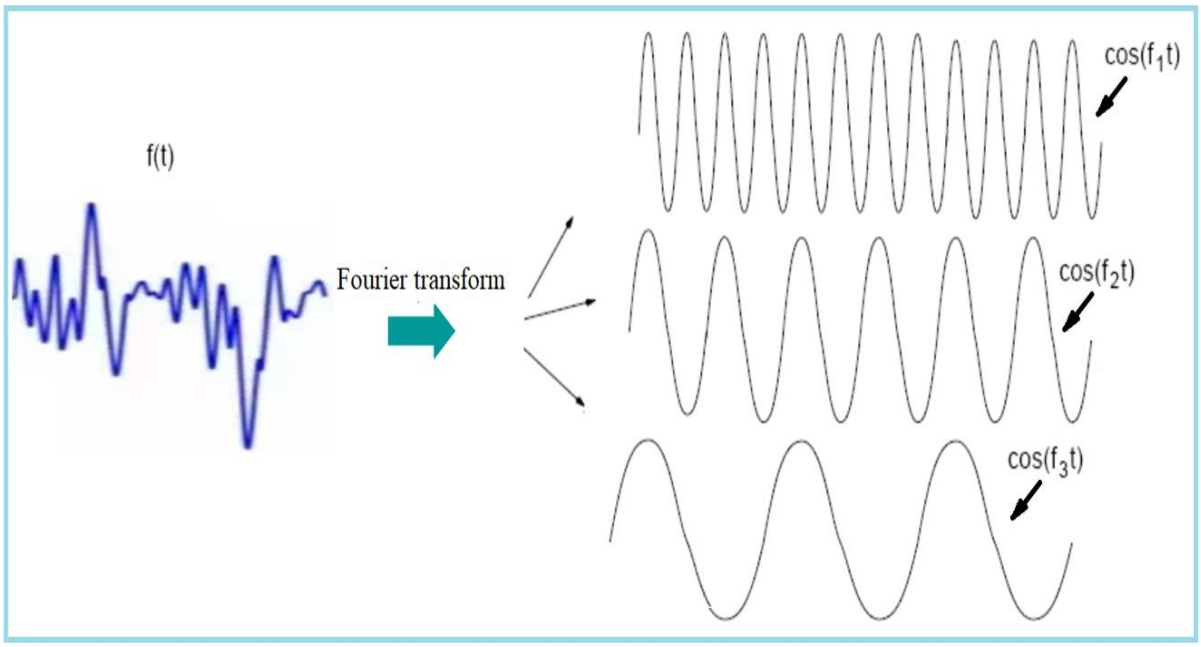

Figure 2.11 Using a Fourier transform, a complex signal was divided into several sinusoidal waves.

2.1.5.1 Execution Code for Fourier transform

The Fourier Transform can be implemented differently based on the software platform or programming language. Python (using libraries like NumPy or SciPy) is commoly used to execute the Fourier Transform in this research.

2.1.5.2 Length of Time Series

The required length of the time series for performing Fourier transforms in Python code depends on the lowest frequency waves of interest that are intended to be captured. According to the Nyquist-Shannon sampling theorem, it is necessary to sample at a rate that is at least twice the highest frequency to be analyzed. Therefore, recording a time series that spans a sufficiently long duration is typically required to capture the lowest frequency waves of interest accurately. The chosen time series duration varied from one second, which contains about 512 samples, to fifteen seconds.

2.1.5.3 Ensemble Averaging

Ensemble averaging is a technique frequently employed in Fourier analysis to improve the signal-to-noise ratio. A lengthy time series must be divided into several overlapping windows, and the Fourier Transform must be determined for each window. After that, an average of the produced transforms is used to estimate the underlying frequency content more accurately. This approach can help reduce the effects of noise or variability in the data.

2.1.5.4 One-Sided or Two-Sided Spectra

The results of the Fourier Transform show the frequency spectrum of a signal. The representation of spectra can vary depending on the nature of the signals being analyzed and the specific application. Two-sided spectra display both positive and negative frequency components of a signal. They are often used in situations where the frequency characteristics of signals may be complex-valued or contain both positive and negative frequencies as shown in Figure 2.12. Two-sided spectra find applications in various fields, including telecommunications, radio frequency analysis, and radar systems.

2.1.5.5 Complex Output and Interpretation

A Fourier Transform generally yields complex-valued output. The complex value represents each frequency component in the signal, including its phase and amplitude. The phase shows the relative timing or position of the component, whereas the amplitude relates to the intensity or magnitude of the component.

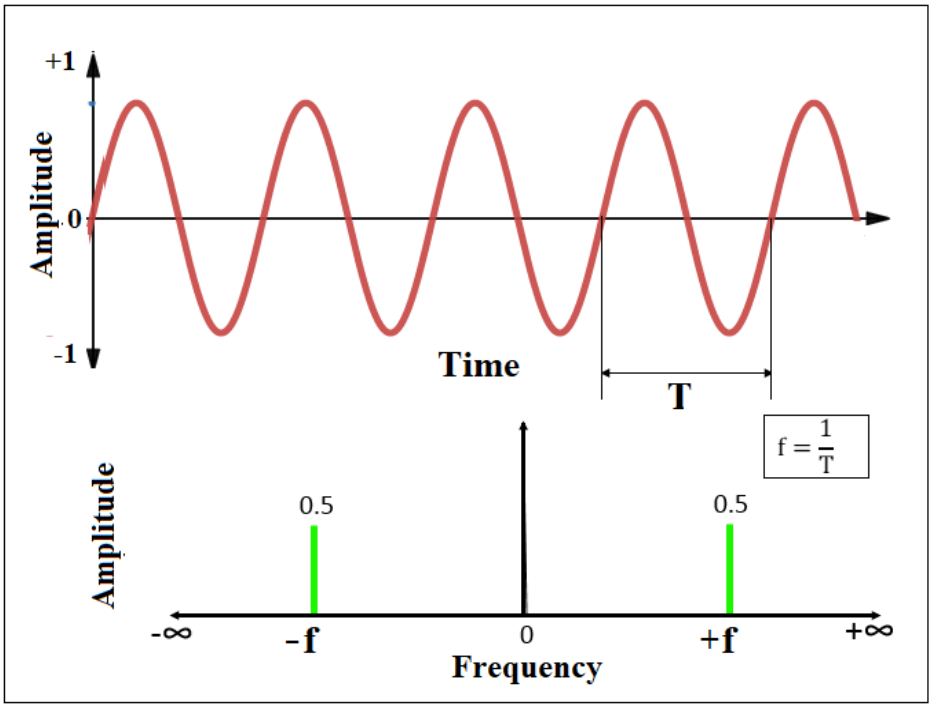

Figure 2.12 Fourier transform converting time domain to frequency domain.

2.1.6 Atmosphere and Ionospheric Regions

The structure of the atmosphere is divided into five different layers. Since the atmosphere is not uniform, its properties change with altitude. The air temperature and pressure properties change with altitude. These distinct layers are the troposphere, stratosphere, mesosphere, thermosphere, and exosphere, as shown in Figure 2.13 [18]. The ionosphere is located in three of those five layers: the thermosphere, the upper mesosphere, and the lower exosphere [12].

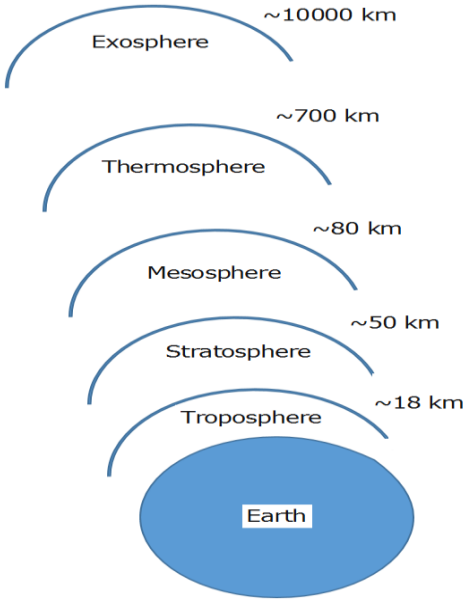

Figure 2.13 Atmosphere layers.

The ionosphere is located in the upper region of Earth's atmosphere, spanning from approximately 60 km to over 500 km in altitude, where the neutral molecules such as nitrogen N2 and oxygen O_2 absorb radiation to form ions. Extreme ultraviolet (EUV) and X-ray radiation hit the neutral atoms or molecules, producing negatively charged electrons and releasing positively charged ions and free electrons, as seen in Figure 2.14. The terrestrial ionosphere is split into three layers: D, E, and F [12]. These layers have varied ionization according to the time of day, solar cycles, seasons, and solar activity. For instance, the upper layer of the ionosphere, the F region, is split into two layers, F1 and F2, during the day.

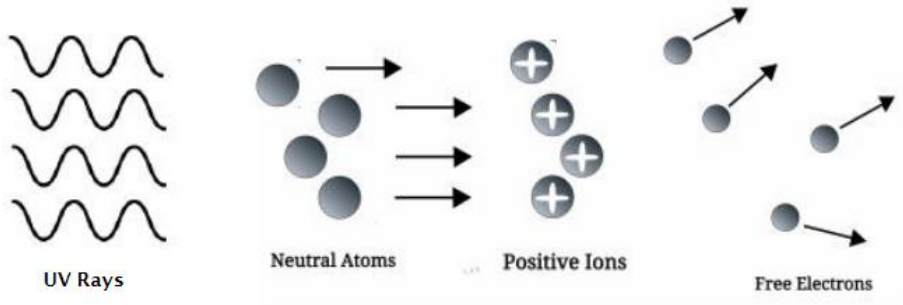

Figure 2.14 Solar energy hits neutral atoms, generating positive charges and free electrons [19].

2.1.7 D Region

The D layer of the ionosphere is approximately 50 to 90 km altitude and consists of neutral components such as oxygen O_2, nitrogen N_2, argon Ar, carbon dioxide CO_2, and helium He. At low altitudes of the ionization layer (D region), the major ions are NO^+ (nitric oxide) and O_2. The electron density of this layer depends on the height, which differs from the diurnal time change, seasonal fluctuation, and solar cycle variations [20].

2.1.8 E Region

The altitude of the E layer stretches from ~95 km to 150 km above the ground. Solar radiation, such as X-rays and ultraviolet (UV), ionizes neutral molecules, including mainly NO^+, $O2^+$, and secondary O^+ and $N2^+$ ion components. This layer disappears at night because the rate of ionic recombination is quick. However, it does not vanish completely and remains weakly ionized [20].

2.1.9 F Region

The F layer is between 140 and 600 km above the surface of the Earth and is the most significant layer because of its availability during day and night. During the night, the recombination of ions and electrons within the F layer occurs at a slower rate compared to the ionization process during the day. This slower recombination process allows the F layer to persist and support radio wave propagation. Although the electron density within the F layer may decrease during the night, it is still sufficient for radio waves to be refracted back to Earth. It is the primary interest of communications and navigation systems. Thus, it is beneficial to the SDR Earth Imager research. When neutral atoms and molecules absorb EUV (Extreme Ultraviolet) radiation, Ions and electrons are produced. These particles lead to ionizing O+ and N2+. The F layer divides into two layers during the daytime, the F1 and F2, but these layers merge into one layer at night because of slow recombination after sunset. Because the ionization remains overnight, it can still affect radio signals. The F layer has the highest electron density since the electron density of the F2 layers is influenced by the sun, causing a rapid increase at any time during the day with maximum values, as can be seen in Figure 2.15 [10, 11].

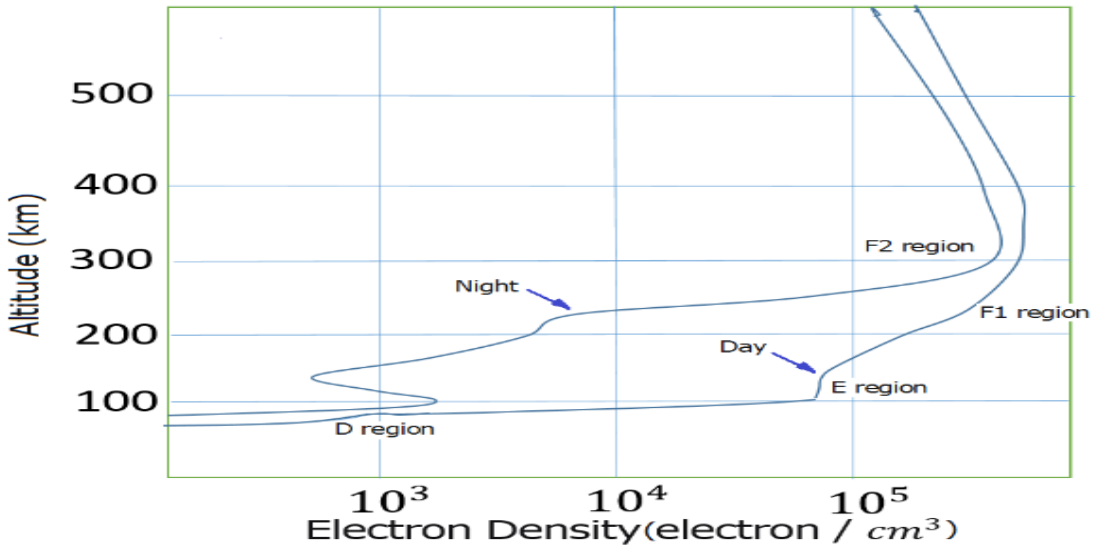

Figure 2.15 Density of electron in ionization layers [20].

2.2 Literature Review

2.2.1 Ionization Layers and Reflected Radio Waves

The existing understanding of the electrically-conducting ionospheric layer in the upper atmosphere was built several papers mentioned next are 100's of years ago . These layers can be affected by any electrical or magnetic field. Carl Gauss in 1839 and Kelvin in 1860 put forward the concept of a conductive layer in the atmosphere being influenced by variations in the Earth's magnetic field [19]. They expected that the upper atmosphere contained ionized regions. In 1878, Balfour Stewart postulated that the conductive layer existed in the upper atmosphere and explained the regular fluctuations of the Earth's magnetic field. In 1902, Arthur E. Kennelly and Oliver Heaviside made predictions regarding the propagation of radio transmissions at a frequency of 300 kHz. This frequency had been transmitted by Marconi in 1901 and was reflected from an ionized layer in the upper atmosphere [21]. The phase comparison was made between the ground wave and the reflected wave from the ionosphere to prove and identify the height of the existence of the ionization layer by Appleton and Barnett in 1925 [22]. A year later, Breit and Tuve measured the heights and critical frequencies of ionosphere layers, and they transmitted pulses by using the first ionosonde [23]. In 1931, Chapman illustrated a theory of an ionized layer formation caused by solar activity [24]. After that, Appleton described radio wave propagation in the ionosphere by

developing some equations, including absorption influenced by the Earth's magnetic field [25]. The characteristics of plasma to reflect radio waves are well-known by plasma physics scientists.

2.2.2 Radio Wave Propagation

2.2.2.1 Effects of Transmission Medium

Radio waves are influenced by different media when they are propagated. In fact, the boundary between two different mediums causes the radio waves to change direction. Some energy of the radio waves might be absorbed by the medium or be reflected back into the original medium, and the radio waves might pass into the following medium at a varying velocity.

2.2.2.2 Radio Wave Reflection

Radio waves change direction when they strike a surface or travel between mediums. An incident wave is reflected when it strikes two media that are separated by a boundary. The surface of the medium works acts as a mirror to reflect radio waves. When radio waves are transmitted by the angle of incidence or vertical to the ionization layer as a sky wave, the sky wave reflects off the ionosphere and returns to a passive antenna. The angle of reflection is equivalent to the angle of incidence, and the speed of radio waves is the same as the speed of light waves [26]. Reflection occurs when there is a large difference in refractive index at an interface of two media. Reflection of the radio waves from the ionosphere used by the SDR Earth Image does not use this method but refraction.

2.2.2.3 Radio Wave Refraction

The bending or change in direction that happens when radio waves travel through the ionosphere is referred to as radio wave refraction. The variation in the density of the ionized gases causes a variation in the refractive index through the ionosphere [27]. Refraction is understood to be the mechanism of radio wave reflections from the ionosphere used by the Earth Imager.

2.2.2.4 Ground and Sky Wave Propagation

A transmitting antenna sends radio waves through the atmosphere as ground waves and sky waves to a receiving antenna. A ground wave propagates along the curvature of the Earth's surface rather than traveling through the atmosphere. Ground waves are mostly employed in communications [28]. Ground waves are not being used in this project. They may be used in the future if they can be separated from the sky wave. Nevertheless, compared to other radio wave types, such as skywaves and space waves, ground waves are often restricted to shorter ranges and lower frequencies.

A radio wave spreads outward in all directions from its source. This means that when a radio wave is emitted from a transmitting antenna, it forms a spherical waveform. A description of an isotropic radiator and how it propagates radiation can be seen in Figure 2.16. The radio wave propagates out in all directions as it goes through space, getting weaker as it gets farther from its source. Generally speaking, the high frequency (HF) band, which includes frequencies between 3 and 30 MHz, is considered the most effective range for sky wave propagation [29].

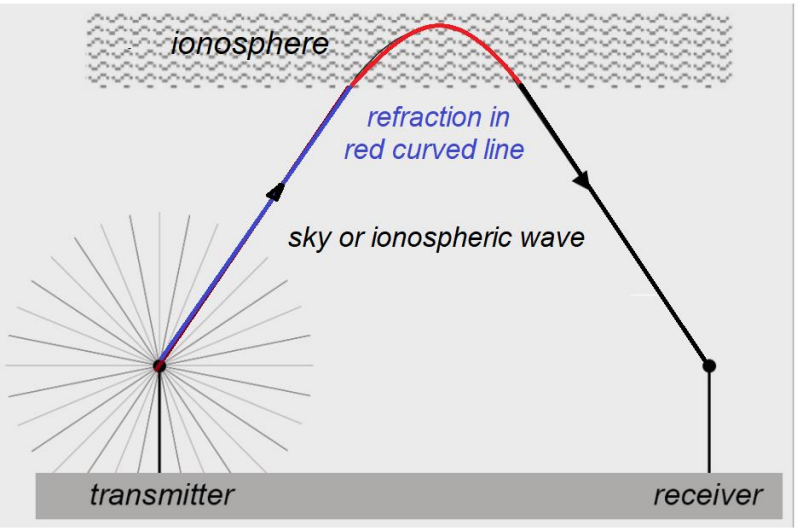

Figure 2.16 A sky wave radiation transmission between a transmitter and receiver *[29]*.

High levels of free electrons in the ionosphere have an impact on radio wave propagation. This essentially bounces the radio wave back toward the Earth [27, 29]. Radio wave entering the ionosphere from below starts facing a low level of electron density to a high level, as represented by the plots (Figure 2.17).

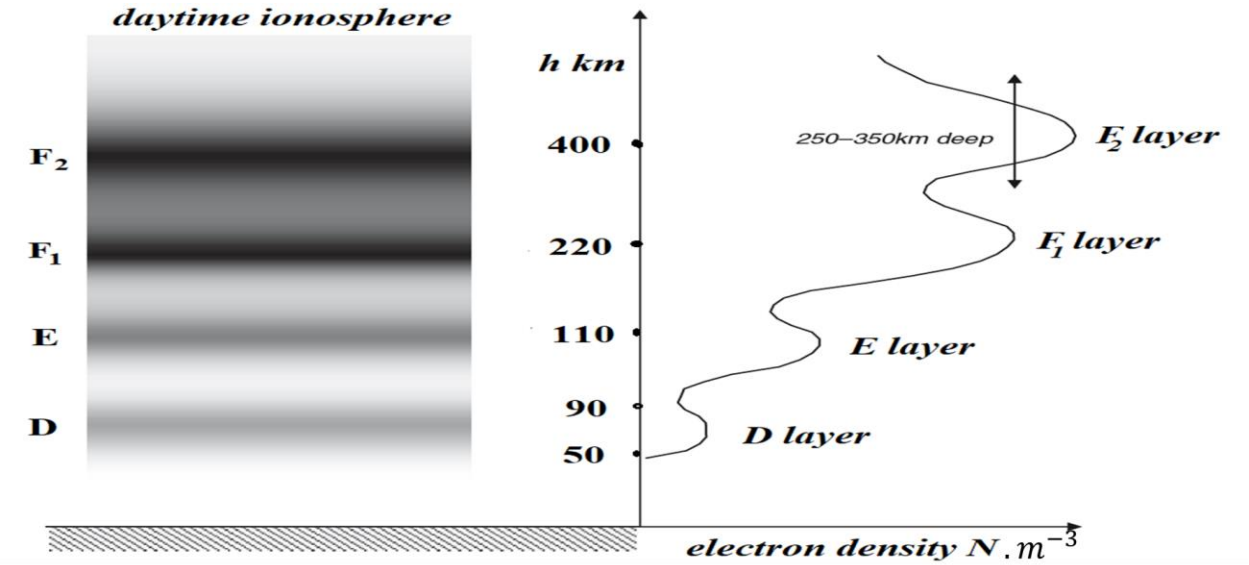

Figure 2.17 A set of slices representing an area of continually fluctuating ionization while assuming constant electromagnetic properties *[29]*.

The electromagnetic beam will refract as it moves from one portion to another of the ionosphere because the refractive index decreases with height until its final angle of refraction is 90 degrees, at which point it begins to travel horizontally. At this point, the beam will then refract back down again; therefore, the 90-degree angle is thought to be crucial for ensuring that there has been sufficient refraction for the beam to return to the Earth's surface, as illustrated in Figure 2.18 [27, 30].

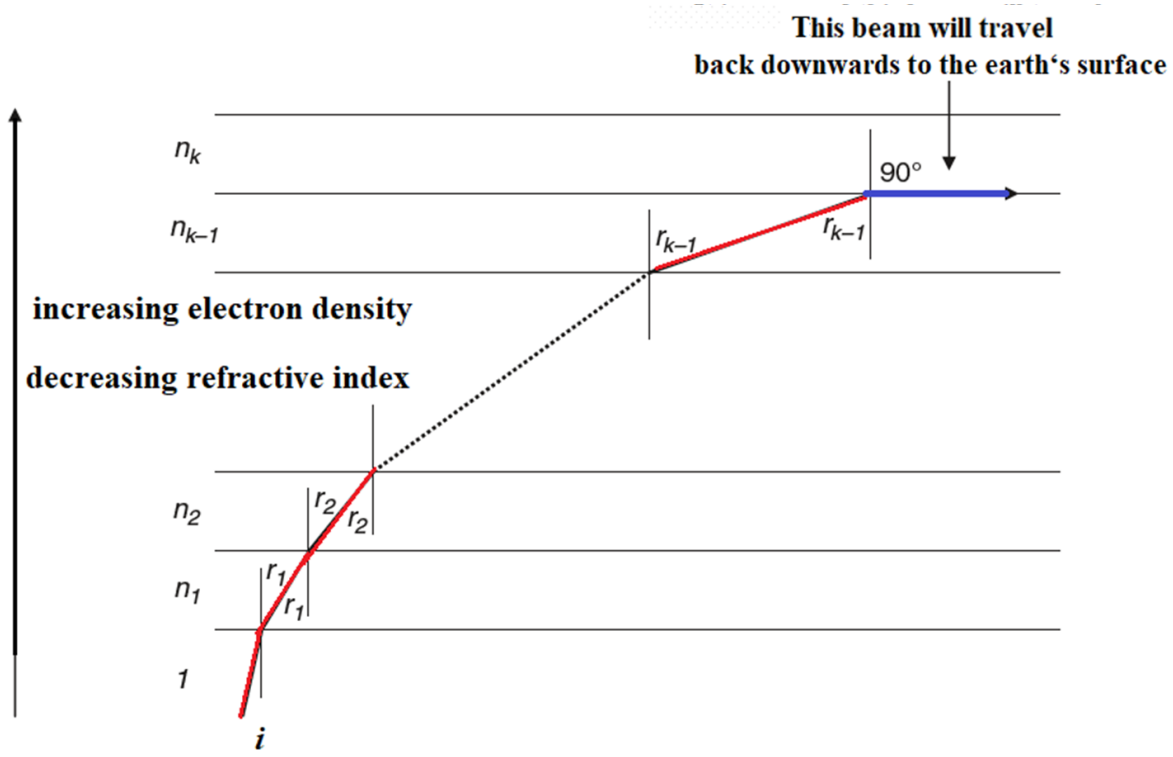

Figure 2.18 A radio wave refracted in the ionosphere will return to the Earth's surface at a 90° angle *[29]*.

Snell's Law of Refraction is applied to the geometry of Fig 2.18

$$\frac{\sin i.}{\sin r_1} = \frac{n_1}{1} \quad , \quad \frac{\sin r_1}{\sin r_2} = \frac{n_2}{n_1}, \ldots\ldots\ldots \frac{\sin r_{k-1}}{\sin 90} = \frac{n_k}{n_{k-1}} \qquad (2.\ 6)$$

In order that

$$\frac{\sin i}{\sin r_1} \times \frac{\sin r_1}{\sin r_2} \times \ldots\ldots\ldots \times \frac{\sin r_{k-1}}{\sin 90} = \frac{n_k}{1} \qquad (2.\ 7)$$

The condition that ensures that a emitted radio wave will be returned to the Earth's surface is,

$$\sin i = n_k \qquad (2.\ 8)$$

Thus, there must be an area in the layer where the electron density is sufficient for bending the radio wave, resulting in the beam to be returned that is mathematically equal to the sine of the angle of incidence at the ionosphere's entry. Otherwise, the beam will penetrate to the next layer [29].

The refractive index of a region with an ionization density of N electrons per cubic meter is

$$n = \sqrt{1 - \frac{81N}{f^2}} \quad (2.\ 9)$$

Where f is the frequency of the radiation that was incident.

For the signal to be returned at vertical incidence

$$\sin i = n = \sqrt{1 - \frac{81N}{f^2}} = 0 \quad (2.\ 10)$$

The condition of having a refractive index of zero (n = 0) reflects a desired outcome.

there is an area of high electron density inside the layer so that it always gets returned at vertical incidence.

$$f = 9\sqrt{N} \quad (2.\ 11)$$

The critical frequency is an electromagnetic wave that is just high enough to be refracted back to the Earth's surface by a particular ionosphere layer. The critical frequency is determined by the maximum electron density of the layer for reflection. The maximum electron density increases, moving up through the layers of the ionosphere. Therefore, the critical frequency also increases with altitude. This means that higher layers of the ionosphere will refract higher-frequency waves [29].

$$f_c = 9\sqrt{N_{Max}} \quad (2.\ 12)$$

Where Nmax is the layer's maximum electron density.

2.2.2.5 Virtual Height and Actual Height

When a radio transmitter sends a carrier wave into the sky, the carrier wave travels through the air and gradually bends through the ionosphere back to the earth due to refraction. The path that the carrier wave takes from the transmitter and the angle of reflection is used to determine the virtual height, which is the apparent height of the carrier wave's reflection point. However, the actual height of the reflection point is slightly lower than the virtual height because the carrier wave refracts as it passes through a dense layer in the atmosphere. This phenomenon causes the carrier wave to bend more than expected, resulting in a lower actual height than the virtual height, as illustrated in Figure 2.19.

Maximum Usable Frequency (MUF) is the highest frequency reflected by the ionosphere layer at the angle of incidence. MUF is determined by different factors, including time of day, the angle of incidence, and solar activity [32].

$$\text{MUF} = \frac{\text{critical frequency}}{\cos\theta} = \text{fc}\sec\theta \qquad (2.\ 13)$$

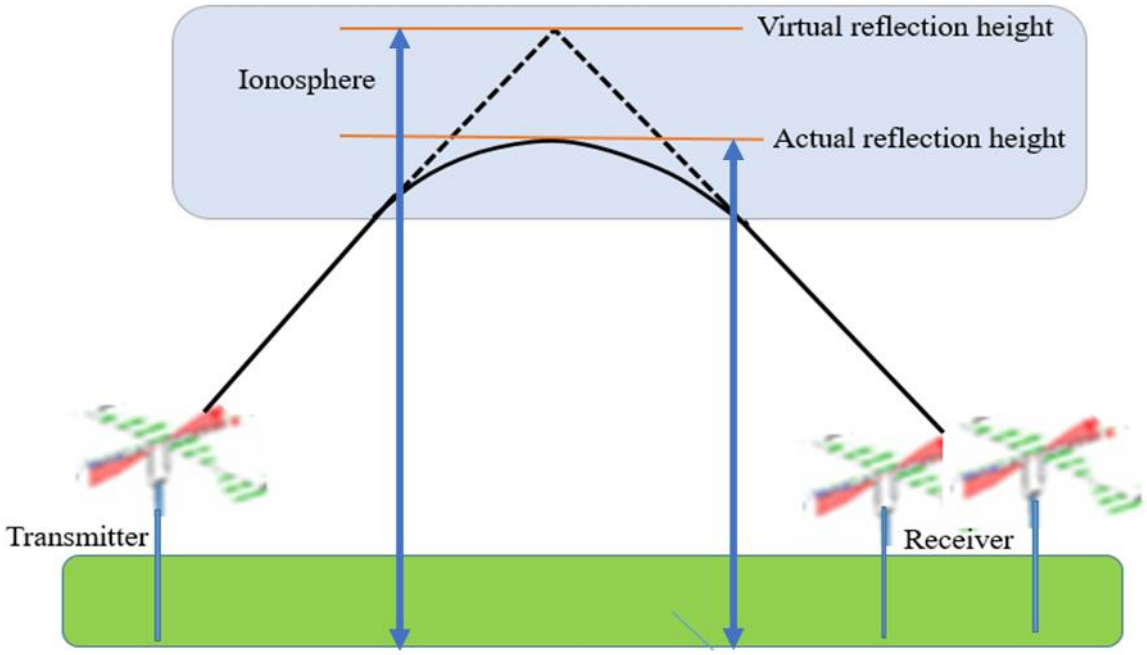

Figure 2.19 Actual and virtual height of the ionosphere.

2.2.3 Software Defined Radio (SDR) Earth Imager

Software Defined Radio is a radio communication system where components that conventionally have been implemented in analog are instead implemented by means of software. It has numerous applications, including military, radar, threat detection, radio astronomy, and amateur radio. The two main advantages of using Software Defined Radio in many applications are flexibility and low cost [33].

Software-defined radio has two main parts: a transmitter and a receiver. Each part has an analog and a digital component. The radio receiver extracts the arrival time of a radio signal coming from an antenna. Figure 2.20 shows that the square on the left is used for analog signals, and the square on the right is used for digital signals.

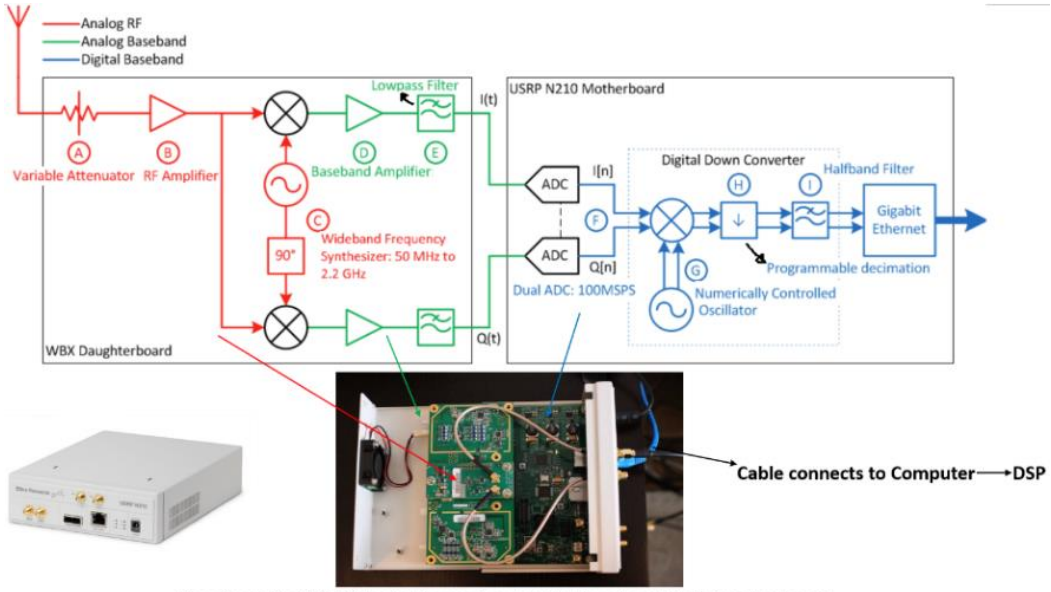

Receive path of USRP including analog daughterboard and digital motherboard

Figure 2.20 Analog and digital Receiver block diagram of Software Defined Radio showing ETTUS model USRP N210.

Two different methods were used to measure the phase of the carrier wave: a hardware method and a software method.

2.2.4 Hardware Method

The hardware method uses quadrature measurements to measure the phase difference between the emitted and detected radio waves. The difference in phase of the transmitted and received radio waves is a measure of the phase shift. The term 'quadrature signal' is generally understood The quadrature signal is also called In-Phase and Quadrature (I/Q). It is commonly used in radio frequency applications such as antenna beamforming, coherent pulse measurements, radar systems, and the direction of radio waves. The I/Q can be represented as a cosine (I) part and a sine (Q) part. where I (in-phase) represents a cosine wave and Q represents a sine wave. Two ways are used to represent the complex signal: Cartesian coordinates (x, y) and polar coordinates (r, θ). The amplitude and angle describe the polar coordinates.

$c = Ae^{i\theta}$

Where A is the magnitude and c is the complex number.

$e^{i\Theta} = \cos\Theta + i\sin\Theta$

Where cos Θ is the real part indicating the in-phase component, and sin Θ is the imaginary part indicating the quadrature component, illustrated in Figure 2.21 and 2.22.

The formula is

c = a + jb

as shown in Figure 2.21. The magnitude of the complex number is;

$$A = |c| = \sqrt{a^2 + b^2} \qquad (2.14)$$

The phase angle is the arctangent of the ratio of the imaginary and the part real part.

$$\Theta = tan^{-1}\left(\frac{b}{a}\right)$$

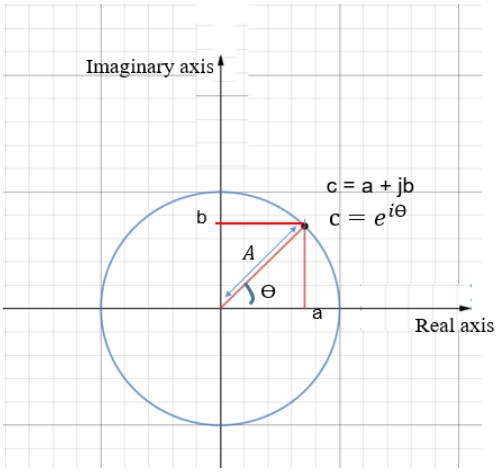

Figure 2.21 A signal representation by a phasor.

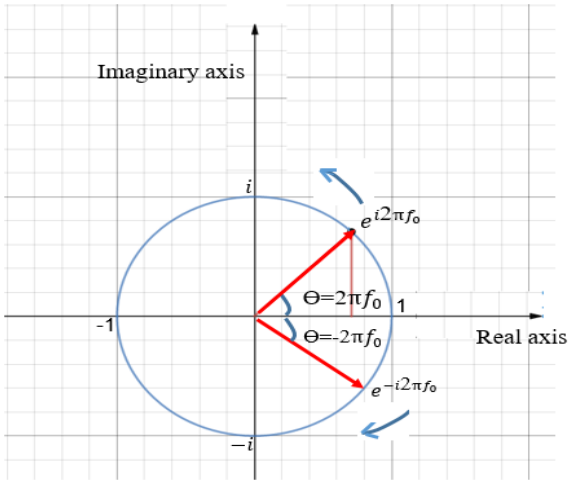

Figure 2.22 The quadrature signal.

The sinusoidal function in Figures 2.21 and 2.22. expresses the quadrature signal as $e^{i2\pi f_0 t}$ and $e^{-i2\pi f_0 t}$. The real-valued harmonic signal can be achieved by superposing two counter-rotating phasors in the complex plane. For better understanding, Figure 2.23 depicts an example of the phasor with its decomposed sine and cosine components.

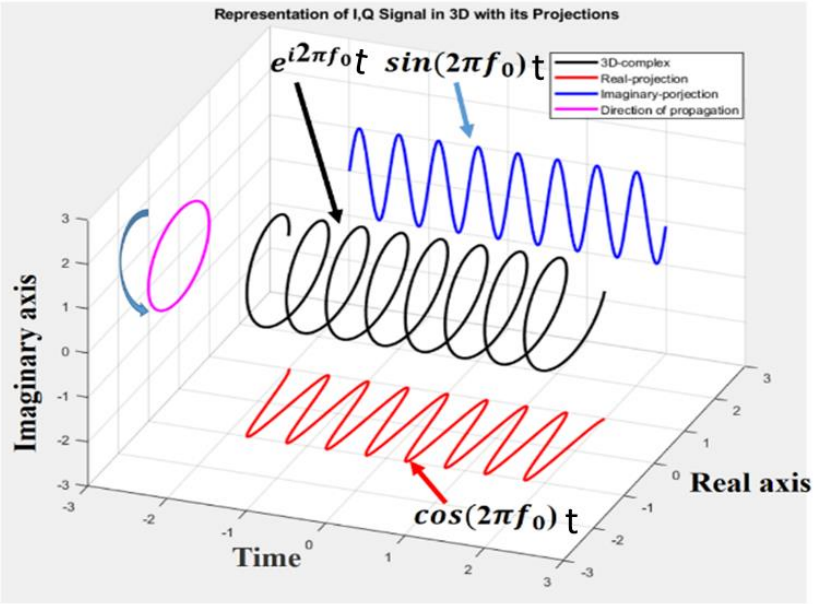

Figure 2.23 Phasor with sine and cosine as complex signals.

2.2.4.1 Carrier Wave Implementation of Phase Measurements

Communications deal with different techniques by modulating the radio wave carrier to carry information from one point to another. Those signals are often called carrier and modulation signals. The carrier signal is modulated on the transmitter side before being transmitted at the transmitter antenna. Later, the radio signal is received at the receiving antenna where the receiver is situated. The receiver is basically a demodulator to demodulate the received signal, whereas its output is the modulation signal. When two signals with frequencies f1 and f2 are mixed together, the output signal will contain frequency components that are the sum (f1 + f2) and the difference (|f1 - f2|) of the input frequencies. This process can be represented by a mixer whose output is a combination of signals; one is the signal of the summation of input frequencies, and the other is the difference between those frequencies, as shown in Figure 2.24.

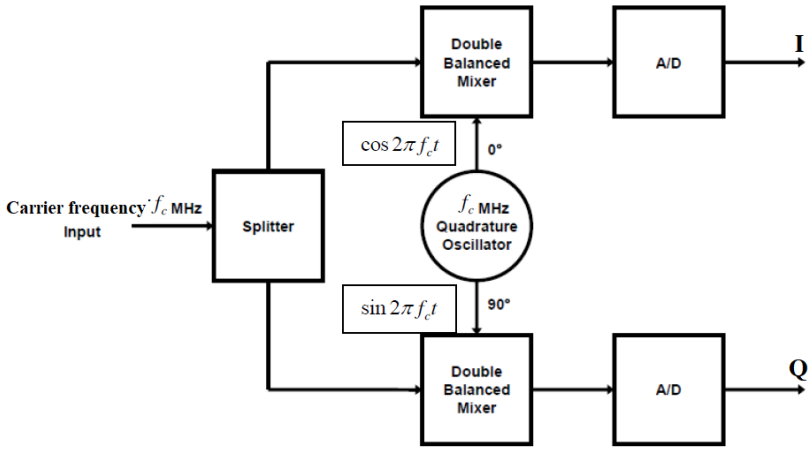

Figure 2.24 Super heterodyne receiver of radio wave showing I and Q channels [34].

.

Here, the single-tone carrier signal can be reflected from the ionosphere layer down to the receiver of the various antenna elements that build the array. Each element is expected to receive the same carrier signal but with some unknown phase difference (namely the relative phase). The above mixing approach can be used here to measure the relative phase difference.

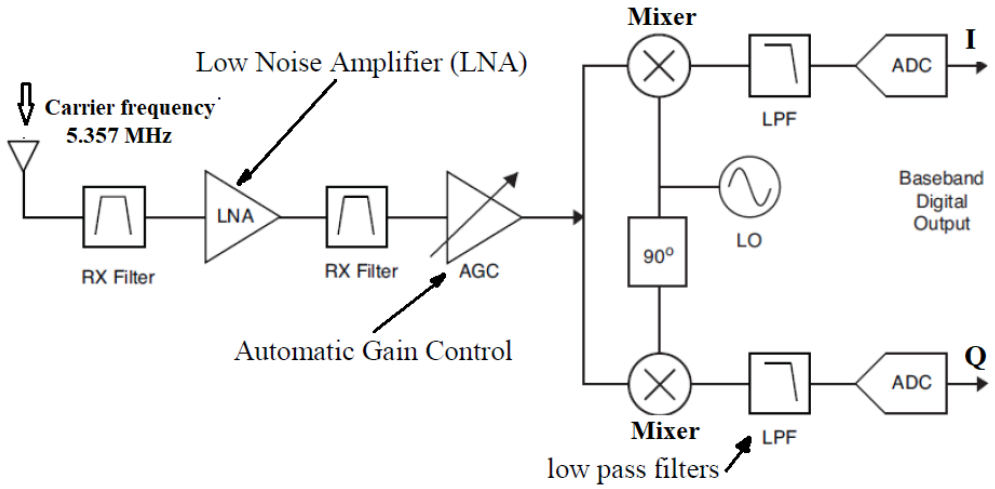

Figure 2.25 A more detailed illustration of the receiver adds several useful elements [35].

This technique can be implemented to convey information from the ionosphere utilizing the hardware method of measuring the phase difference. The radio wave can be represented as :

$$S(t) = \mathrm{Re}\left\{A(t)e^{i\theta(t)}\right\} = A(t)\cos\left(\theta(t)\right) \qquad (2.15)$$

$$\theta(t) = 2\pi f_c t + \phi(t). \quad (2.16)$$

$$S(t) = A(t)\cos(2\pi f_c t + \phi(t)) = \mathrm{Re}\left\{A(t)e^{j\phi(t)}e^{j2\pi f_c t}\right\} \quad (2.17)$$

Where $S_i(t)$ is the received signal at the receiver with a frequency f_c, amplitude $A(t)$, and phase $\phi(t)$. The complex components of the signal can be denoted by I and Q, referring to the "in-phase" and "quadrature" components, respectively.

$$S_i(t) = A(t)\cos 2\pi f_c t \cos\phi(t) - jA(t)\sin 2\pi f_c t \sin\phi(t) \quad (2.18)$$

$$= I(t)\cos 2\pi f_c t - jQ(t)\sin 2\pi f_c t \quad (2.19)$$

The cosine term is the component with zero phases called the in-phase component, whereas the sine term with a 90-degree phase is the quadrature. The input signal is mixed with the local oscillator (LO) at the receiver at 0- and 90-degree offsets (Figure 2.25). This multiplication of trigonometric functions results in two orthogonal functions as components of phase (I) and quadrature (Q). The two-channel output can be used to estimate the relative phase value β.

$$e^{j\beta(t)} = \cos\beta_I(t) + j\sin\left(\beta_Q(t)\right) \quad (2.20)$$

Where $\cos\beta_I(t)$ and $\sin\beta_Q(t)$ are the in-phase and quadrature channel outputs of the receiver, and $\beta(t)$ is the time-varying relative phase between the receiving antenna elements.

The concept of using a double-balanced mixer (multiplier) or mixer acts as a phase detector. A transmitter (modulator) and each detector (demodulator) use a double-balanced mixer in order to measure the phase. The Vector Network Analyzer (VNA) can assist in measuring the phase of several received signals. A VNA requires two or more receivers since a reference channel (R) is required to calculate the phase.

2.2.5 Software Method

The software technique utilizes a software-defined radio to measure the round-trip time of the radio wave from the transmitter to the ionization layer and back to the receiver. To achieve this, the ETTUS N210 is employed to generate a Barker's code, which is used for measuring the transmission time and receiving times at each antenna. The computer records these times and calculates the time differences for each receiver, resulting in a time difference image. It is expected

that this time difference image corresponds to the hardware phase image. Both measurement methods (Hardware and Software) rely on the temporal coherence of the imaging device. The periodic phase shifts within the phase image indicate waves within the Earth's ionization layer.

2.2.6 Ionospheric Disturbances

2.2.6.1 Ionospheric Response to Disturbances

To better understand the relationship between a disturbing event and its ionosphere response, a range of methodologies have been used to study these Earth and space disturbances. Rishbeth [3] addresses the likelihood that distinct waves might be produced by storms and dynamic climate models. Examples of these disturbances are natural earthquakes and man-made earthquakes.

2.2.6.2 Ionospheric Response to Earthquakes

Several studies have shown that measuring the critical frequency of the ionosphere wave has given a variety of results before and during an earthquake [3]. Earthquakes have been known to cause disturbances in the F region of the atmosphere, with precursors appearing up to five days before the earthquake [36]. As a result, it is critical to investigate any potential predictive characteristics in these signs because the mechanism of earthquakes that seismic activity of the Earth's plate tectonic motion generates electromagnetic radiation as pulses reach the ionosphere [37]. According to Chen et al. (2004), earthquakes have been observed to induce disturbances in the F region of the atmosphere, leading to the emergence of precursors up to five days before the seismic event. Investigating the predictive characteristics associated with these signals is of utmost importance. They conducted statistical tests for pre-earthquake ionospheric anomalies to investigate this phenomenon [36]. The mechanism underlying these precursors involves the generation of electromagnetic radiation from seismic activity resulting from the Earth's plate tectonic motion reaches the ionosphere.. During an earthquake, the release of energy from the Earth's crust causes seismic waves to propagate through the Earth. These waves, including primary waves (P-waves) and secondary waves (S-waves), travel through the crust, mantle, and core. As the seismic waves approach the Earth's surface, they interact with the atmosphere and ionosphere. The interaction between seismic waves and the ionosphere generates electromagnetic radiation in the form of atmospheric waves [34].

By studying the characteristics of these precursors, researchers aim to identify patterns and establish potential links between ionospheric disturbances and impending earthquakes. The hope is that by understanding the relationship between seismic activity and ionospheric anomalies, it may be possible to develop more reliable earthquake prediction methods and enhance early warning systems. Further research is still ongoing to unravel the complex mechanisms and processes involved in seismo-ionospheric coupling and the generation of ionospheric precursors.

Trigunait and co-workers [38] used three satellites and a ground-based radio station to detect electron density variations in the ionosphere before and after a quake. They found anomalous electron density fluctuations before an earthquake occurred, showing that electric and magnetic changes could happen a few hours or days before the earthquake occurs [38]. Other supporting research illustrated that ionosondes and GPS receivers measured a variation in electron density leading to ionosphere variations where the precursor of this phenomenon was noticeable from one to seven days before the earthquake [7], [24 , 25].

2.2.6.3 Correlation between Earthquakes and Ionosphere

Different methods have been proposed to classify the measuring of earthquakes. For many years, scientists have used traditional methods to predict natural disasters. For example, in 1906, crustal deformation was suggested by H. F. Reid to estimate pre-earthquake activities and to measure the accumulated forces produced by the seismic shift [40]. Also, the detection of gas emissions such as carbon dioxide and radon was considered one of the approaches to predict the precursors of earthquakes [39]. The current measurement network, which has several sensors distributed in many countries, aims to detect earthquake precursors and is costly compared to the proposed SDR Earth Imager, which may be able to warn about earthquakes [36].

Many papers have reported the mechanism of pre-earthquakes. The most important phenomenon in preparing for earthquakes is the electric field, which was first recorded in 1924 by Chernyavsky [39]. Other reports reveal that pre-earthquakes cause perturbations in the F-region of the atmosphere, and the signatures of these pre-earthquakes appear one to five days before the actual quake [36]. The mechanism of the pre-earthquake signatures, possessing structures of the ionosphere, is still not fully understood. Studies led to a hypothesis according to which seismic activity is produced by tectonic plate frictions that generate electric fields. These electric fields

that ionize the particles in the ionosphere are more noticeable in the E region of the ionosphere during nighttime [41].

Pulinets and Davidenko [42] demonstrated the link between the electromagnetic field of the ionosphere and the seismic waves created by the epicenter of an earthquake. They have based their scholarship history on this link, referring to the link as Global Electric Circuit. They showed the influence of earthquakes on changing the ionosphere's ionization. Harrison [43] reported a correlation between the seismic activity and the lower ionosphere responses over the pre-earthquake area and suggested measuring the change in the ionosphere by cutoff frequency 'tweeks'. The amplitude and phase of radio waves could be examined to detect the electron density of the lower ionosphere as well. Karpov et al. [44] proved a strong connection between Total Electron Content (TEC) variation of the ionosphere and events prior to earthquakes by numerical simulations that showed the density, longitude, and latitude of seismic and ionosphere areas. The investigation of variation in the F2 ionization layer during precursory activities before the 1994 Chi-Chi earthquake was recorded by Taiwanese scientists. The anomaly of critical frequency of the F-region in the atmosphere was documented during the pre-earthquake up to five days, and the disturbance to the ionosphere was influenced by earthquakes with a magnitude (M) ≥ 5.0 [36]. H. Rishbeth indicated the possibility of the ionosphere variations, particularly F2 layer being linked to an unexpected natural phenomenon such as earthquakes or a big man-made disaster [3]. It has also been thought that the reactions of ions in the seismic area of the earthquake preparation generated electric fields that could transport ions from the lower atmosphere and cause variations in the ionosphere [45]. It is possible to verify this theory by taking some samples of gases from the ionosphere during the pre-earthquake. However, this theory could probably face issues in choosing the proper place for instrumentation during the event. Also, the mechanism of electromagnetic emission generated by pre-earthquakes and transferred to the ionosphere is not yet fully understood. In 2015, Petraki et al. [46] published a review article that showed various frequencies recorded from earthquakes. They demonstrated the properties and characteristics of waves on the surface of the ionization layer created by seismic disturbances-and found a wide range of frequencies of earthquakes from kilohertz to megahertz (MHz).

2.2.6.4 Velocity and Altitude of Coseismic Ionospheric Disturbances Caused by Earthquakes

Several attempts have been made to find the velocity of coseismic traveling ionosphere disturbances (CTIDs) caused by earthquakes. Most of the previous research indicated that ionospheric waves propagate with an average velocity of around 2400 m/s.

In 2016, Yang-Yi Sun et al. [47] investigated the Nepal earthquake on 25 April 2015 by having vertically scanned electron density (Ne) in the ionosphere using a ground GPS receiving network and the space GPS Radio satellite. They found the Nepal earthquake pulses with a magnitude of 7.8 in the vertical directions penetrated the ionosphere at a supersonic speed of around 800 m/s, and the Ne structure was altered by 10% close to the maximum height of the F2 layer (hmF2). The excess of 30 km elevated the hmF2 within one minute, and the size of the disturbance in the vertical direction was 150 km. In contrast, a velocity of seismotraveling ionosphere disturbances (STIDs) propagated at 2.4 km/s in the horizontal direction.

Another study of the Nepal earthquake on 25 April 2015 was done in 2017 by Ram and co-workers [48] and found that the upper atmosphere at altitudes of 300 – 440 km from the Earth's surface was affected by the earthquake-induced acoustic waves. They observed ionosphere wave propagation on the south of the epicenter with an initial velocity of ~2.4 km/s, which is lower than the surface Rayleigh wave velocity of ~3.7 km/s. In addition, the study shows that the ionospheric wave propagates far away, about 800 km from the central ionosphere disturbances to the southward direction, and then the wave split into modes as fast (~2.4–1.7 km/s) and slow (~ 680 – 520 m/s).

In 2016, Chum and co-workers reported that an earthquake in Nepal on 25 April 2015 with a magnitude of M7.8 had an effect on the ionosphere layers over Taiwan and the Czech Republic. The signatures of the ionosphere were observed in Taiwan and the Czech Republic, far from the epicenter of the earthquake. The cause of the ionosphere disturbances was infrasound waves produced by the apparent movement of the ground surface. The study also found that the damping occurred to infrasound waves while propagating nearly vertically through the ionosphere at 200 km altitude of the F layer, as seen in Figure 2.26 [14].

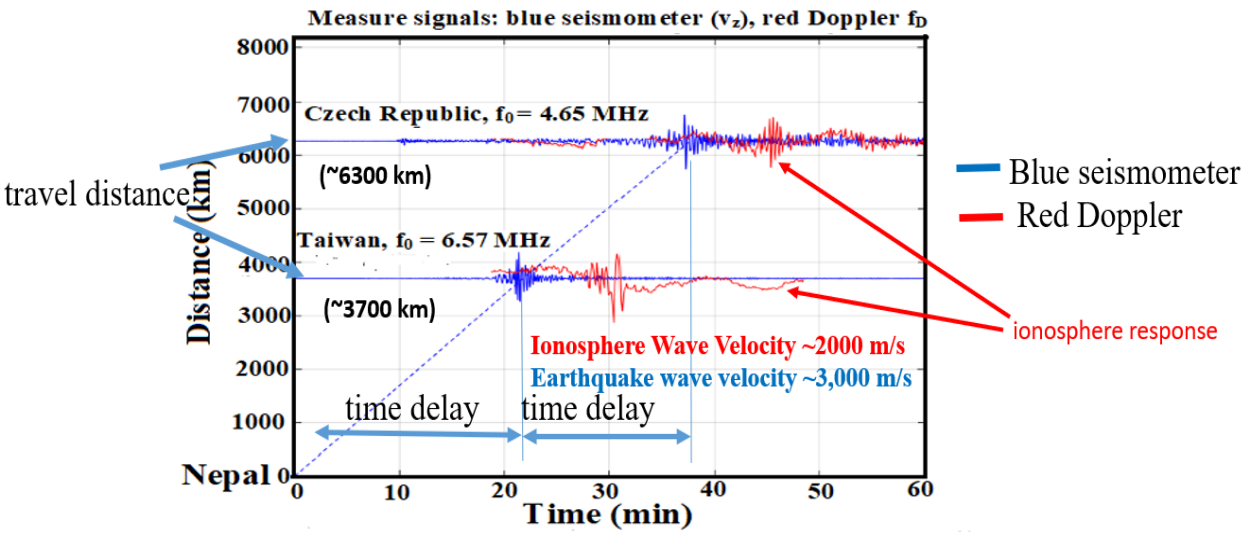

Figure 2.26 The ground wave and the ionospheric wave response to the Nepal earthquake in 2015 from two different locations [14].

2.2.6.5 Transfer Function of Earthquakes

The differences in time (software determined) and phase (quadrature measured) between each antenna produce two types of equivalent phase images. The differences in phase are due to the radio waves reflecting off the ionization layer's surface waves from two different points, the peaks, and valleys. Reflecting off the valley will travel a longer path length than reflecting off a peak, so it will take longer to reach the antenna. The small percentage of the phase shift, ~5%, is sufficient to measure the phase information with the Earth Imager [49]. Each set of ionization layer's waves represents a different Earth-disturbing event having its own characteristic amplitude, frequency, and travel direction. The transfer function of the Earth's disturbing event can then be determined from the following,

$$R(t) = A\, e^{i\Theta t}, \qquad A_o = d(x).c.\, A, \qquad \Theta = \omega = 2\pi f k, \tag{2.21}$$

Where A is the amplitude of the Earth-disturbing event, A_o is the amplitude of the Earth-disturbing event after coupling and damingg , c is the coupling of the Earth-disturbing event to the ionization layer, and d (x) is the damping of the wave as it travels along the surface of the ionization layer.

The power of the disturbing event can be determined by the square of the amplitude and the energy of the disturbing event can be measured by the wave's frequency.

As mentioned above, a Fourier transform of the phase image can be applied to separate the many sets of waves using their various frequencies and wave vectors within the Fourier image. An illustration of the disturbing event impressing its signal into the ionization layer represented by its transfer function is shown in Figure 2.27.

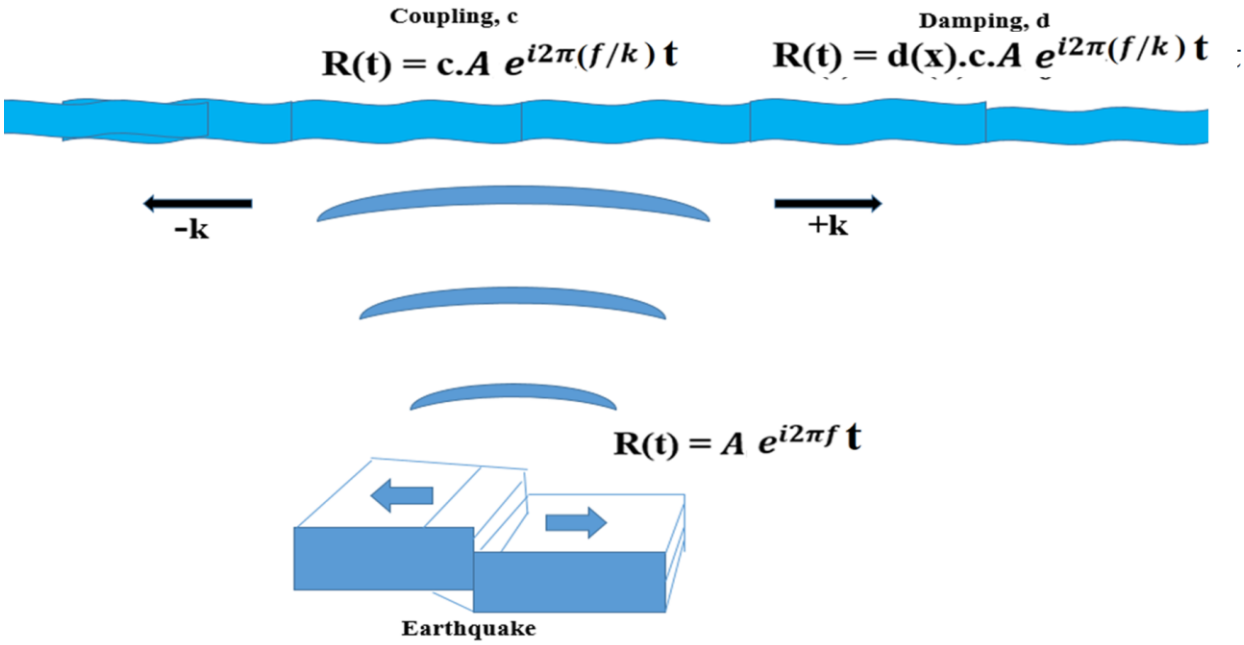

Figure 2.27 The transfer function of the earthquake.

2.2.6.6 Response of Ionosphere to Artificial Disturbances Made by Humans

A different area of study for the ionosphere response is artificial disturbances such as explosions, rockets, and missile launches, which reach the ionization layers as acoustic and gravity waves [50]. Since the 1960s, a great deal of research has been done on the relationship between disturbing events on Earth caused by humans and their impact on the ionosphere. In 1962, Bowman published a paper in which he described variations in the ionosphere and determined a pressure wave's propagation speeds, including previous explosions from 1958. The pressure wave from the blasts on the ground propagated upward and pushed the ionosphere, creating ionosphere

disturbances [51]. A more recent research study from 2006 has indicated that one of the sources of infrasonic waves coupling below from the troposphere to the ionosphere is underground nuclear and massive chemical explosions [52]. Rothkaehl and co-workers investigated a number of factors affecting the standard of satellite communications. They mentioned some disturbances generated by power sources, including broadcasting transmitters, power stations, power lines, and heavy industry, produced a very low-frequency emissions range in the Earth's plasma environment [53].

2.2.6.7 Ionospheric Response to Power Line and Losses

Growing concerns have been raised about how the man-made ionosphere and magnetosphere such as power line emission (PLE) and power line harmonic radiation (PLHR), are affected. An electromagnetic wave with harmonic frequencies of 50 or 60 Hz found in the ionosphere and brought on by electrical power systems on the surface of the Earth is known as Power Line Harmonic Radiation or PLHR. A sort of emission that happens at 50 or 60 Hz frequencies is referred to as Power Line Emission (PLE). The PLHR and PLE are believed to be related to ground electric power systems since their frequencies are in excellent agreement with comparable ground power system frequencies [54].

Since the 1970s, many reports have been issued on the monitoring of PLHR and PLE on the ionosphere and considered that power line harmonic radiation (PLHR) is a type of pollution that originates from the power system and is emitted into the near-earth space [55]- [56]. In 1975, the pioneer work of Helliwell et al. reported that VLF line radiation existed in the Earth's magnetosphere by the spectrograms of the received singles showing a frequency close to 60 Hz. It was suggested that a whistler duct in the magnetosphere is penetrated by harmonic radiation from the Canadian power grid near Roberval [57].

PARK (1977) demonstrated that Power Line Harmonic Radiation (PLHR) had the ability to stimulate the strongest waves, leading to frequent emissions in the magnetosphere. [58]. When Park and Miller (1979) examined the magnetospheric wave strength between 2 and 4 kHz, they found that the chorus (discrete narrowband emissions) activity shows a noteworthy minimum on Sunday compared to the rest of the week because of reduced electrical consumption on that day [59]. According to another study (J.P. Matthews and K. Yearby in 1981), the PLHR seen at Siple is typically comparable to the VLF line radiation characteristics of magnetospheric waves detected at Halley. Even though it seems like line spacings, occurrence frequency, and diurnal fluctuation

are separate [60]. Numerous parallel horizontal spectral lines with spacings of 50 Hz/100 Hz or 60 Hz/120 Hz, similar to the local terrestrial power, were found when these occurrences were analyzed using the time-frequency spectrogram of the electric field intensity [46, 50].

Another study indicated that PLHR penetration into the lower ionosphere may lead to increased electron precipitation and changes in the ionosphere and magnetospheric currents, which may have an influence on thunderstorm activity [51–54].

The PLHR and PLE events in the ionosphere over China were discovered using DEMETER satellite data, and the features and relationships between the two types of radiation were examined. 133 PLHR events were moved by the 50 Hz spectral line frequency in the electric field power density time-frequency spectrograms. They had a strong connection to the frequency of the ground power grid [66].

2.2.6.8 Response of Ionospheric to Weather and Storms

Severe weather and storms at lower Earth's atmosphere also create waves affecting the ionosphere. The common hypothesis is that active storms and weather systems generate waves in the lower atmosphere, which are carried up to the ionosphere [3]. In the 1940s, decade-long research at the Zi Ka Wei Observatory in Shanghai, China, applied an approach in weather forecasting with great success. They found that there was a connection between the critical frequency echoed and the movement of air masses. The carrier wave was transmitted to the ionization layers and fromed returned ionosphere echoes (E, F, and F). They could predict the cause to be the weather across a 400-square-kilometer area. The echo from the E layer indicated that the maritime air mass was close to them. To clarify, ionospheric waves serve as indicators of weather events happening at a distant location. If these ionospheric waves can also determine whether a storm is approaching the measurement location, they could be utilized for weather prediction purposes [67].

It is important to note that the specific capabilities of an ionospheric imager depend on the design, frequency range, antenna configuration, and processing techniques employed. Different types of ionospheric waves require different measurement and processing approaches. Researchers and scientists use ionospheric imagers to investigate and understand the behavior, dynamics, and effects of waves in the ionosphere, contributing to fields such as space weather monitoring, radio wave propagation studies, and ionospheric research.

The SDR Atmosphere Imager consists of multiple antennas as receivers, each representing a pixel in the generated image. However, due to the spatial distribution of the array antenna, the radio waves reflected by the ionosphere reach different antenna locations at different times. This variation in path and arrival time of the radio wave carriers is crucial for determining the phase shift between the emitted and received radio waves, which ultimately forms the image of the ionospheric waves.

In order to separate the different sets of waves present in the phase image, Fourier analysis is employed. Each set of waves in the phase image exhibits a distinct combination of frequency and wave vector. By applying Fourier analysis, a Fourier image is obtained, where the waves are separated based on their frequencies and wave vectors.

The relative phase information about the ionospheric waves is obtained through the configuration of the antennas. It is important to note that the specific capabilities of an ionospheric imager depend on the design, frequency range, antenna configuration, and processing techniques employed.

Chapter 3 Monitoring Earth Using Earth Imager

This chapter is based on a publication in the Journal of Atmospheric and Solar-Terrestrial Physics [9], and additional information on data collection and analysis has been included.

Radwan Sharif [a]*, S. Gokhun Tanyer[b], Stephen Harrison[c], Peter Driessen[b], Rodney Herring[a]
a MENG, University of Victoria, Victoria, V8W 2Y2, Canada
b ECE, University of Victoria, Victoria, V8W 2Y2, Canada
c Dominion Radio Astrophysical Observatory, Kaleden, British Columbia, V0H 1K0, Canada

Abstract

To obtain information about Earth's disturbances to the ionosphere of the atmosphere, a Software Defined Radio (SDR) Earth Imager was constructed at the Dominion Radio Astrophysical Observatory (DRAO). This imager used radio waves reflected from the Earth's ionization layer to phase image waves on/in the ionosphere. Two sets of waves were found, one having a constant frequency and another having a large spike. The constant frequency waves represent a continuously active ionospheric disturbance, such as a power generating station. The large spike waves were randomly occurring outliers. Candidates for the spike waves are lightning strikes and/or earthquakes. Having the capability to detect these waves opens up the possibility of measuring the power, energy and location of their disturbance.

3.1 Introduction

The ionosphere is an envelope surrounding the Earth and is its largest sensor existing at the highest region of the atmosphere. The ionosphere has been studied since the 1920s using ionosondes [2]. The ionosphere consists of ions and free electrons generated by the radiation from the Sun being absorbed by atoms and molecules such as nitrogen, oxygen, and nitric oxide [68].

Ionospheric measurements made by the ionosondes start at about 50 km altitude and extend to over 500 km altitude. The ionosphere is divided into three layers, D, E, and F. Each has varying ionization densities due to the Sun's radiation as a function of time of day and seasons and is also influenced by solar activity, including solar flares and solar wind [68]. These ionization layers are

not flat. Instead, they have waves that can be inferred from ionosonde measurements. An ionosonde measurement, though, only provides the equivalent information of one pixel in an image that is not able to provide any wavevector information of the waves. Previous studies have shown that the waves in the ionization layers are created by terrestrial disturbances such as earthquakes, volcanic eruptions, hurricanes, tsunamis, and man-made events. Disturbances from Space, such as solar flares, also can create measurable waves on the surfaces of the ionization layers (Rishbeth, 2006).

3.2 Ionospheric Response

The ionospheric response to Earth and space disturbances has been studied using various techniques to clarify the connection between a disturbing event and its ionospheric response. Rishbeth (Rishbeth 2006) discusses the possibilities of multiple waves being created from atmospheric dynamics and storms within the atmosphere. However, he also indicated that more investigation was required. An example of these disturbances is Earthquakes. Although there is still doubt among the scientific community of the validity of using radio waves to measure pre-earthquake disturbances, several studies have shown that measuring the critical frequency of the ionospheric wave before and during an earthquake shows precursors appearing up to five days before the earthquake (Rishbeth, 2006), [36].

A possible mechanism involves generating electromagnetic pulses during seismic activity that reach the ionosphere [37]. Trigunait and co-workers (Pulinets et al., 2004) also used three satellites and a ground-based radio station to detect electron density variations in the ionosphere before and after an Earthquake. They found anomalous fluctuations of the electron density before an earthquake occurred, showing that electric and magnetic changes could happen a few hours or days before the earthquake occurs (Pulinets et al., 2004). Other supporting research using ionosondes and GPS receivers measured a variation in electron density leading to ionospheric variations where the precursor of this phenomenon was noticeable from one to seven days before the earthquake [69]. As a result, further studies should be conducted to add more information to the potential predictiveness of using radio waves to measure the disturbances of the ionosphere.

A different study area is the ionosphere response to man-made disturbances such as explosions, rocket and missile launches, which arrive in the ionization layers as acoustic and gravity waves [50]. The correlation between human-made Earth disturbing events and their effects on the

ionosphere has been widely investigated since the 1960s. In 1962, Bowman published a paper in which he described variations in the ionosphere and determined a pressure wave's propagation speeds, including previous explosions from 1958. The pressure wave from the blasts on the ground propagated upward and pushed the ionosphere creating ionospheric disturbances [51].

A study by Laštovička [52] indicated that infrasonic waves created from underground nuclear and massive chemical explosions were able to couple with the ionosphere from the troposphere. Rothkaehl and co-workers [70] studied some factors that affect satellite telecommunication quality. They mentioned that some disturbances generated by power sources, including broadcasting transmitters, power stations, power lines, and heavy industry produce very low-frequency emissions in the Earth plasma environment.

It has also been reported that the penetration of power line harmonic radiation (PLHR) into the lower ionosphere caused increased electron precipitation and changes in ionospheric and magnetospheric currents [71], [52–54]. Almost all PLHR events have corresponding man-made power line emissions (PLE) at the fundamental frequency of the local power network [54].

Many methods are currently being applied to gather data on the ionosphere, including weather balloons and ionosondes [4]. Weather balloons are launched twice a day to collect information about temperature, air pressure, humidity, and the speed and direction of the wind in the atmosphere. These techniques provide only a few data points per day and, although the information is useful, it is not enough to give a clear picture of the behavior of the ionosphere. As well, the maximum height reached by weather balloons is about 53 km [5].

The useful information provided by ionosondes is an estimate of the height and critical frequency of each ionization layer. They are not able to locate the source of the waves they are detecting.

Other possible methods of measuring the properties of the ionosphere include using multiple satellites [6], HF Doppler radar, and over-the-horizon radar [72]. In an attempt to identify Rayleigh waves generated by earthquakes, radio wave imaging by Doppler has been found to have limited sensitivity only able to detect disturbances greater than the Richter scale magnitude 7 [16], which is not able to give enough information about the ionization layers and their corresponding Earth disturbing event.

Imaging the ionosphere's waves is not possible by the previously described methods. Therefore, this paper intends to present a novel approach to image the waves existing on the ionosphere by

using radio waves reflected from the ionosphere as the carrier wave and an antenna array on the surface of the Earth as the camera. Software Defined Radio (SDR) and GPS timing are the enabling technologies.

3.3 Experimental Method

3.3.1 SDR Experimental Method

The SDR Earth Imager comprises Software Defined Radio (SDR), GPS timers, and an antenna array to detect and monitor the waves existing on the ionosphere. Radio waves are transmitted from a point source on the surface of Earth up through the atmosphere at near-vertical incidence, reflecting them off the ionosphere and then detecting them upon their return to the Earth using the radio wave camera. The device measures the time and phase shift of the radio waves received by each antenna of the radio wave camera (Figure 3.1). The difference in the path length of the radio wave (L) propagating from the transmitter to each receiver in the array determines the phase shift at each pixel in the image. The spatially varying phase shift is used to construct a phase image of the reflecting ionospheric surface revealing the waves created by Earth disturbances.

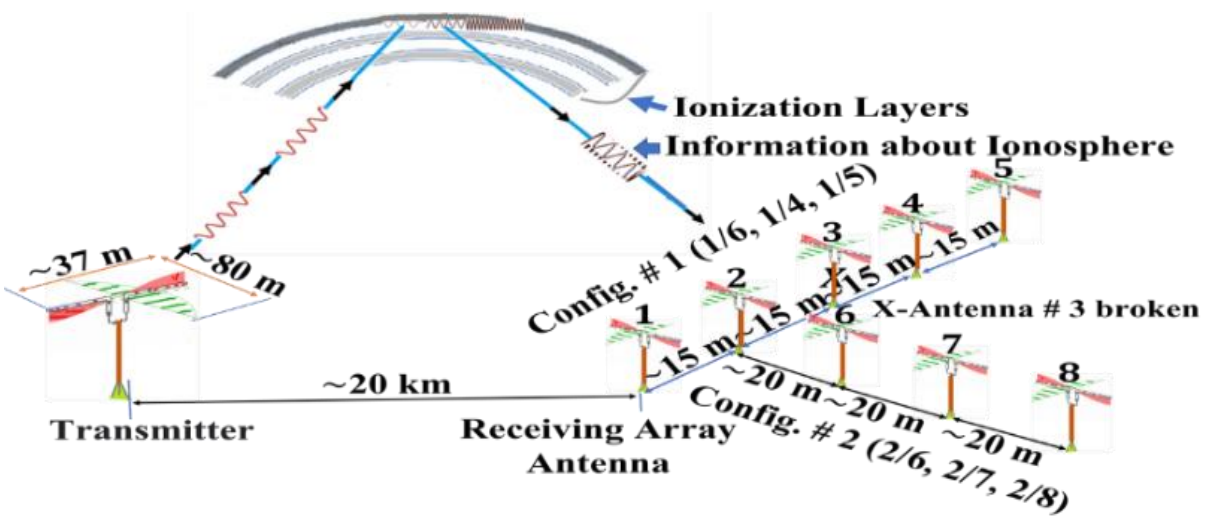

Figure 3.1 A transmitted radio wave is shown reflecting off the ionosphere to the camera consisting of an antenna array having 4 antennae aligned in the east-west direction (antenna 3 marked with an X was inoperable) and 4 antennae aligned in the north-south direction.

The transmitted radio wave can be considered as a carrier wave of the information, i.e., amplitude, frequency, and wavevector of the waves existing in the surface of Earth's ionization layer. The radio wave transmission was from Penticton, British Columbia, Canada and received by the antenna array at DRAO, Kaleden, British Columbia, Canada situated 19.86 kilometers away from the transmitter.

The method to measure the phase of the carrier wave used the quadrature of a beamformer, a device using multiple signal inputs received at the same time. The beamformer had 16 inputs, although only four antennas were connected. The beamformer measured the relative phase between all pairs of antennas.

The difference in phase, $\Delta\varphi$, determined the difference in the path length of the radio wave (L) propagating from the transmitter to each receiver in the array, expressed as

$$\Delta\varphi = 2\pi\,(\Delta L/\lambda) = 2\pi\, f\,(\Delta L/c) \quad \text{(3. 1)}$$

where f is the frequency, λ is the wavelength, and c is the speed of light ($\sim 3\text{x}10^8\,\text{m/s}$).

3.3.1.1 Dominion Radio Astrophysical Observatory (DRAO) Experimental Method

The experimental device consisted of three main components; one radio wave transmitter, one radio wave detector that comprised a two-dimensional array of receivers, and the beamformer that measured the phase of the transmitted and received radio waves shown in the block diagram in Figure 3.2.

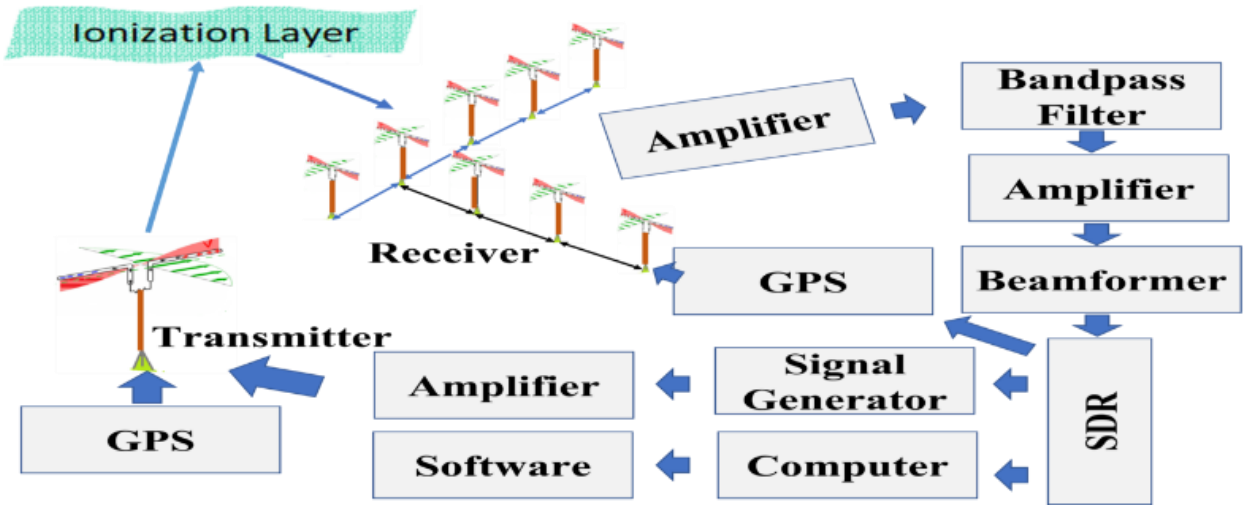

Figure 3.2 The experimental equipment used included a transmitter, receiving dipole antenna, filter and beamformer connecting to the SDR at DRAO.

The radio wave transmitter was a half-wavelength dipole for the amateur 80 m bands. The wire of the transmitting dipole antenna extended 37 m from East to West. It was powered by a signal generator that is connected to a GPS receiver providing a reference to synchronize the transmitted signals with the received signals.

The signal generator generated tones and sweeps of continuous waves having sinusoidal waveforms and a maximum power of 100 W. These transmitted radio waves included a ground wave and a skywave. The detector consisted of an antenna array of eight (two antenna arrays of 4) receiving antennas set up on non-conducting tripods 16 feet above the ground. The antennas numbered one to five were arranged in an East-West line with an approximate distance of around 15 m between antennae. The antennas numbered six to eight, branched off perpendicularly from antenna 2 to form a T shape alignment North to South with a spacing of roughly 20 m between the antennas. The dipoles were all oriented the same way along the East-West axis where the null of the array is approximately zero. The intensity of the ground wave was attenuated greatly by mountains located between the transmitter and the receiver. Each antenna had the same length of coaxial cable connected to the equipment allowing in-phase reception. The amplifiers after the bandpass filter were coupled to the beamformer. Initially, eight low-frequency amplifiers were connected between the bandpass filters and the eight antennas; however, the beamformer received weak signals, so the amplifiers for four of the eight antennae were transferred to the remaining four antennae to provide enough amplification of the signals for their detection. As a result, four

antennas could only be used at a time. Two configurations of four antennae were used. Configuration one used antennae 1, 6, 4, 5, which were perpendicular to the incoming carrier wave. Antenna 6 was replaced by antenna 3, which at the time wasn't working well in the linear array. The second configuration consisted of antennas 2, 6, 7, 8, which were parallel to the incoming carrier wave, Figure 3.3.

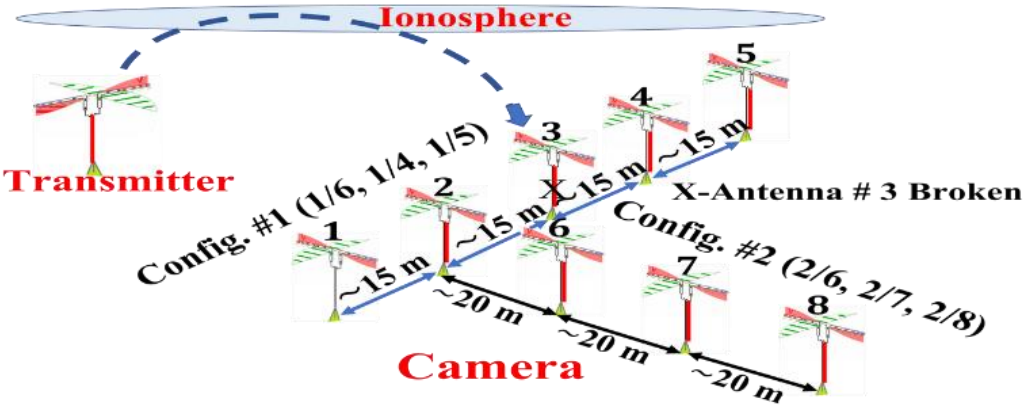

Figure 3.3 The receiving antennae array used as a camera having configurations consisting of one set of antennae 1/6, 1/4. 1/5 and another set of antennae of 2/6, 2/7, 2/8 with distances between the antennae shown.

The window length of the bandpass filter was from 3.85 MHz to 4.096 MHz and had 512 channels. Each channel had one-kilohertz bandwidth. Eight bandpass filters were used, as shown in Figure 3.4.

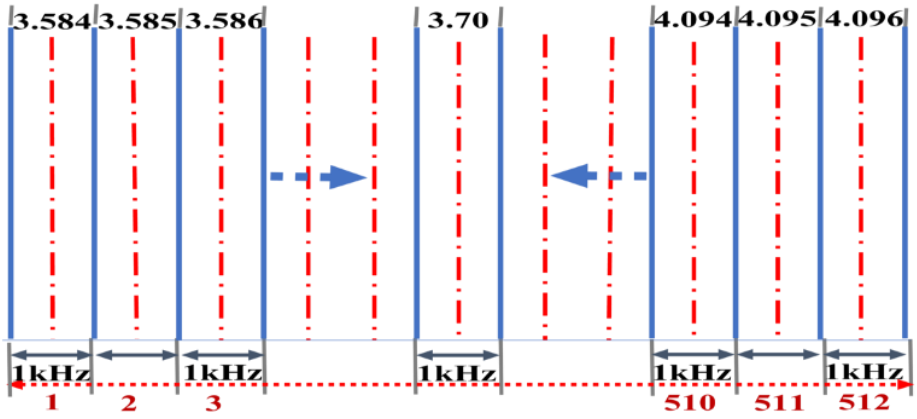

Figure 3.4 shows the 512 channels of a bandpass filter having a 1 kHz width.

There were three sets of data collected. The signals were digitalized with a sample rate of 1.024 MSPS (million sampling per second) at an integration time of 0.4s. Further details are in Table 1. The beamformer measured the relative phase between all pairs of antennas. Each of the two antenna configurations was used to generate three data sets. Each data set used a different range of frequencies with a sample rate of 0.4 seconds. The waves shown in Figures 3.5, 3.6, and 3.7 are representative of the two types of waves found, i.e., continuous waves and spike waves.

Table 3.1: DRAO Experimental Parameters.

Beamformer channels used		4
Frequency range test		3.584-4.096 MHz
Number of frequency channels		512
Sample rate		0.4 s
Configuration #1		
Frequency and Recorded Data		3.7 MHz for 71.2 and 12 seconds
Frequency and Recorded Data		3.8 MHz for 683.2 seconds
Frequency Sweep		3.70 to 3.706 MHz for 2002 seconds
Configuration #2		
Frequency and Recorded Data		3.7 MHz for 2001.2 seconds
Frequency and Recorded Data		3.8 MHz for 721.6 seconds
Frequency Sweep		3.72 to 3.726 MHz for 2002.4 seconds

3.4 Experimental Results

The three-dimensional (3D) ionospheric surface waves for antenna configuration one are illustrated by a time sequence of frames of the phase images, Figure 5. The dataset of 3.7 MHz for antenna configuration one was analyzed at different time series during 71 seconds. Plots a, b and c show three-dimensional axies; the x-axis is the horizontal line representing various time sequences and the y-axis is the horizontal line representing the distance between antennas, whereas the z-axis is the vertical line representing relative phase.

The relative phase differences between the antennae were determined from antenna pairs 1/6, 1/4, 1/5, i.e., relative to antenna 1. As a result, the four antennas have three relative phase

measurements. The animation of the phase differences for the receiver array revealed a travelling ionospheric disturbance whose peaks and troughs are constant, Figure 3.5. The oscillatory phase differences are observed to have a mean frequency was 0.7421 ± 0.32910 Hz, and their mean amplitude was 30.3899 ± 6.07599 degrees. These waves representing those disturbances appear to have a wavevector pointing in the North-South direction. Additionally, waves having a large amplitude like the spikes shown in Figure 3.5 c and Figure 3.7 were found passing through at unpredictable times, essentially being outliers in the timing of their appearance.

However, the analysis of the dataset of 3.8 MHz was performed, and the results did not show as clear waves as the dataset of 3.7 MHz.

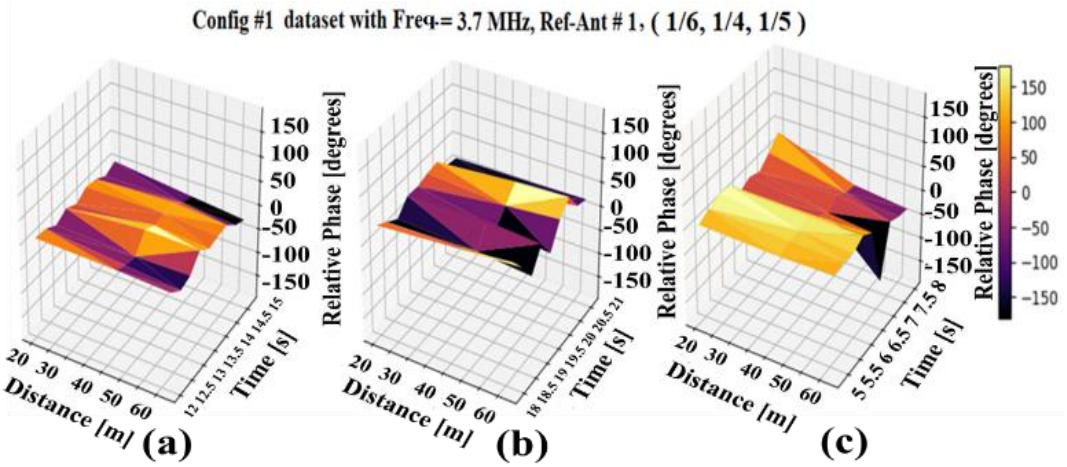

Figure 3.5 Graphs show waves moving in the surface of Earth's F ionization layer having a constant amplitude in (a) and (b), and a high amplitude spike in (c).

Another dataset generated by configuration 2 is presented in Figure 3.6 plotted relative to antenna 2 for the pairs 2/6, 2/7, and 2/8. The data also revealed the presence of the constant waves, which have a mean frequency of 1.4389 ± 0.97234 Hz and had an average amplitude of 26.6180 ± 7.0699 degrees.

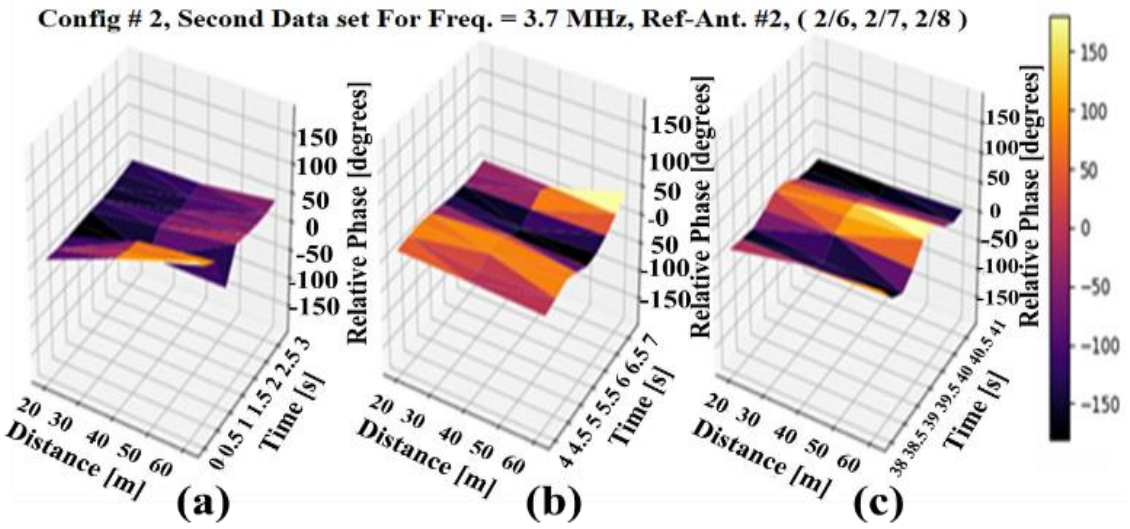

Figure 3.6 Waves found moving in the surface of Earth's F ionization layer having a constant amplitude, frequency and direction of movement in the different time sequences a, b, and c.

Again, spike waves were found. Figure 3.7 shows two examples. These waves occurred at irregular times and had a large, single-phase shift.

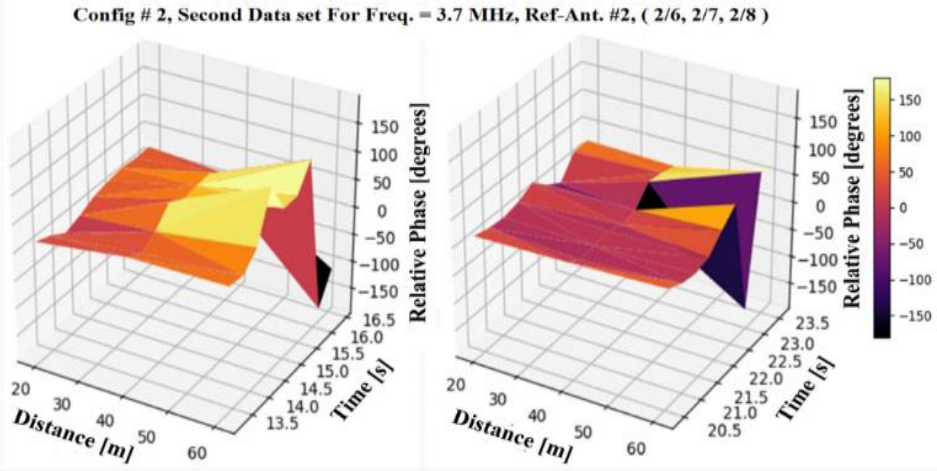

Figure 3.7 Waves having a high amplitude spike were observed as shown in the two graphs.

3.5 Discussion

Prototypes of the SDR Earth Imaging device were constructed and tested at University of Victoria UVic and DRAO in June 2018. In July 2018, data for this study was collected using two perpendicular sets of four linear antennae at DRAO. A SDR method of phase imaging the waves

existing in the surface of Earth's F ionization layer has been described and demonstrated. The receiving antenna array worked well as a camera where each antenna was equivalent to one pixel in the phase image; thus, the array of four antennae represented four pixels. Although severely limited in spatial resolution, individual waves were still discernable when imaged relative to one antenna. Two types of waves were revealed, one continuous and the other a single, randomly occurring large spike, essentially an outlier. Their frequencies and amplitudes were measurable even at this low resolution. In configuration 1, their wavevectors appeared to have North-South propagation. Accurate measurement of their wavevectors requires two simultaneous measurements from two locations using parallax, which additionally could be used to locate the origin of the waves, the source of the disturbance, at their intersection. With the limited data collected, the sources of the waves imaged could not be identified. The spike waves being outliers were possibly created by lightning strikes as these experiments were conducted in July, a time when a lot of local lightning was occurring.

The next step of this research is to acquire higher resolution phase images using more antennae for the camera, possible at the University of New Mexico using its Long Wavelength Arrays (LWA), i.e., the LWA-SV and LWA-1, which may enable the source of the disturbances creating the ionosphere's waves to be identified.

3.6 Conclusions

A SDR Earth Imaging device was constructed and demonstrated, enabling two types of waves in the ionosphere to be imaged, one having constant frequency and amplitude and the other having a randomly occurring spike. This device shows promise of being able to provide information about Earth's ionosphere being disturbed by events that created the waves on its surface, which have yet to be identified.

3.7 Declaration of Competing Interest

The authors declare that they have no known competing financial interests or personal relationships that could have appeared to influence the work reported in this paper.

3.8 Acknowledgments

Grants from the Natural Science and Engineering Research Council of Canada (NSERC) have made this work possible.

3.9 Additional Information for Data Collection and Analysis.

It is important to note that section 3.9 was not included in the published work upon which the rest of this chapter is based.

3.9.1 Receiver System

The receiver, which included the beamformer, and the receiver array was setup at DRAO. Dr. Stephen Harrison and his colleagues built the multi-channel beamformer to illustrate the phased array feeds. The reflected radio wave from the ionosphere was received by a multi-element phase-coherent sensor, and each receiver generated a pixel in the phase image. The beamformer had 16 physical channels that could be processed simultaneously.

When the beamformer was first connected to the receiving array, all eight antennas were connected. It was evident that an amplifier would be needed inline on each physical channel. A voltage was applied to the antennas to give enough signal for the receiver to have a noise level of 10 dB or less. A local AM radio station, CKOR operating at 800kHz, was the only signal detected if the amplifiers were not used [73]. The voltage injectors were connected to give a sufficient signal for the HF receiver. The signal represented as a waterfall showed some noise but with a very strong carrier frequency. The signal was later doubled amplified to provide 15 dB of gain into the ADC. Thus, the eight antennae were reduced to four antennas. Aliasing was an issue since the beamformer did not contain analog or digital filtering. Aliasing was addressed by providing 80 m separation filter between the antenna corresponding to the 3.5 - 4 MHz of the carrier wave. These antennae were connected inline before the amplifiers for the reason that if the pre-filtered signal from CKOR was amplified, the amplifiers were sent in a non-linear direction.

A handheld GPS was used to determine the antenna positions. GPS was also used by the transmitter and receiver for frequency synchronization.

In the diagram (Figure 2), there are two separate signal paths. The receiver path consisted of:

Rx antenna / receiver, Bandpass filter, Amplifier, and Beamformer

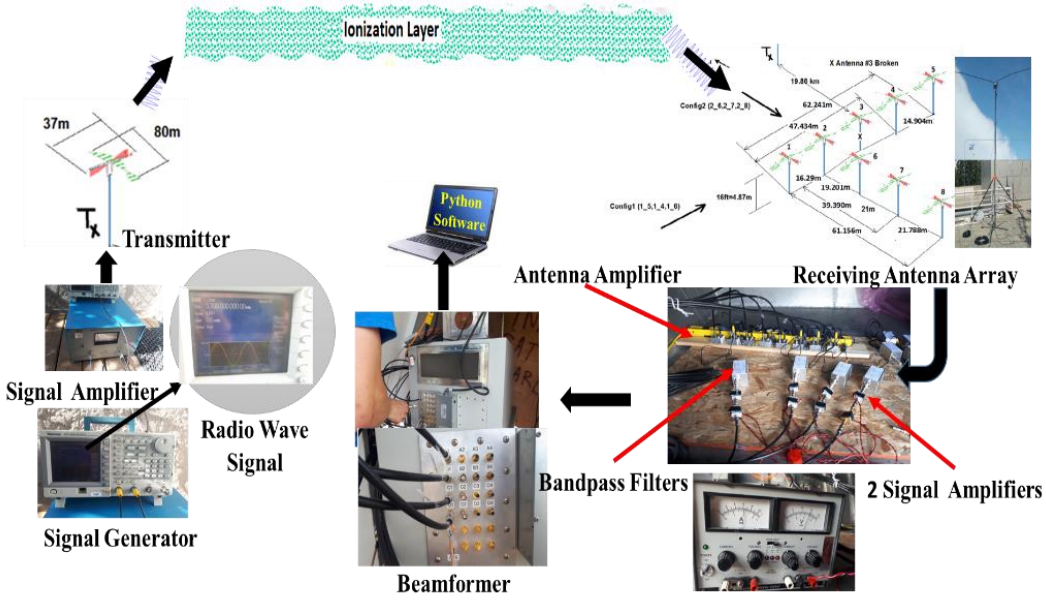

Figure 3.8 Experimental equipment and how are they were connected.

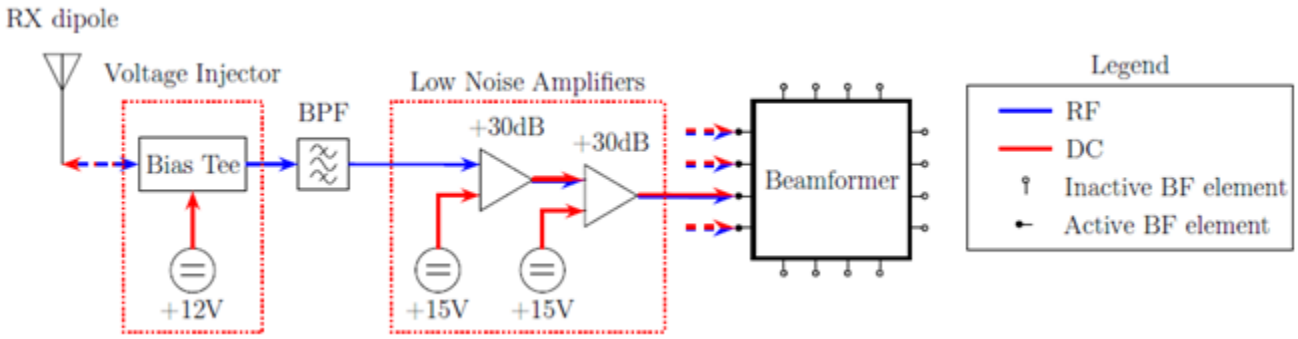

Figure 3.9 Block diagram of receiver system *[74]*.

A carrier frequency between 3.5 - 4 MHz was used because it had the best reflection off the ionozation layers measured by an ionogram [75] as well as from prior POC experiments conducted at the University of Victoria. The DRAO experiments were conducted during the su 0mmer time for 3 days in a row. Durations for collecting the data were chosen to take enough datasets for their analysis. Figure 3 below illustrates the relative magnitude and phase between antenna 1 and

antenna 5. In the figure, it is clear that the phase appears to be more coherent at lower frequencies. The strongest signals were between 3.5 and 4 MHz.

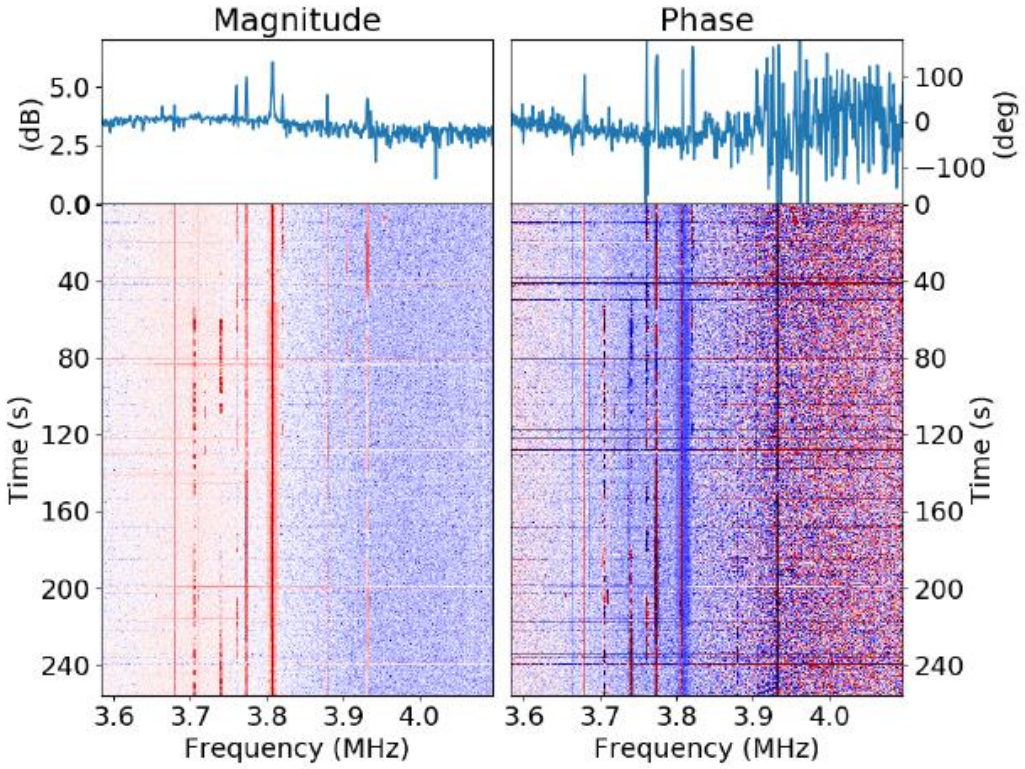

Figure 3.10 Relative magnitude and phase between antenna 1 and antenna 5 *[74]*.

.

3.9.2 Signal-to-Noise Ratio:

To make sure the noise levels were comparable, UVic engineers, Dr. Driessen and Nick Bruce, tested all of the antennas at UVic from the top of the engineering lab wing [74]. From the result of the DRAO experiment, it can be seen that low frequencies were dominant because of the low sample rate (2.5 Hz). The experiment showed good reliability of the data readings and it showed us how we could image ionospheric disturbances. These experiments were the first to show that we could image waves existing in the ionosphere.

3.9.2.1 Methods for Data Analysis

Several analysis methods were employed to reduce the noise in the data sets. Three specific methods were investigated, namely the moving average filter, Gaussian filter, and the addition of sample points as described below. The rolling average technique was utilized to analyze the noise present in the data.\..

3.9.2.2 Method of Moving or Rolling Average

The idea of the moving or rolling average method is to compute an average of a selected set of numbers to see how the overall trend behaves in a data set. It is a kind of filter in which one subset moves into another subset. Moving Average Filters are used in digital signal processing because they are simple and easy. This digital filter such as a FIR filter (Finite Impulse Response) works to reduce random noise in the time domain, whereas in the frequency domain it is considered the least suitable filter.

Configuration two with a frequency of 3.7 MHz was used and antenna two was used as a reference. The rolling average method was used for seven sample points. A Fourier transform was applied to the relative phases after using this method for antennas (2/6, 2/7, 2/8) to obtain frequencies that appear as waves on the surface of the ionization layer.

3.9.2.3 Gaussian Filter

Gaussian Filter is defined as a window function. The window function is a continuous function within a chosen interval, where the zero value is indicated outside of the chosen interval. The maximum peak is in the middle of the interval. The bell curve is a symmetrical curve about the middle of the interval line. The Gaussian function is given by

$$G(x) = \frac{1}{\sigma\sqrt{2\pi}} e^{-\frac{1}{2}\left(\frac{x-\mu}{\sigma}\right)^2} \qquad (3.1)$$

The full window (width) can be calculated by taking the full width half maximum height of the curve (FWHM) $= \frac{G(x)\,max}{2}$. Sigma describes the shape of carve and is called the Standard Width of the Gaussian The width of the Gaussian filter is determined by the chosen sigma. Data sets applying a Gaussian filter require a sigma value. Many sigma values are used to know how a

Gaussian filter works with the data sets and to find the dominant peaks that match the antenna pairs (2/6, 2/7, 2/8).

3.9.2.4 Method of Adding Sample Points

Approach of Summing Sample Points was employed to visualize the shape of the waves. In this approach, a time window was selected for each antenna pair (2/6, 2/7, 2/8). The chosen time interval for each antenna pair was successively added until the end of the data set. This process involved summing all the sample points within the windows and displaying the resulting sum.

Chapter 4 Locating Earth Disturbances Using Earth Imager

The content of this chapter was published in the Atmospheric Remote Sensing Journal [10].

Radwan Sharif 1,*, Suleyman Gokhun Tanyer 2, Stephen Harrison 3, William Junor 4, Peter Driessen 2 and Rodney Herring 1

[1] Mechanical Engineer (MENG), Center for Biomedical Research (CBR), Centre for Advanced Materials and Related Technology (CAMTEC), University of Victoria, Victoria, BC V8W 2Y2, Canada; rherring@uvic.ca

[2] Electrical and Computer Engineering (ECE), University of Victoria, Victoria, BC V8W 2Y2, Canada; peterd@ece.uvic.ca (P.D.); gokhuntanyer@uvic.ca (S.G.T.)

[3] Dominion Radio Astrophysical Observatory, Penticton, BC V0H 1K0, Canada; stephen.harrison@nrc-cnrc.gc.ca

[4] Los Alamos National Laboratory, Long Wavelength Array (LWA), University of New Mexico, ISR-2, Los Alamos, NM 87545, USA; bjunor@lanl.gov

***** Correspondence: rsharif@uvic.ca or rudwan_naj@yahoo.com

Abstract

The Radio Wave Phase Imager uses monitoring and recording concepts, such as Software Defined Radio (SDR), to image Earth's atmosphere. The Long Wavelength Array (LWA), New Mexico Observatory is considered a high-resolution camera that obtains phase information about Earth and space disturbances; therefore, it was employed to capture radio signals reflected from Earth's F ionization layer. Phase information reveals and measures the properties of waves that exist in the ionization layer. These waves represent terrestrial and solar Earth disturbances, such as power losses from power generating and distribution stations. Two LWA locations were used to capture the ionization layer waves, including the University of New Mexico's Long Wavelength Array's LWA-1 and LWA-SV. Two locations of the measurements showed wavevector directions of disturbances, whereas the intersection of wavevectors determined the source of the disturbance.

The research described here focused on measuring the ionization layer wave's phase shifts,

frequencies, and wavevectors. This novel approach is a significant contribution to determine the source of any disturbance.

Keywords: Software Defined Radio (SDR); Long Wavelength Array (LWA); radio wave imager; Ionosphere waves; phase imaging method; earth disturbances; wave vectors.

4.1 Introduction

The terrestrial ionosphere is part of the Earth's upper atmosphere where atoms and molecules are ionized by incoming solar radiation. This region is divided into three layers based on ion densities [20]. The ionosphere is the highest region of Earth's atmosphere as it starts at about 60 km and reaches over 500 km of altitude that are divided into three layers named D, E, and F [1]. The D layer of the ionosphere is at approximately 50 to 90 km altitude. The altitude of the E layer stretches from ~95 km to 150 km above the ground. However, the F layer is between 140 and 600 km above the surface of the Earth and is the most significant layer because of its availability during day and night [20]. These layers contain observable waves created by space weather events, including solar flares, coronal mass ejections originating in sunspots, and Earth-disturbing events, such as earthquakes, hurricanes, volcanoes, and man-made disturbances [3].

4.1.1 Ionospheric Disturbances

The ionosphere is a major area of interest within the field of waves. It is the envelope of ionization layers that surrounds the Earth, and the surfaces of these layers are not flat and are thought to be the most sensitive Earth entity to disturbances. Waves that exist on the surface of the Earth's ionization layer are the primary concern of this research. It is a widely held view that horizontal and vertical waves are created by solar, geomagnetic, and meteorological events. A number of researchers have reported that gravity waves, such as earthquakes and tsunamis, have waves that affect the ionosphere [76]. Weather events, such as hurricanes and typhoons, might produce waves on the surface of ionization layers [6–8]. One observer has already drawn attention to the waves associated with meteorological events, such as hurricanes [77]. Finally, waves may be created by other atmosphere-disturbing events, including volcanoes, forest fires, and lightning events [3], [78]. Rishbeth found some evidence that the majority of the waves on the surface of the ionization layer were induced by meteorological events [3].

Dungey explored the dynamics of the magnetosphere system while interacting with solar wind plasma carrying a southward interplanetary magnetic field. The model discussed in this study clearly illustrated the link between auroras and neutral points in the magnetic field [79].

A geomagnetic storm occurred on 17 March 2015 above Millstone Hill (42.6°N, 71.5°W, 72° dip angle) that revealed different phenomena from prior ones based on relationships between total electron content (TEC), the highest density in the F2 region (NmF2), electron temperature, and vertical ion velocity by employing data collected from satellites that operated at various altitudes and ground-based devices. The topside ionosphere had a significant plasma density increase, although it was not close to the F2 peak. The authors interpreted that the electrons' ability to transport heat was considerably reduced due to the exceptionally low ionospheric densities below the F2 peak. Therefore, the heat was trapped in the topside with a heat source above. As a result, the topside scale height raised even though electron concentrations in the F2 peak reduced, and TEC grew in the SED (storm-enhanced density). An increase in the density of molecular neutrals that led to recombination was most likely what reduced the amount of NmF2 [80].

The Thermosphere Ionosphere Electrodynamics General Circulation Model (TIEGCM) included an empirical representation of subauroral polarization streams (SAPS). The global thermosphere and ionosphere were simulated by the SAPS-driven TIEGCM during a moderately geomagnetically active time for five days (329 to 333) in 2008. The thermosphere's overall temperature rose as a result of SAPS and increased with time, but the subauroral and auroral zones showed a higher increase in neutral temperature; additionally, at higher elevations, neutral temperature and wind reactions to SAPS were more substantial and showed seasonal/hemispheric asymmetry. Wang et al. mentioned that significant variations in thermospheric winds were caused by a strong ion drag impact in the subauroral SAPS channel in the SAPS-driven TIEGCM. Finally, their report also indicates that the composition of the thermosphere changed due to heat from SAPS that caused air rich in molecules to rise in the subauroral and auroral areas and fall in other latitudes [81].

A research investigation that utilized incoherent scatter radars at Millstone Hill (MHO), Arecibo (AO), and the Defense Meteorological Satellite Program's (DSMP) in situ topside ionospheric data concentrated on ion-neutral coupling processes linked with strong electrodynamic forces. A variety of ionospheric and thermospheric disturbance features were noted and compiled throughout the storm, especially in the afternoon and dusk sectors over North America [82].

A study of the impact of solar flares on magnetospheric dynamics and the electrodynamic interaction between the magnetosphere and ionization layers was conducted using an entire geospace model in conjunction with observational data from the 6 September 2017 X9.3 solar flare event. The study supported the idea that solar flare impacts do not only affect the atmosphere where radiation energy is absorbed. They also propagate across geospace via the electrodynamic connection [83].

Extreme perturbations in the equatorial ionosphere caused by the 15 January 2022 eruption of the Tonga volcano created waves traveling from the ocean surface to the whole atmosphere for more than 12 h. This occurrence offered a research opportunity to increase knowledge of local and global ionospheric responses caused by volcanoes. Many investigations were reported about ionospheric perturbations following the eruption. Aa et al. [84] used Global Navigation Satellite System total electron content data, Global-scale Observations of the Limb and Disk ultraviolet images, Ionospheric Connection Explorer wind data, and ionosonde data to study variations in EIA crests accompanying the ionosphere to show waves traveling for more than 10 h over a distance 14,000 km away from the Epicenter [84]. Zhang et al. (2022) noticed worldwide propagation of Lamb waves that affected the ionosphere for days. Ionospheric waves (disturbances) were seen to circle the world three times. According to Zhang et al. (2022), the waves left Tonga every 1.5 days [85]. Aa et al. (2022) [84] and Harding et al. (2022) [86] discovered that powerful horizontal neutral wind perturbations caused by volcanic eruptions might significantly alter the equatorial electric field. Themens et al. described that the eruption caused large ionospheric disturbances and a number of subsequent medium ionospheric disturbances. The initial observations of these ionospheric waves started traveling at about 950 m/s propagating thousands away from the eruption site [87].

4.1.2 Ionospheric Response to Man-Made Disturbances

Researchers have been looking at the link between human-caused Earth disturbances and their impacts on the ionosphere since the 1960s. Studies showed that the ionosphere's response to man-made disturbances, including explosions, rocket launches, missile launches [88], power line emission (PLE), and power line harmonic radiation (PLHR) [89], arrive as acoustic and gravity waves in the ionization layers. Blecki, Rothkaehl, and his colleagues looked at some aspects that influence satellite telecommunications quality. They reported that power sources, such as

broadcasting transmitters, power stations, power lines, and heavy industries, formed a very low-frequency emissions range in the Earth plasma environment [70].

A recent study is also worth mentioning because its technique involved studying an isodensity in the lower E area using about 2 and 3 MHz pulsed Doppler radar and three receivers that measured the phase and amplitude and showed waves exiting on/in the ionosphere caused by two 1-ton TNT equivalent explosions. The output of small-size explosions around three orders of magnitude produced infrasound waves that reached the ionosphere. This is the first proof that explosions of this size had apparent effects on the lower ionosphere [90].

4.1.3 Ionospheric Response Space Weather Disturbances

Studies of space weather events related to ionospheric disturbances continue to be important because they could help better understand the relationship between Earth and space disturbances. For example, a geomagnetic storm caused by solar wind determines strong disturbances of the magnetosphere–ionosphere–thermosphere system. The atmosphere's composition changes as a result of the heating [91], [92]. Fuller-Rowell et al. demonstrated how the upper atmosphere reacts to geomagnetic storms starting at a different universal time. The high temperature of the upper thermosphere causing by Joule heating made a large-scale wind surge which resembles a gravity wave that spread to low latitudes [92]. Another study reported that Intense geomagnetic storms significantly impact ionospheric electrodynamics due to the interplanetary electric field penetrating the lower ionosphere [91],[93].

Another type of disturbance in space is a Transient Luminous Event (TLE). These events are the phenomena of lightning that can occasionally be observed in the upper atmosphere at altitudes ranging from tens to hundreds of kilometers or they can occur above a thunderstorm. We expect these types of disturbances to be a spike and not continuous waves and to be outliers as they are swift events that happen quickly. Many theories have been suggested regarding TLE creation. Still, the most commonly recognized concept is that elves are mainly created by electromagnetic pulses (EMPs) from lightning strikes. Additionally, sprites and halos are caused by quasi-static fields (QEs) from lightning strikes as well [94]. According to TLE energy estimates, the strength of these events can reach up to 0.01 W/m^2, which is large compared to the value of about 0.001 W/m^2 that occurs during some space weather disturbing events [94].

The aim of this study is to determine the location of the source of ionospheric disturbances from the intersection of wavevectors of waves existing in/on the ionosphere (or the F-layer). The intersection of wavevectors indicates the source of the disturbance.

4.2 Materials and Methods

4.2.1 SDR Experimental Method

The SDR Earth Imager collects data from the ionosphere by sending radio signals up into the atmosphere at a near-vertical incidence from the Earth's surface. These radio waves reflect off the ionosphere and return to Earth's surface, where they are imaged using an antenna array camera (Figure 4.1).

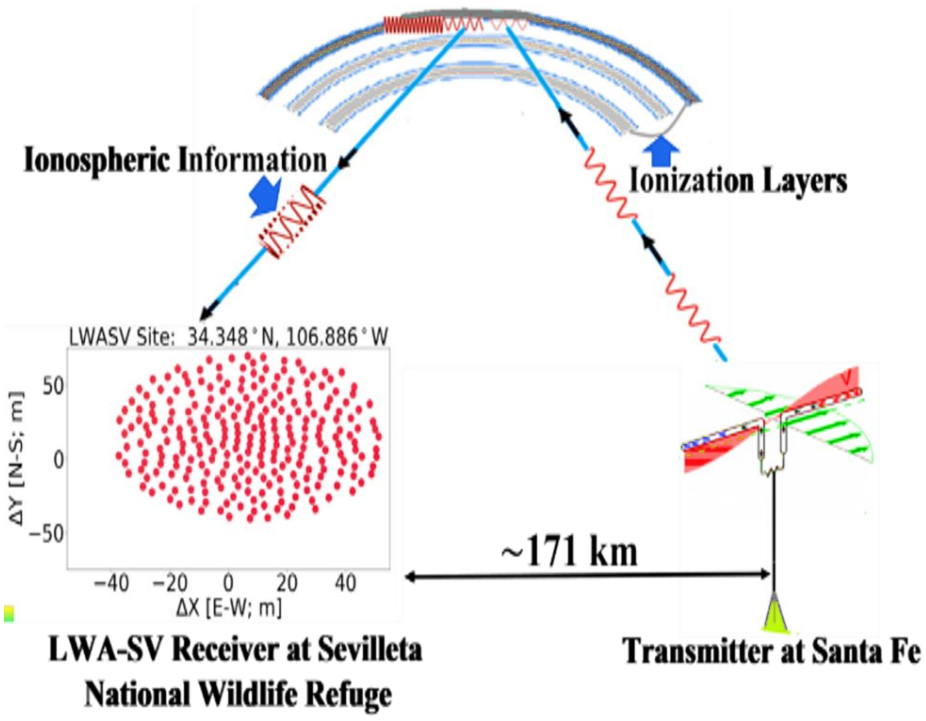

Figure 4.1 . A transmitter transmitted a carrier radio wave from the Earth, and the carrier radio wave was reflected off the ionosphere captured by receiving antenna arrays.

The phase of the carrier wave was measured using the hardware method. This method uses the quadrature to measure the phase difference between the emitted and received waves. The phase shifts within the phase images show the presence of the waves on/in the ionization layer. The phase

shift was determined using the relative phase difference between each pair of antennas at one time. The absolute phase at each antenna could be measured if the transmitter and all the antennae were synchronized.

The phase difference, $\Delta\varphi$, is determined based on the difference in the path length of the radio wave (L) propagating from the transmitter to each receiver in the array, which is expressed as

$$\Delta\varphi = 2\pi\left(\frac{\Delta L}{\lambda}\right) = 2\pi f \left(\frac{\Delta L}{c}\right) \quad (4.1)$$

Where f is the frequency, λ is the wavelength, and c is the speed of light.

4.2.1.1 LWA-SV and LWA-1 Description of New Mexico Experiments

Datasets were captured at the Long Wavelength Array (LWA)-SV station at the Sevilleta National Wildlife Refuge 34.35°N, 106.89°W [72] LWA-1 station. The LWA-SV and LWA-1 (University Radio Observatory) in central New Mexico captured radio wave frequencies from 3 MHz to 88 MHz, and each array consisted of 256 pairs of dipole-type antennas, while each pair of antennas had orthogonal polarizations on one stand. Antennas of the LWA-SV were arranged in a 110 m by 100 m north–south area distributed in about 100 m of aperture, as seen in Figure 4.2 [72]. Array geometry of the LWA-1 was within a 100 m (east–west) × 110 m (north–south) elliptical shape, as illustrated in Figure 4.3 [95]. It was designed to produce high-sensitivity, high-resolution images operating over a wide range of frequencies [96]. Both radio telescope arrays had a minimum of 5 m of separation between the antennas, which allowed for easy access of elements for maintenance purposes and also decreased beam desensitization because of sky noise correlation [97]. They received a carrier wave after reflection off the ionosphere from a transmitter placed in Santa Fe and transmitted radio waves with frequencies between 3 and 7 MHz. However, only one dataset (5.357 MHz) was analyzed as it had an obvious carrier wave. Transmitter and receiver locations, sent signal, and data specifications utilized during the LWA-SV and LWA-1 experiments are illustrated in Tables 4.1 and 4.2 below.

The distance between the Santa Fe transmitter and WA-SV is about 171 km, whereas the LWA-1 station is about 235 km away from the transmitter. The separation between the two stations—LWA1 and LWA-SV—is around 75 km, as shown in Figure 4.4 [95].

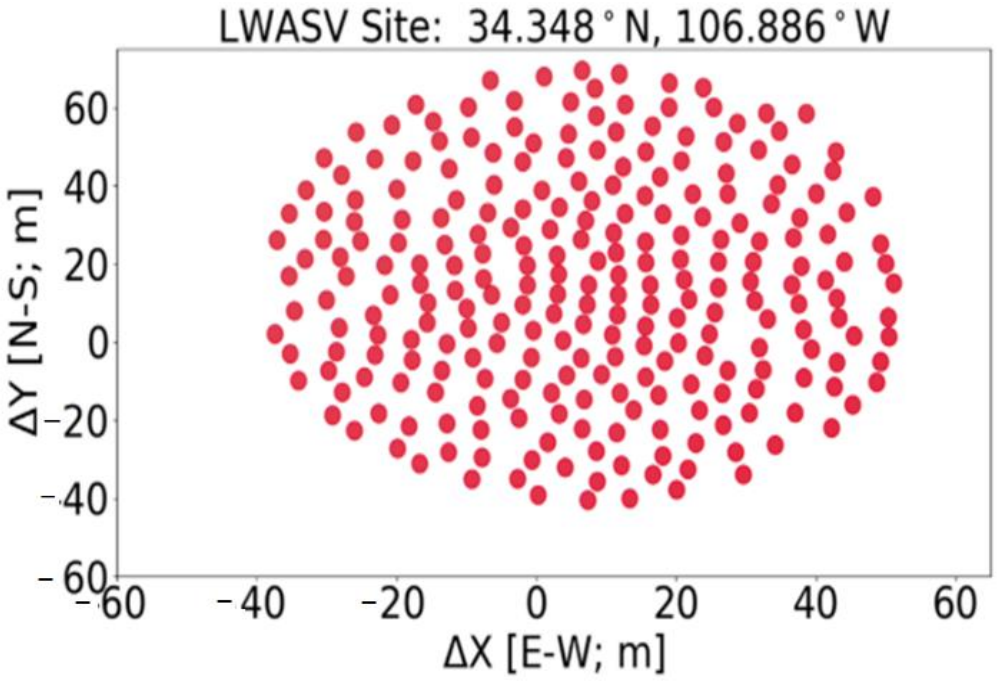

Figure 4.2 Antenna locations of LWA−SV which show the position of each antenna as a red circle in x and y direction.

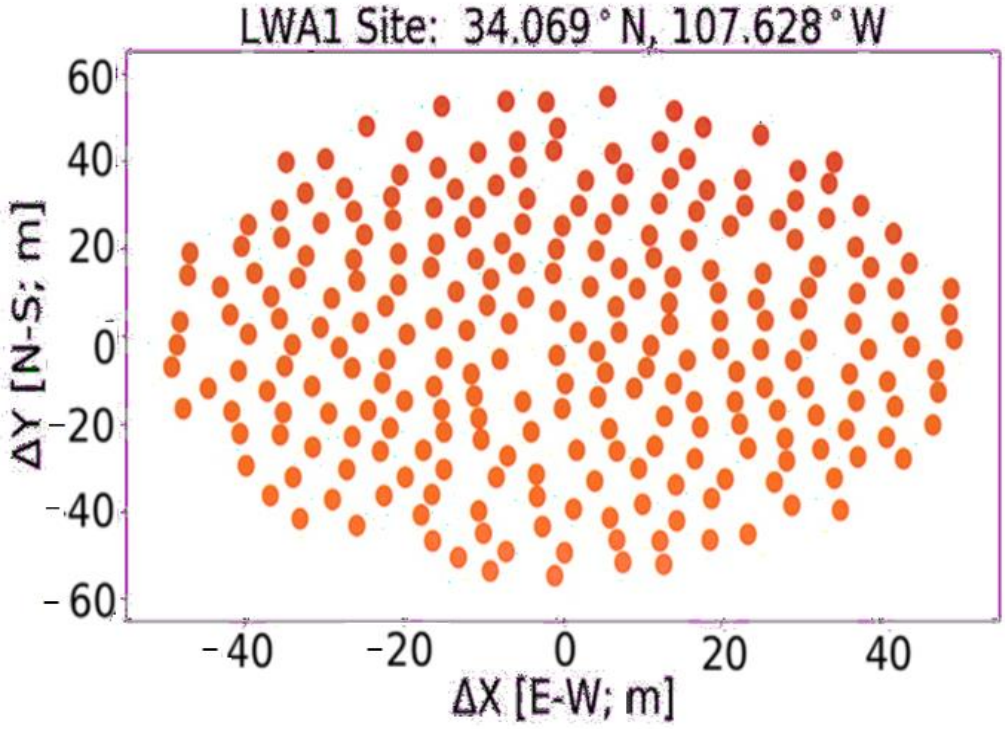

Figure 4.3 Antenna locations of LWA−1 present the position of each antenna as a red circle in x and y directions.

Table 4.1 Transmitter signal and data set specifications used during the LWA-SV experiment.

Santa Fe Transmitter (35.71144°N, 106.0084°W)	
Date and Time	UT 01 August 2021, 20:29:30
Transmitted Frequency	5.3570 MHz
Mode-Send	CW Tone (Continuous Wave)
Receiver LWA-SV (34.348°N, 106.886°W)	
Center Frequency	5.33999 MHz
Polarization	Zero
Date and Time of First Frame	8 January 2021, 20:29:20
Sample Rate	100,000 Hz
Recorded Time	1765.895 s

Table 2.

Table 4.2 Transmitter signal and data set specifications used during the LWA-1 experiment.

Santa Fe transmitter (35.71144°N, 106.0084°W)	
Date and Time	UT 01 August 2021, 17:57:32
Transmitted Frequency	5.3570 MHz
Mode-Send	CW Tone (Continuous Wave)
Receiver LWA-1 (34.069°N, 107.628°W)	
Center Frequency	5.33999 MHz
Polarization	Zero
Date and Time of First Frame	8 January 2021, 18:00:00
Sample Rate	100,000 Hz
Recorded Time	1731.281 s

Figure 4.4 The distance between the transmitter and both LWA stations as well as the distance between LWA−1and LWA-SV.

4.3 Results

4.3.1 LWA-1 and LWA-SV Experimental Results

The LWA Software Library (LSL) was created to manage the specific data formats produced by LWA-1 and LWA-SV and to make them available for basic analysis tools [98]. A total of about 28 min of each data (LWA-1 and LWA-SV) using a sampling frequency of 100 kHz was obtained by digitally acquiring more than three giga-samples in total. After the initial analysis step, data were found to be consistent throughout the recording time after pre-conditioning (channel selection, noise reduction, etc.). The calculated wavevector (LWA-SV) remained pointed in a north–south direction around 90% of the time, which was in agreement with the physical locations of the transmitter and the receiver array. However, the wavevector for the LWA-1 signals pointed

northeast–southwest between 30 to 65 degrees 70% of the time, which showed the effects of the ionospheric disturbances that occurred during the recording time.

The first step of the data analysis was to represent the data as a waterfall plot. Figure 4.5 shows a visual illustration of the transmitted signal strength represented by colors over time and varies with the spectrum of frequencies used to look at the carrier wave extracted from the frequency range.

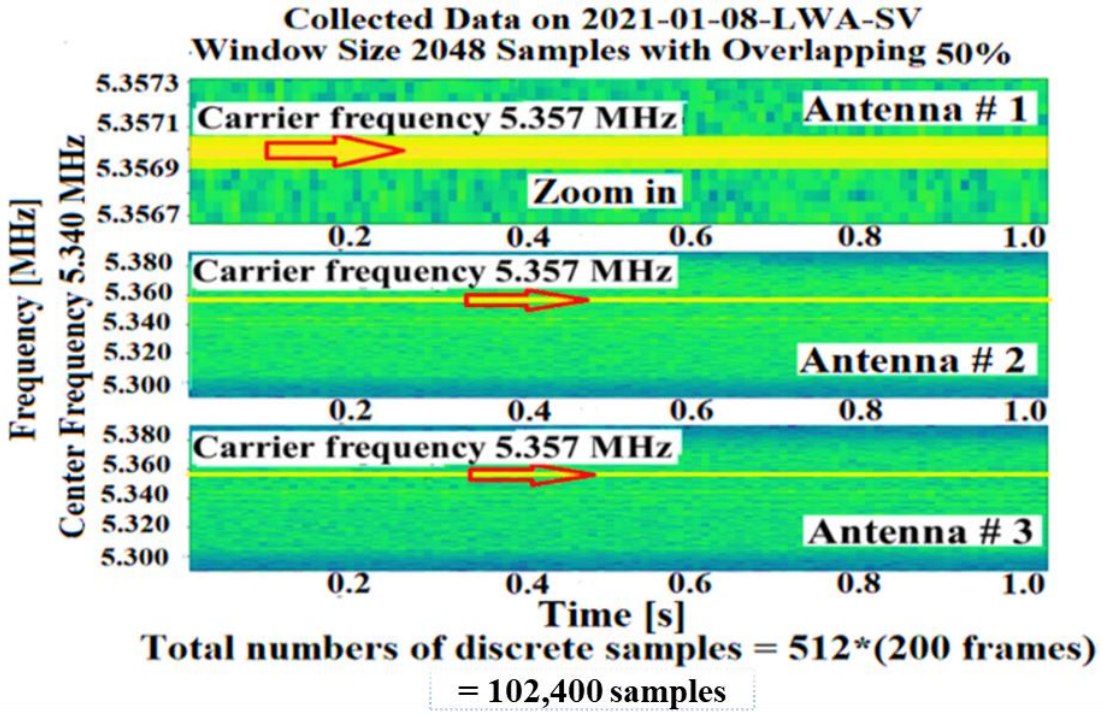

Figure 4.5 A waterfall plot of LWA-SV antenna representing a carrier wave across a frequency range. The color indicates its amplitude demonstrated over time and zooms in for antenna one.

4.3.1.1 Carrier Frequency

The carrier frequency (5.357 MHz) worked only as a carrier wave to carry wave information of waves existing in/on the ionosphere to the antenna array. The carrier radio wave propagated through the atmosphere and reflected off the ionization layers. The receiving antennas received the reflected waves at different paths depending on the antenna position. The hardware method used a quadrature to measure the phase of the emitted and received waves to determine their phase

difference. The difference in phase of the transmitted and received radio waves was a measure of the phase shift.

4.3.1.2 Relative Unwrapped Phase

The time difference image was unwrapped, and its relative phase values were determined by taking an antenna close to the center of the LWA-1 and LWA-SV arrays. The relative phase image removed the absolute phase shift that resulted from the tilted carrier wave. Figures 6 and 7 show examples of relative unwrapped phase images taken from LWA-1 and LWA-SV during three seconds of collection time. Antenna number 10 is used as a reference for LWA-1 in Figure 4.6. Antenna number 134 is used as a reference for LWA-SV in Figure 4.7.

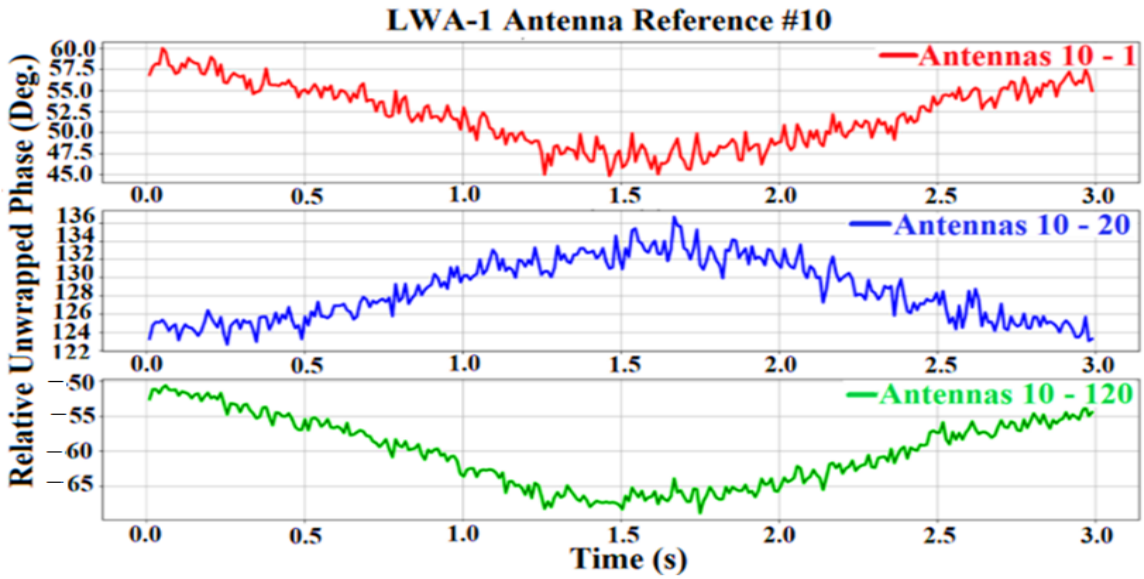

Figure 4.6 The plot displays an example of the relative unwrapped phases versus time in 3 s for LWA−1.

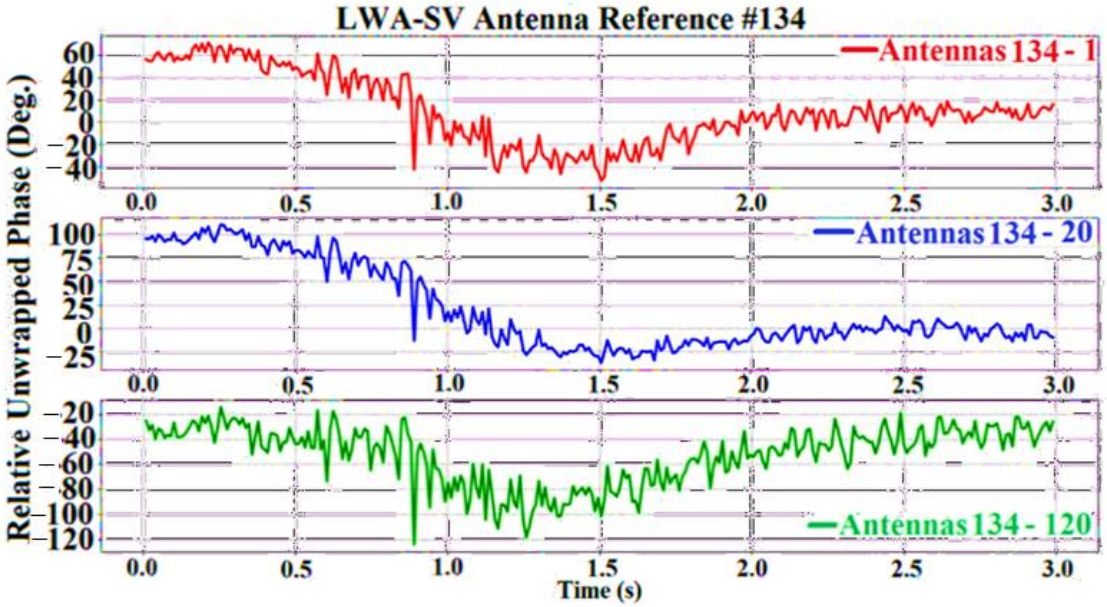

Figure 4.7 The graphic shows an example of relative unwrapped phases vs. time in 3 s for LWA-SV.

4.3.1.3 Spatial Phase Image

The area of antenna locations in the x-direction and y-direction represents phase image using a relative unwrapped phase, as shown in Figure 4.8. The color of the phase image represents the size of the phase shift using unwrapped angles. The positive side illustrates the top of the wave, whereas the negative side shows the bottom side of the wave. The height of a wave represents the amplitude that could be positive or negative. The imaging processing of the relative unwrapped phase was done using a mesh used on the antenna positions and divided into several rectangular shapes. The area ($dx \times dy$) of each cell was around 6 m^2, as depicted in Figure 4.9. Each stand had only one relative unwrapped phase, and the pixels outside the image were zero. The parameters were the center frequency 5.334999 MHz and carrier bin 5.351500 MHz with a sample rate of 100 kHz. The relative unwrapped phases were calculated by taking the stand number 134 of LWA-SV and 10 of LWA-1 as a reference, which was located close to the center of the antenna locations. Polarization zero was chosen as cross-polarizations were provided in the dataset.

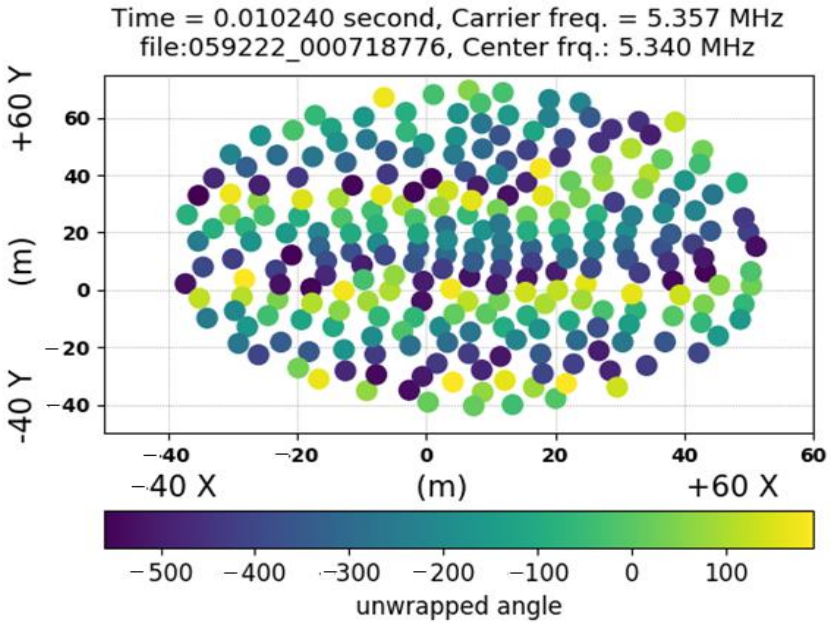

Figure 4.8 Phase image of antenna locations applying the relative unwrapped phase.

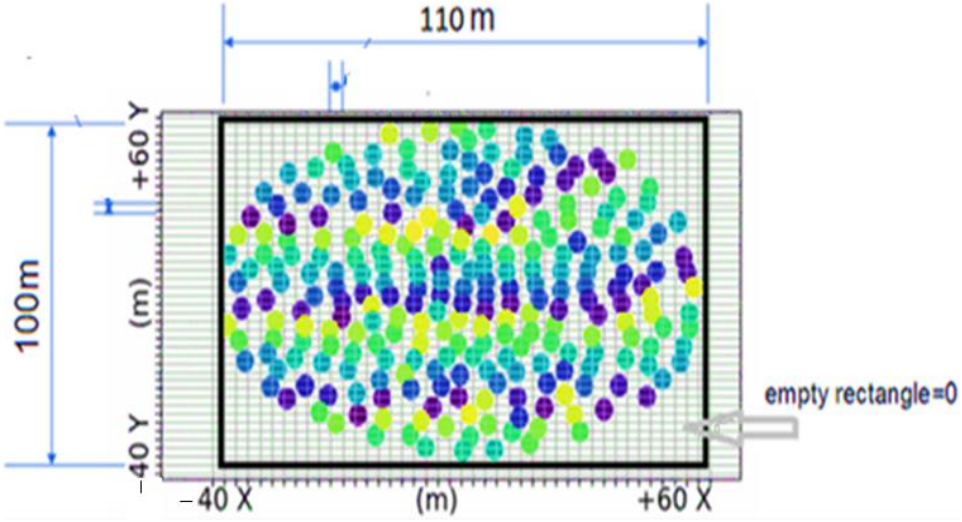

Figure 4.9 Phase image of antenna locations divided into many cells that contain the relative unwrapped phase and the applied Fourier space method mesh.

A 2D Fourier transformed over the space domain was applied to the relative phase image, $f(x,y)$, to obtain a complex Fourier image, $F(u,v)$ in the spatial frequency domain for each time of data collection,

$$F(u,v) = \int_{-\infty}^{\infty}\int_{-\infty}^{\infty} f(x,y)e^{-j2\pi(ux,vy)}\,dxdy \qquad (4.2)$$

Where u and v are the spatial frequencies,

$$F(u,v) = F_{Re}(u,v) + jF_{Im}(u,v) \quad (4.3)$$

$$|F(u,v)| = \sqrt{F_{Re}^2}(u,v) + F_{Im}^2(u,v),) \quad (4.4)$$

$$\phi(u,v) = \tan^{-1}\left|\frac{F_{Im}(u,v)}{F_{Re}(u,v)}\right| \quad (4.5)$$

And where $|F(u,v)|$ and $\phi(u,v)$ are the amplitude and phase distributions of the spatial spectrum given by $F(u,v)$. A 2D Fourier image depicted this symmetry criterion graphically as a succession of symmetric points in the *u* and *v* plane, as shown in Figure 4.10.

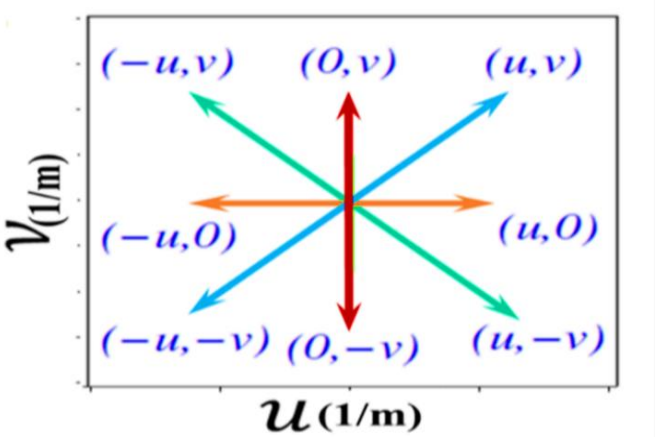

Figure 4.10 Fourier image showing symmetry in two dimensions.

4.3.2 Analysis

The datasets were collected using two locations of receiving antenna array on 8 January 2021. The first frame of LWA-SV started recording at 20:29:20, whereas the first frame of LWA-1 was at 18:00:00. Both datasets lasted around 28 min.

4.3.2.1 Analysis of LWA-SV Spatial Frequency Result

The 2D Fourier image showed many frequency peaks or approximately 170 peaks, as shown in Figure 11a,c. Each peak represented a set of waves on the ionosphere with its own amplitude, frequency, and wave vector. One pair of peaks located close to the origin had a frequency of 0.06 cycles/m and a wavelength of 16.667 m, which was the largest peak and was studied the most for

its possible location of creation. It had a wave vector that sometimes pointed north–south and sometimes slightly tilted from this direction, as shown in Figure 4.11. Different time sequences were tested to check the direction of the wavevectors. As a result, the wavevector maintained pointing around 90% of time in a north-south direction, and 10% of time was tilted in a westward direction.

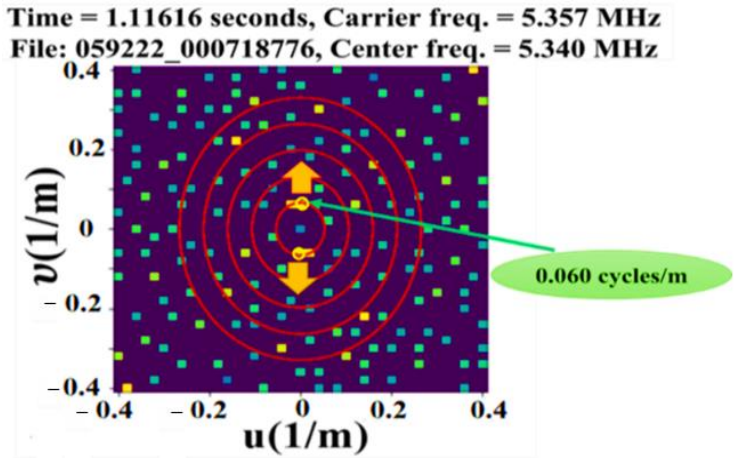

(a)

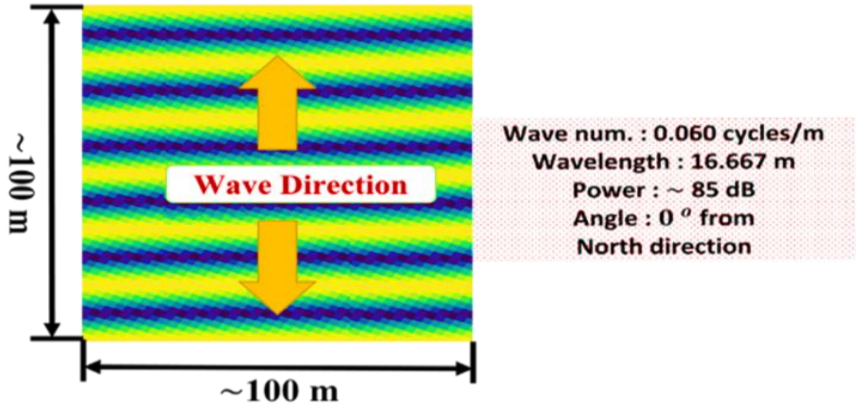

(b)

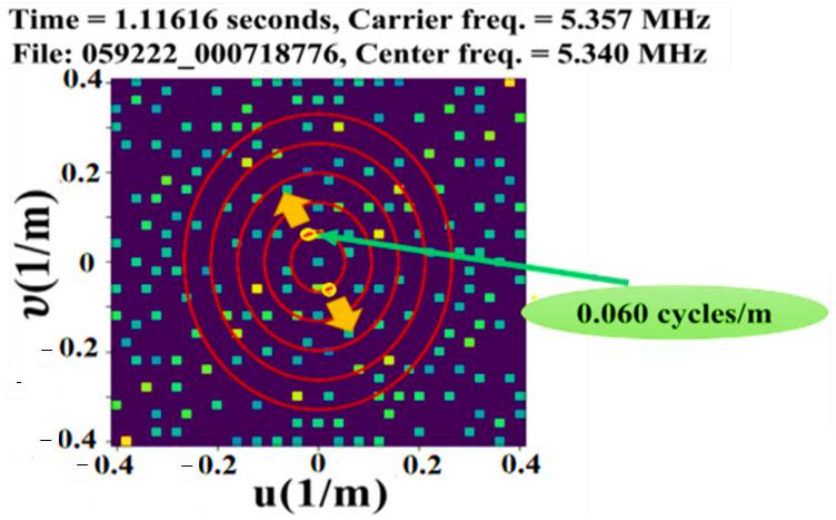

(c)

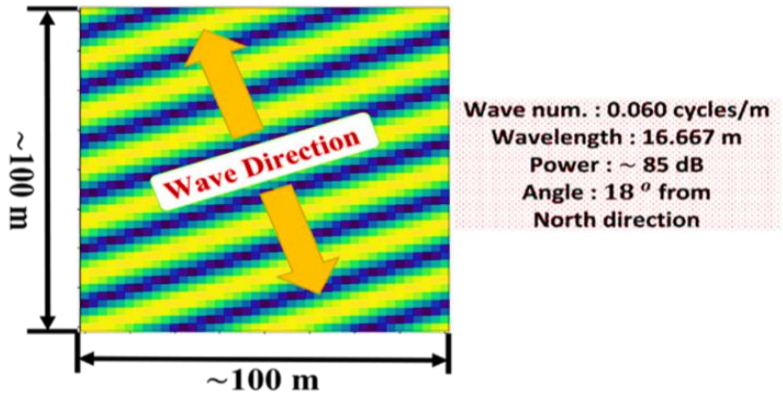

(d)

Figure 4.11 (a) A Fourier image of LWA–SV that shows many peaks which represent sets of detected waves. The the strongest (yellow circle) has 0.06 cycles/m, and the wavevector (yellow arrows) pointing north–south. (b) The inverse Fourier transform (IFT) of (a) revealing the north–south waves. (c) A similar set of waves pointing north–south tilt in a westward direction. (d) The IFT of (c) revealing the tilted waves.

The 2D Fourier images of LWA-SV displayed many spatial frequency peaks (around 170 on one side). The Fourier image shows symmetry sides representing many sets of waves on the ionosphere, as shown in Figure 4.11.

4.3.2.2Analysis of LWA-1 Spatial Frequency Results

A 2D Fourier transform space domain was also applied to a relative phase image for LWA-1 to obtain Fourier images for each time of data collection.

The Fourier image reveals symmetrical sides representing numerous sets of waves on the ionosphere, and the 2D Fourier images of LWA-SV exhibited several spatial frequency peaks of about 170 on one side, Figures 4.12–4.14.

The LWA-1 phase image showed corresponding waves to those seen by LWA-SV. The main Fourier peak was 0.06 cycles/m and was like LWA-SV's but had a northeast–southwest wavevector instead of a north–south one. The 0.06 cycles/m wave was the largest and strongest peak on both sets of data and was studied the most due to its possible location of creation.

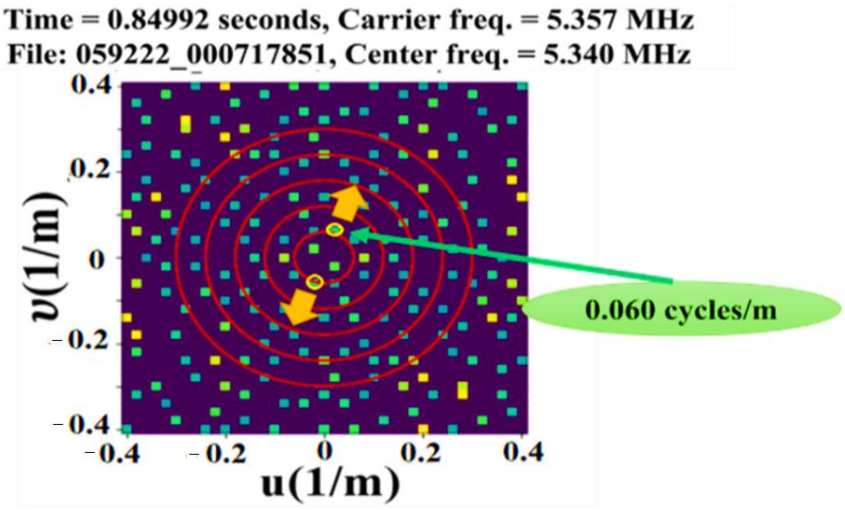

(**a**)

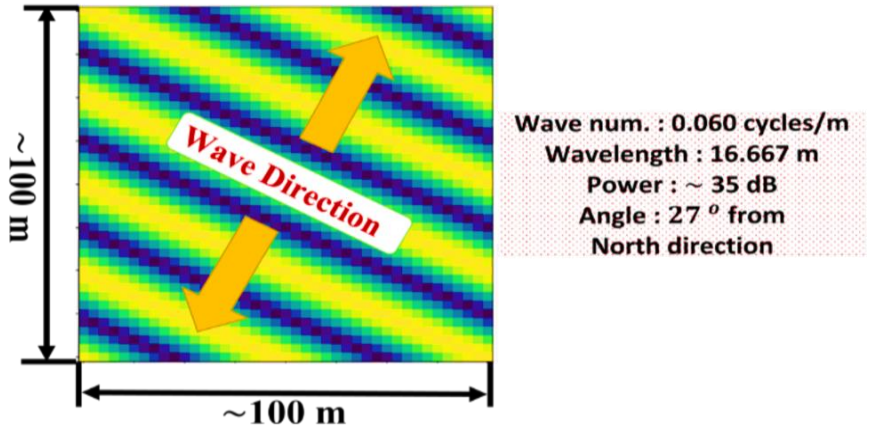

(**b**)

Figure 4.12 A Fourier image demonstrating the wave direction (0.06 cycles/m) (yellow circle) of LWA-1 pointing northeast–southwest with an angle about 30 degrees from the north–south direction. (b) IFT of the spatial frequency with its wave vector.

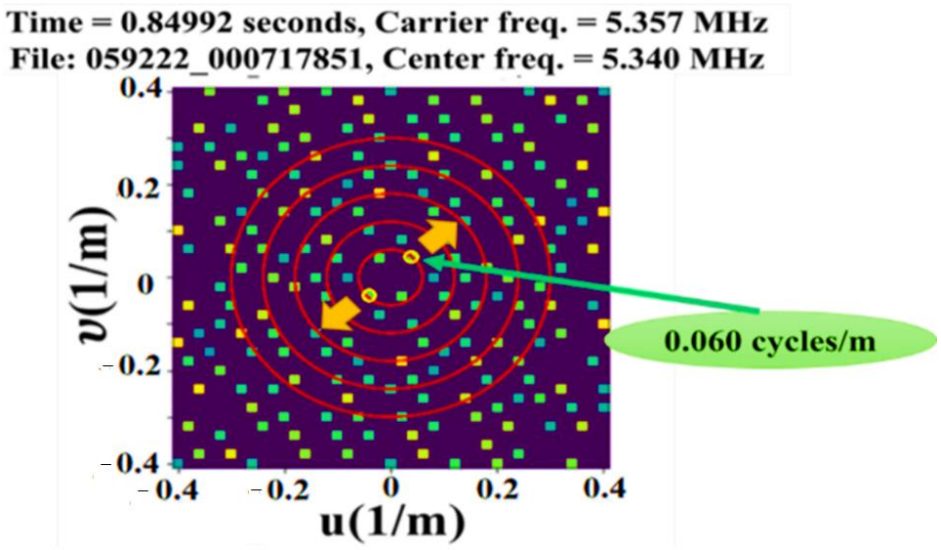

(**a**)

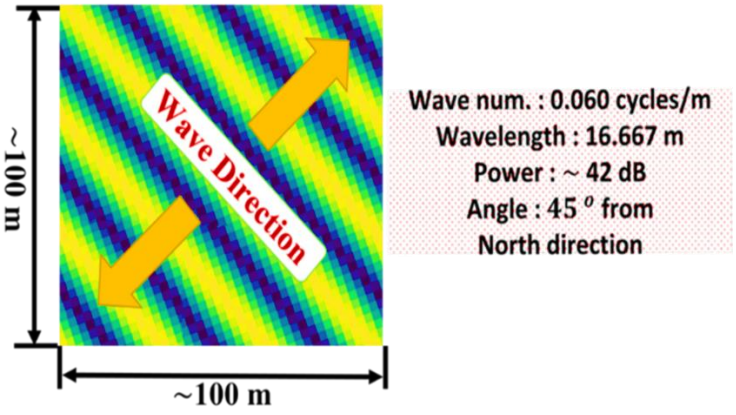

(b)

Figure 4.13 (a) A Fourier image of LWA-1 data with 0.06 cycles/m displaying a northeast–southwest wave vector direction of ~45 degrees eastward from the north–south direction. (b) Its IFT reveals the set of waves and its wave vector.

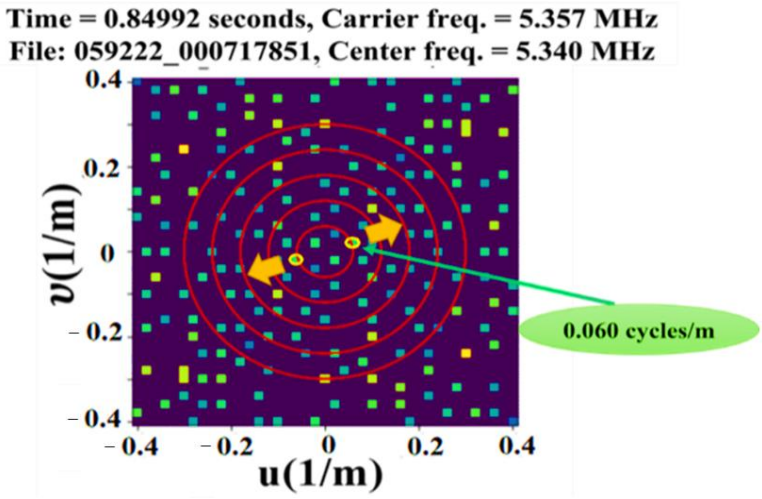

(a)

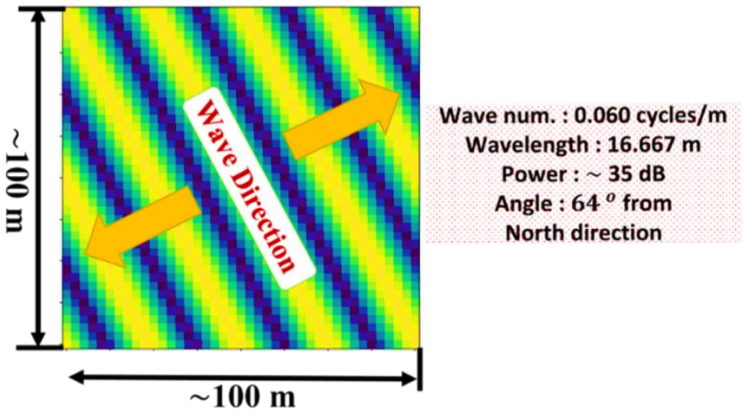

(b)

Figure 4.14 (a) A Fourier image demonstrating the wave direction (0.06 cycles/m) of LWA-1 with angles about 60 degrees eastward (northeast–southwest) from the north–south direction as well as its IFT in (b).

4.3.2.3 Intersection of 0.06 cycle/m Wave Vectors from LWA-SV and LWA-1

There are two places on the surface of the ionosphere reflecting the carrier radio wave. They lie mid-way between Santa Fe and LWA-SV and LWA-1, as shown in Figure 4.15. Each place had its own set of waves. Their Fourier images nicely revealed the intersection points of their wavevectors that represented the location of the source that created the waves. Possible local wave sources were Albuquerque and its nearby power-generating stations. The two sets of data showed a range of vectors in the LWA-1 Fourier image from around 25 to 60 degrees and from around (0 to 13 degrees) in the LWA-SV image. As a result, the intersection points covered a swath of area between Albuquerque and the power stations.

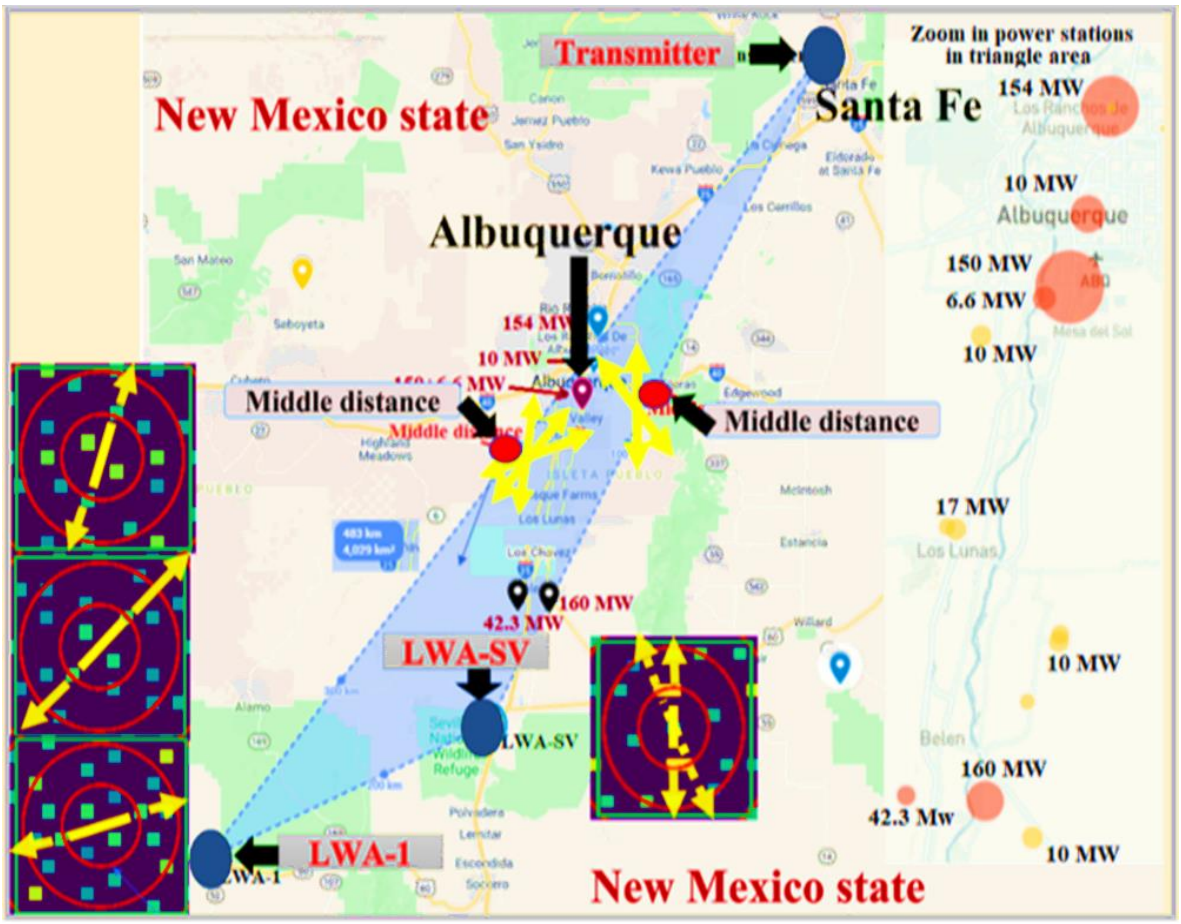

Figure 4.15 Measured wavevectors at mid-way points (red dots) between Santa Fe and LWA-1 and LWA-SV showing their intersections around Albuquerque and local power generating stations.

4.4 Discussion of LWA-SV and LWA-1 Results

The receiving antenna arrays functioned well as cameras where each antenna represented one pixel in the phase image. Hence, the 256 antennas in the array represented 256 pixels in the phase image. The same carrier wave was transmitted; however, there was a short time difference in collecting the raw dataset between the two LWA(s). Their 2D Fourier images showed the same spatial frequency peaks, although not all peaks were similar. The results of the 0.06 cycles/m were the same in terms of their amplitudes, but their wave vectors were different. The wave vectors were different because the direction of the source of the waves was different, i.e., Albuquerque. Albuquerque essentially acted as a point source of disturbance as its waves emanated radially 360

degrees outward. Thus, LWA-1 and LWA-SV saw different wave vectors of the same set of waves. Triangulation using the two sets of wave vectors was used to find the source of the disturbance.

Fourier image analysis showed the presence of ~170 sets of waves that were likely created by both space and Earth disturbing events. There has been some previous research showing a link between man-made Earth disturbing events and ionosphere responses. Such events like these generate waves that have a clear impact on the ionosphere. For example, waves on the ionization layer have been known from ionosondes [2]. This SDR Atmosphere imager has been shown to provide new information, such as the presence of numerous sets of waves with different amplitudes, frequencies, and wave vectors.

Only one set was studied for its possible location of creation, i.e., the strongest peak had a spatial frequency of 0.06 cycles/m with a wavelength of 16.67 m/cycle. The wavevector of this set of waves at LWA-SV and LWA-1 were the same, and both often pointed in the north–south direction and sometimes slightly tilted off this direction. Based on triangulation of the wavevectors, the location of the possible disturbances that created this set of waves was from the local power generating stations and possibly the grid of their transmission lines around Albuquerque, which is considered a main consumer of power. Time measurements over a 1 s and 3 s period of the 0.06 cycles/m peak had a frequency of 30 Hz. A frequency of 30 Hz could have resulted from the resonances of the 60 Hz in-phase current being transmitted within the power grid around Albuquerque. Several power generators supply Albuquerque and are spatially close to each other; therefore, it is possible that their interference can produce the frequency of 30 Hz found in the measurement.

4.5 Conclusions

The SDR Earth Imager enabled imaging of the Earth's ionosphere layer. The wave vector of one set of waves—the strongest with 0.06 cycles/m—was followed in time at both LWA-SV and LWA-1 stations. The most likely sources for this set of waves are the local power generating stations and power usage in Albuquerque, which is a primary consumer of power.

Further investigations are warranted to determine which wave vectors relate to the power of ionospheric waves and local disturbances, such as the power generating stations around Albuquerque.

Chapter 5 Measuring Power of Earth Disturbance Using Radio Wave Phase Imager

This chapter is based on a publication in the Journal of Imaging under manuscript number [11].

[1] Department of Mechanical Engineering, MENG, University of Victoria, Victoria, BC V8W 2Y2, Canada

[2] Centre for Advanced Materials and Related Technology (CAMTEC), Department of Mechanical Engineering, MENG, University of Victoria, Victoria, BC V8W 2Y2, Canada; rherring@uvic.ca

***** Correspondence: rsharif@uvic.ca or rudwan_naj@yahoo.com

Abstract

Numerous studies have investigated ionospheric waves, also known as ionospheric disturbances. These disturbances exhibit complex wave patterns similar to those produced by solar, geomagnetic, and meteorological disturbances and human activities within the Earth's atmosphere. The radio wave phase imager described herein measures the power of the ionospheric waves using their phase shift seen in phase images produced by the Long Wavelength Array (LWA) at the New Mexico Observatory, a high-resolution radio camera. Software-defined radio (SDR) was used for processing the data to produce an amplitude image and phase image. The phase image revealed the ionospheric waves, whereas the amplitude image could not see them. From the phase image produced from the carrier wave received at the LWA, the properties of the ionospheric waves have been previously characterized in terms of their energy and wave vector. In this study, their power was measured directly from the phase shift of the strongest set of ionospheric waves. The power of these waves, which originated at Albuquerque, the local major power consumer, was 15.3 W, producing a power density of 0.018 W/m2. The calculated power density that should be generated from the local power generating stations around Albuquerque was also 0.018 W/m2, in agreement with the experimen-tally measured value. This correspondence shows that the power generated by power stations and being consumed is not lost but captured by the ionosphere.

Keywords: software-defined radio; radio wave imager; ionospheric waves; phase imaging method with wavevectors; power stations; transmission line losses.

5.1 Introduction– Earth's Ionosphere Response to Waves

Changes in the ionosphere, the uppermost part of the Earth's atmosphere, are known as ionospheric disturbances. These disturbances, often referred to as ionospheric waves, can be triggered by a diverse range of natural phenomena, including solar flares, geomagnetic storms, meteor impacts, lightning, volcanic eruptions, and earthquakes, as well as man-made disturbances, such as explosions and electricity generated and transported of power stations [3], [99], [100], [101]. Traveling ionospheric disturbances (TIDs) are generated by atmospheric waves that travel across the ionosphere region. Scientists have employed various techniques to identify and analyze these disturbances to better comprehend the mechanics of wave propagation and the geophysical causes of TIDs. Therefore, TIDs have been detected for years using ground-based observations, namely, radio techniques, such as ionosondes, incoherent scatter radars, and High-Frequency (HF) Doppler sounders [102], [103], [104], [105], [106]. More recently, GPS total electron content (TEC) has been used to create 2D images of TIDs in places like Japan [107],[108] and the United States [109]. Understanding TIDs is critical to improving our ability to anticipate and mitigate their impact on our technology and environment.

TIDs are disruptions in the number of electrons in the ionosphere caused by a disturbance in atmospheric gravity waves (AGWs). These waves collide with neutral particles traveling through the thermosphere and ionosphere. The resulting movement of the neutral gas sets the ionosphere in motion, causing variations in electron density.

The characteristics of TIDs are influenced by factors such as their origin, the conditions of their spread, damping, and the extent to which they are reduced over time. Therefore, predicting TID periods, amplitudes, speeds, and directions at a given location remains challenging because of the complex nature of TIDs and the lack of comprehensive observational data [110].

Several articles have mentioned techniques for identifying traveling ionospheric TIDs [1], [9], [111], [112], [113]; still, additional observations are needed to fully understand the physics of wave propagation and geophysical source phenomenology. However, in more detail, these articles study physical events, such as the tsunami associated with the Tohoku earthquake that occurred on 11 March 2011, which was examined using data on total electron content (TEC) from around 4000 GPS devices dispersed across the continental United States. This work proved that the accompanying TIDs were detected during the tsunami, which traveled across the Pacific Ocean to Japan's west coast for several hours. The researchers computed different TID properties,

including horizontal wavelength, velocity, and duration. A two-dimensional representation of TEC disturbances was made possible using this network of GPS receivers [114].

The characteristics and behavior of ionospheric waves have been the subject of research. For instance, Hunsucker and Hargreaves thoroughly explain ionospheric waves, including how they are created, spread, and affect the ionosphere. They reviewed several ionospheric wave types, such as gravity, acoustic, and plasma waves, and explained how they interact with the ionosphere [115].

AGWs are atmospheric waves that occur when air density and pressure are disturbed by wind, heat, or terrain. When gravity restores equilibrium, the waves propagate to bring the atmosphere back to balance after it has been disrupted by the external force. These waves, generally described as buoyancy waves, may significantly alter the weather and environment [116], [117], [118].

Other natural disasters, including earthquakes, have generated waves affecting the ionosphere. In 2016, the authors of [47] conducted a study on the Nepal earthquake of 25 April 2015, using GPS technology to measure changes in the ionosphere. They found that the earthquake caused seismic-traveling ionospheric disturbances (STIDs) propagating at 2.4 km/s horizontally.

Another study by Harrison observed a correlation between the responses of the lower ionosphere and seismic activity in the region prior to an earthquake [43].

The generation of waves on the ionosphere and magnetosphere by power line emission (PLE) and power line harmonic radiation (PLHR) is a subject of growing concern due to their potentially harmful effects [9], [54], [62], [63], [64], [65].

In more recent experimental investigations, ionosphere wave sources have been traced back to the vicinity of local power generating stations [10]. The primary site of power consumption was identified as Albuquerque, New Mexico. The success of this endeavor could be attributed to the novel measurement technique employed, which used a wavevector analysis of the ionosphere waves detected at two distinct locations, LWA1 and LWA-SV.

The study reported here introduces a novel approach for measuring the power of waves in the ionosphere and investigates their frequency characteristics, representing the first instance of such measurements. This report involves using a terrestrial radio-wave transmitter to illuminate the ionosphere and measure the power of its ionospheric waves. The radio waves were transmitted from the ground and reflected back to a two-dimensional array of passive receivers/antennas, allowing for the relative phase imaging of the ionosphere waves and revealing their temporal and spatial evolution. This study used Fourier analysis to determine the power, energy, and location of

the ionosphere wave generation based on amplitude, frequency, and wavevectors. Furthermore, this study explored the possibility of a correlation between ionosphere waves and local Earth disturbances, such as power generating stations.

5.1.1 Response of the Ionospheric System to Man-Made Disturbances

The impact of power line emission (PLE) and power line harmonic radiation (PLHR) on the ionosphere and magnetosphere have been a growing concern. Since the 1970s, many publications have reported on PLHR and PLE monitoring on the ionosphere PLHR is a type of electromagnetic wave at harmonic frequencies of 50 or 60 Hz, observed in the ionosphere (radiated) and caused by electric power systems on Earth's surface. PLE refers to a form of emission that occurs at frequencies of 50 or 60 Hz. Because their frequencies are in good accord with comparable ground power system frequencies, PLHR and PLE are thought to be connected to ground electric power systems [10, 11]. Other investigations have shown that increased electron precipitation and changes in the ionosphere and magnetospheric currents may result from the penetration of PLHR into the lower ionosphere, potentially impacting thunderstorm activity [62], [63], [64], [65]. Some of the artificial disturbances in the ionosphere were PLE and PLHR. These articles considered PLHR as a type of pollution originating from the power system [119], [120]. In 1975, The pioneering work of [121], [122] revealed that very low–frequency (VLF) line radiation existing in the Earth's magnetosphere has a frequency close to 60 Hz. It was proposed that harmonic radiation from the Canadian power grid penetrates a whistler duct in the magnetosphere. Luette et al. in 1977 showed that PLHR had the ability to stimulate the strongest waves on the magnetosphere [123]. In 1979, Park and Miller studied magnetospheric wave intensity between 2 to 4 kHz [124]. They identified that the chorus (discrete narrowband emissions) activity indicated a noticeable minimum on Sundays compared to the rest of the week because of low electrical power usage. Other researchers, specifically Matthews and Yearby in 1981 [122], found that the characteristics of VLF line radiation of magnetospheric waves detected at one location, Halley (75.5674° S, 25.5165° W) British Overseas Territory), were usually equivalent to the PLHR observed at another location, Siple (75.916667° S, 83.916667° W). The analysis of these events employing the time–frequency spectrogram of the electric field strength revealed numerous parallel horizontal spectral

lines separated by 50 Hz/100 Hz or 60 Hz/120 Hz, equivalent to the local terrestrial power system's working frequency. Another study [70] showed that broadcast transmitters, electric power plants, and their associated power line transmission losses, as well as electric power losses in heavy industries, are all potential sources of ionosphere disturbances that may generate ionosphere waves.

In other research, the characteristics and connections between the two types of radiation were investigated using DEMETER satellite data to identify PLHR and PLE events in the ionosphere above China [54]. The electric field power density time–frequency spectrograms displaced 128PLHR events with the 50 Hz spectral line frequency. They were very closely connected to the frequency of the ground power grid [54].

More recent experiments found the sources of the ionosphere waves to be local power generating stations, and the primary place of power consumption was Albuquerque, NM. This capability was enabled by the measurement of the wavevectors of the ionosphere waves made possible by the detection of the waves from two locations, LWA1 and LWA-SV [10].

The study reported here involves illuminating the ionosphere with radio waves from a terrestrial radio-wave transmitter and builds upon the previously reported capability of using this device to measure the ionosphere waves' wavevectors. The radio waves terrestrially transmitted were reflected back from the ionosphere to the ground and were captured by a two-dimensional array of passive receivers/antennae. From the time-tagged received signals at each receiver, the ionosphere waves could be relative phase imaged, revealing their spatial and temporal evolution. From a Fourier analysis of the ionosphere waves' phase image, which contained sets of phase shifts, frequencies, and wavevectors, properties of the strongest set of waves, such as the power, energy, and location of generation of the ionosphere waves, were determined. A possible relationship between the waves of the ionization layer and man-made local Earth disturbances, namely local power generating stations, is suggested by matching the measured power to the calculated power.

5.2 Materials and Methods

5.2.1 SDR Experimental Method

Through the transmission of radio signals almost vertically from the Earth's surface, the SDR Earth Imager effectively acquires significant data from the ionosphere. Following their interaction with the ionosphere, these signals make their way back to the Earth's surface. Throughout this involved procedure, the antenna array camera diligently captures and records these signals, enabling the creation of amplitude and phase imager. Of particular interest, the phase imagery reveals the presence of a phase shift, represented as $\Delta\varphi$, which indicates the variation in the path length (L) that the radio wave has traversed.

$$\Delta\varphi = 2\pi\ (\Delta L/\lambda) = 2\pi\ f\ (\Delta L/c) \quad (5.1)$$

where c represents the speed of light, λ denotes the wavelength, and the f represents the frequency of the carrier wave. The phase shift indicates the disparity in the path length covered by the radio wave traveling from the transmitter to the antenna array detector. This phase shift holds significance as it aids in assessing the strength or power of the ionospheric wave.

Data were collected at two distinct locations in New Mexico, LWA-1 and LWA-SV. One dataset was collected at the Long Wavelength Array (LWA)-SV station at the Sevilleta National Wildlife Refuge in central New Mexico [72]. The other set of data was obtained using the LWA-1 radio telescope array, which is positioned in northern New Mexico and has a diameter of 100 m. This radio telescope array is associated with the University Radio Observatory [95].

5.2.1.1 Transmitter and Dataset Collection

The The transmitter was placed in Santa Fe and transmitted radio waves with frequencies of 5.3570 MHz on 8 January 2021, as shown in Table 1.

Table 5.1 Transmitter signal and data set specifications were used during the LWA experiment.

Santa Fe Transmitter (35.71144° N, 106.0084° W)	
Date and Time	UT 8 January 2021, 20:29:30
Transmitted Frequency	5.3570 MHz
Mode -Send	CW Tone (Continuous Wave)
Receiver LWA-SV (34.348° N, 106.886° W)	
Center Frequency	5.33999 MHz
Polarization	Zero
Date and Time of First Frame	8 January 2021, 20:29:20
Sample Rate	100,000 Hz

Recorded Time	1765.895 s
Receiver LWA-1 (34.069° N, 107.628° W)	
Center Frequency	5.33999 MHz
Polarization	Zero
Date and Time of First Frame	8 January 2021, 18:00:00
Sample Rate:	100,000 Hz
Recorded Time	1731.281 s

5.2.1.2 Receivers and Transmitter Distances

The LWA-SV and the Santa Fe transmitter are separated by around 171 and 235 km, respectively, from the LWA-1 station. Figure 1 visually represents the approximate 75 km between the two stations, LWA1 and LWA-SV [95].

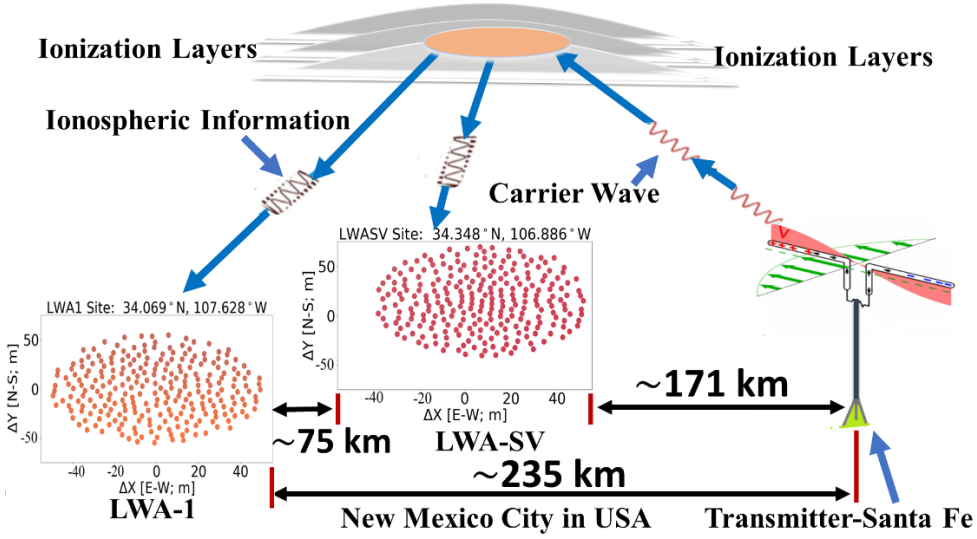

Figure 5.1 The distance between the transmitter of the carrier wave in Santa Fe and the two receiver arrays at the LWA stations, LWA1 and LWA-SV, as well as the distance between the two stations.

5.2.1.3 LWA-1 and LWA-SV Experimental Approach

The LWA Software Library (LSL) was built to manage the LWA-1 and LWA-SV data formats and make them accessible to basic analytic tools [98]. The carrier wave was extracted from the frequency range employing a short-time Fourier transform (STFT). For the LWA-SV and LWA-1 data, the relative unwrapped phase difference of the antenna reference of this channel was computed.

5.2.2 Amplitude and Phase Images from Antenna Array Receiver

An amplitude image produced from the carrier radio wave does not display any wave information, as shown in Figures 2–4. The plot in Figure 2 shows the absolute values of real numbers and the amplitude image obtained from performing spectrogram analysis on the raw antenna data. Specifically, the plot is based on selecting the transmitted carrier bin from 256 antennas.

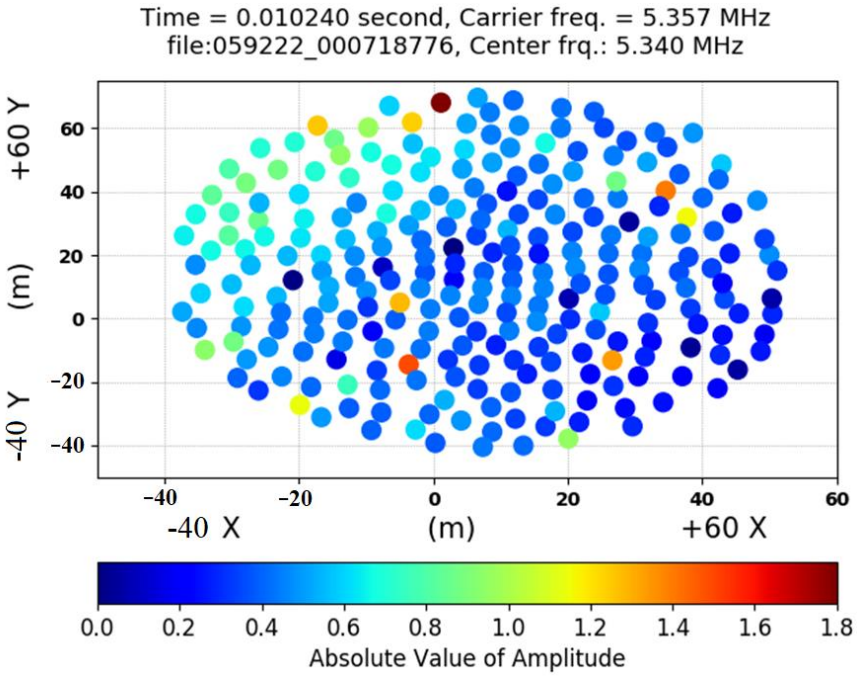

Figure 5.2 An amplitude image produced from the amplitude signals received at each antenna location.

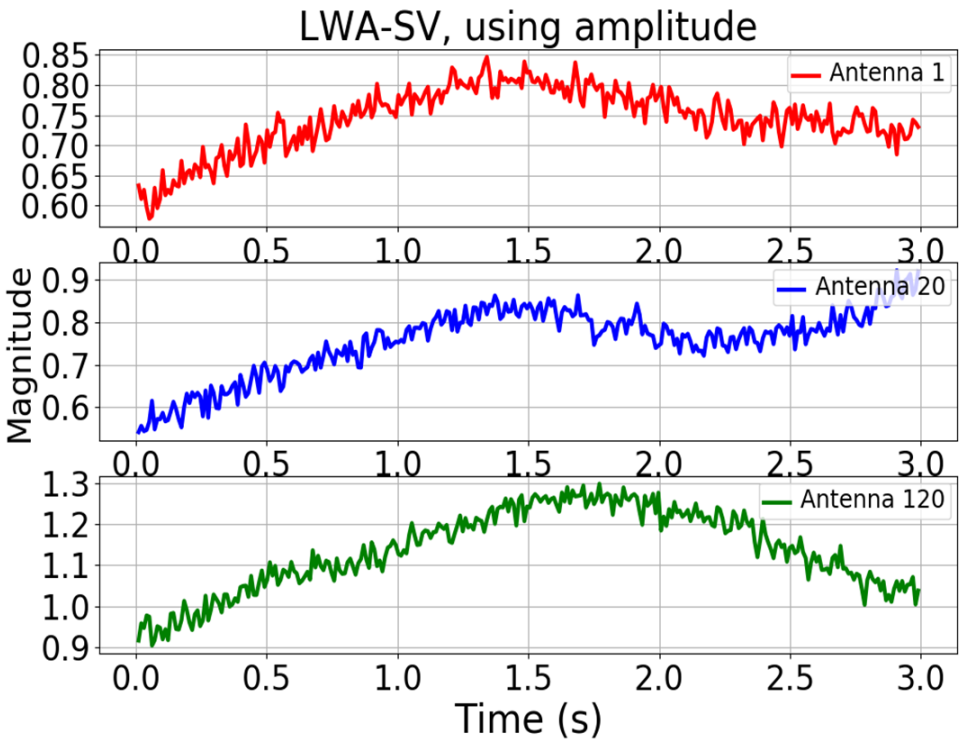

Figure 5.3 Three plots displaying the amplitude signals received versus time over a 3 s period at three antennas, respectively.

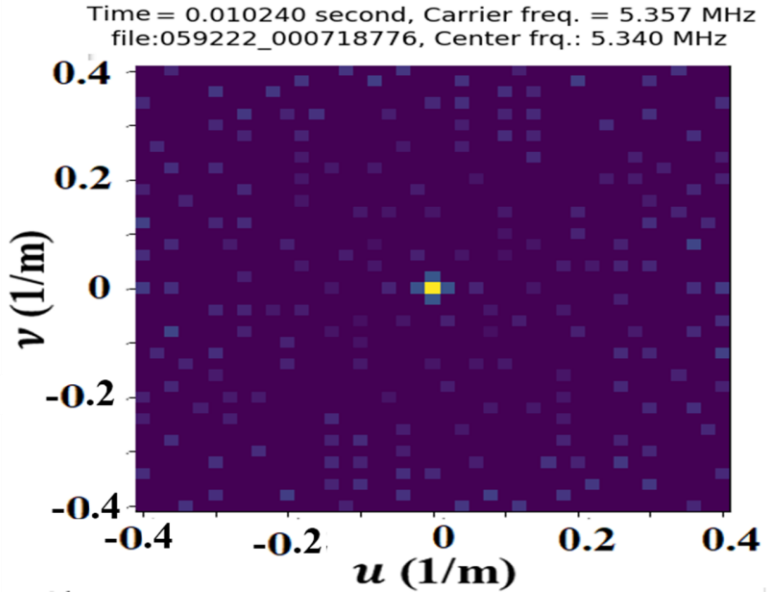

Figure 5.4 The Fourier image of the amplitude image in Figure 2, which does not reveal any strong set of waves.

The phase difference between the signals received at each individual antenna in the array is the phase shift. Since each antenna contributes one phase measurement, the antenna array works as a camera to

produce a phase image, which reveals the waves within the ionosphere. The phase shift is directly proportional to the amplitude of the ionospheric waves.

5.2.3 Spatial Phase Image

The antenna placements in the x- and y-directions are depicted in Figure 5. By using unwrapped angles, the figure uses color to show the size of the periodic phase shifts. The wave's peak is illustrated on the positive side, while the bottom is depicted on the negative side. The size of the phase measures the amplitude of a wave in meters. The relative unwrapped phase image is distributed on a mesh based on antenna placements and split into a variety of rectangular forms. Each has a surface area of roughly 6 m^2 (dx×dy), as shown in Figure 5.

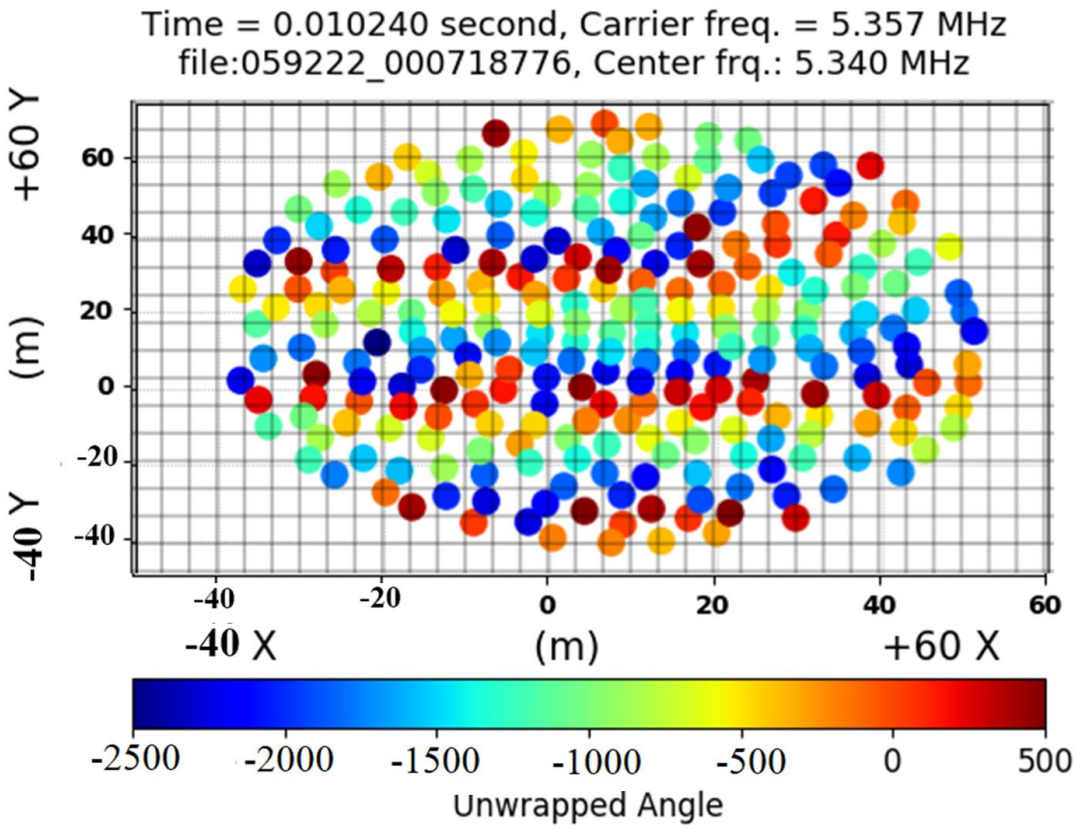

Figure 5.5 The grid showing antenna locations is divided into cells containing relative unwrapped phases to yield the phase image. A dominant vertically oriented wave is obvious.

The center frequency of 5.334999 MHz, the carrier bin of 5.351500 MHz, and a sampling rate of 100 kHz were the parameters of the dataset. The relative unwrapped phases were determined

using LWA-stand SV's number (antenna) 134 and LWA-1's stand number (antenna) 10, both near the center of the antenna sites. The sample included cross-polarizations. A polarization of zero was used in the generation of the phase image.

For each time of data collection, a 2D Fourier transform over the space domain was performed to the relative phase image, f(x, y), to produce a complex Fourier image, F(u, υ), in the spatial frequency domain.

For each time of data collection, a 2D Fourier transform over the space domain was performed to the relative phase image, f(x, y), to produce a complex Fourier image, F(u, υ), in the spatial frequency domain.

$$F(u,\upsilon) = \int_{-\infty}^{\infty}\int_{-\infty}^{\infty} f(x,y)e^{-j2\pi(ux,\upsilon y)}\,dxdy \quad (5.1)$$

Where u and υ are spatial frequencies

$$F(u,\upsilon) = F_{Re}(u,\upsilon) + jF_{Im}(u,\upsilon), \quad (5.2)$$

The Fourier image's amplitude is determined by

$$|F(u,\upsilon)| = \sqrt{F_{Re}^2(u,\upsilon) + jF_{Im}^2((u,\upsilon)}, \quad (5.3)$$

The Fourier image's phase angle is calculated as

$$\phi(u,\upsilon) = tan^{-1}\left|\frac{F_{Im}(u,\upsilon)}{F_{Re}(u,\upsilon)}\right|, \quad (5.4)$$

The power of the wave is given by the amplitude square as

$$P(u,\upsilon) = |F(u,\upsilon)|^2, \quad (5.7)$$

The Fourier transform that produces the Fourier image from the phase image provides a convenient and effective method of separating the different sets of waves by their wavevectors and frequencies. The amplitudes of the Fourier peaks are the sizes of the phase shifts within the phase

image. A representative Fourier image is shown in Figure 6, where each peak is paired with another peak of opposite wavevector and frequency symmetrically placed about the u and v's origin (0, 0).

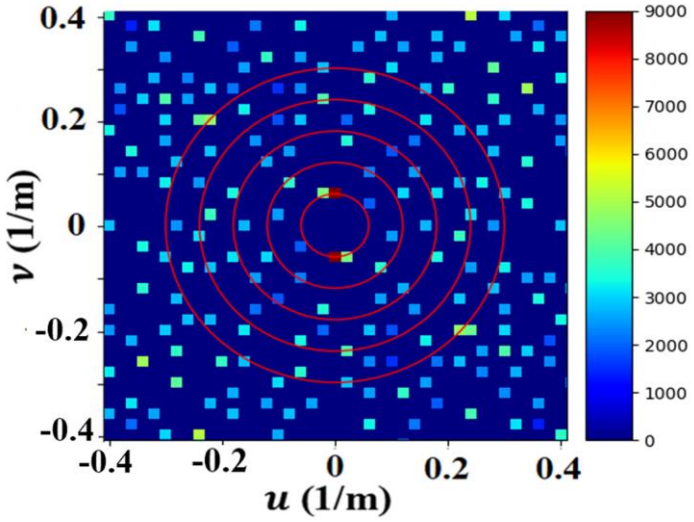

Figure 5.6 Fourier image shows symmetry in two dimensions, revealing many sets of waves existing in the phase image. The red circles in the plot show the frequency (0.06 cycles/m) in a series of harmonics.

5.3 Results

5.3.1 Analysis of LWA–SV and LWA-1 and Spatial Frequency

The experiment was conducted on 8 January 2021 at 20:30 UTC at the Santa Fe transmitter location (35.71144° N, 106.0084° W). The transmitted frequency was 5.3570 MHz, and the mode used was CW tone (continuous wave).

The experiment involved two receivers: LWA-SV (located at 34.348° N, 106.886° W) and LWA-1 (located at 34.069° N, 107.628° W). For the LWA-SV receiver, the date and time of the first frame recorded were 8 January 2021 and 20:29:20 UTC. The sample rate was 100,000 Hz, and the total recorded time was 1765.895 s. For the LWA-1 receiver, the date and time of the first frame recorded were 8 January 2021 and 18:00:00 UTC. The sample rate was also 100,000 Hz, and the total recorded time was 1731.281 s.

There were two places on the ionosphere being measured (Figure 1). They lay mid-way between Santa Fe and LWA-SV and between Santa Fe and LWA-1. Each place measured its own set of waves. Together, their stereographic projection revealed nicely the intersection points of the two sets of wavevectors having the same frequency of 0.06 cycles/m but different wavevectors [10].

Their intersection point represents the location of the source creating the waves as the ionospheric waves radiate outwards 360 degrees from the source. The local wave sources were previously determined to be Albuquerque and its nearby power generating stations [10].

Figure 7 shows a Fourier image of the LWA-SV data revealing ~177 spatial frequency peaks. A set of strong peaks near the origin with a frequency of 0.06 cycles/m and wavelength of 16.667 m was selected to determine its power, represented by the two symmetric, yellow peaks in Figure 7.

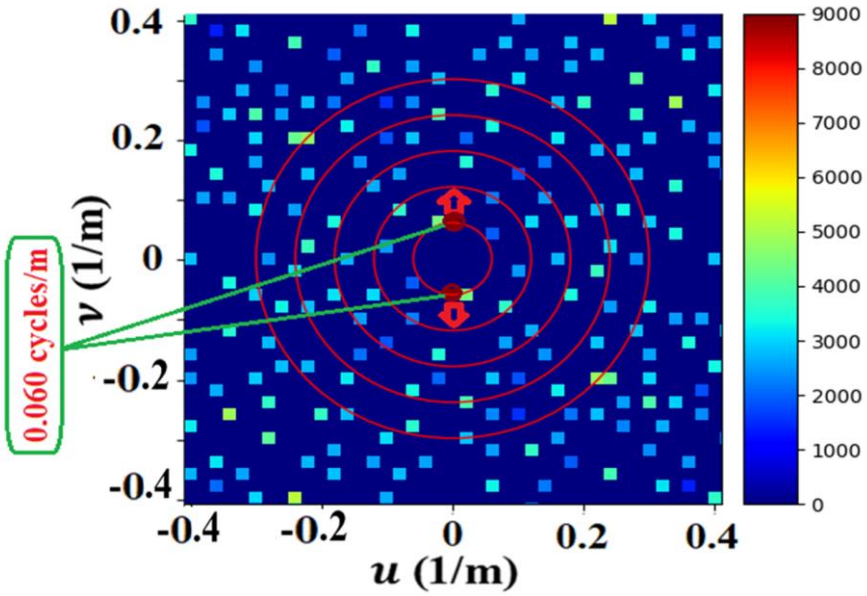

Figure 5.7 Fourier image of LWA-SV showing many peaks representing many sets of waves. The strongest set (red peaks) has 0.06 cycles/m with its wavevector (red arrows) pointing north–south. Greenish peaks have low power intensity, as shown in the scale bar. The red circles in the plot show the frequency (0.06 cycles/m) in a series of harmonics.

5.3.2 Model to Determine Wave Power

The power of the waves on the surface of the ionization layer was determined using a simple capacitor model. The analysis focused on the strongest set of waves, those represented by the two yellow Fourier peaks in Figure 7. These peaks were previously used to determine the origin of their disturbance at Albuquerque [10].

The ionosphere model employed two parallel conductive plates to represent both the Earth's surface and the bottom surface of the ionosphere. The change in the distance between the plates, d, due to the amplitude of the waves, is the size of the measured phase shift in Figure 7. The surface area of the plates represents the imaged area of the antennas onto the surface of the ionosphere.

The change in capacitance, ΔC (farads), is given as

$$\Delta \mathbf{C} = \frac{\boldsymbol{K} * \in_{\mathbf{0}} * \boldsymbol{A}}{\Delta \boldsymbol{d}} \tag{5.8}$$

where K is the relative permittivity and equals 1 for vacuum and air; $\in_0$ is the permittivity of free space, $\in_0 = 8.854 \times 10^8$; A is the area illuminated on the ionosphere, $\frac{\pi * (a * b)}{4}$ (m^2), where a and b are the elliptical coordinates (50 m and 55 m, respectively) determined from the size of the antennae array; and Δd is the peak height, i.e., the change in distance between the plates (403 m) and equals the size of the phase shift of the wave. In terms of current and voltage, the change in capacitance is

$$\Delta \mathbf{C} = \frac{\boldsymbol{Q}}{\Delta \boldsymbol{V}} \tag{5.9}$$

where ΔV (volts) is the change in voltage across the capacitor. Q (coulombs) is the electron density in the ionosphere (3.5356×10^{11} $(\text{electrons}/\text{m}^3)$ typically ranging from 10^{10} to 10^{13} electrons/m^3, determined from the critical frequency for reflection/transmission of radio wave propagation within the ionosphere that occurs around 5 MHz, which was the carrier wave frequency used in this study. It should be noted, though, that the various ionosphere layers' altitudes and their electron concentrations change according to the cyclical nature of solar radiation in every geographic area. Three factors taken into account in this study determined the ionosphere's reflection. The first is the layer's ion density. The second is the radio wave's frequency, and the third is the angle at which the wave enters the ionosphere, close to 90 degrees from the vertically propagating wave.

The graph in Figure 8 shows the changes in the average size of the phase shift (degrees) in one second, which fluctuates over time. The size of the phase shift reached a low level of around 8500 degrees and a high level of around 9100 degrees, having an average phase shift of 8707 degrees.

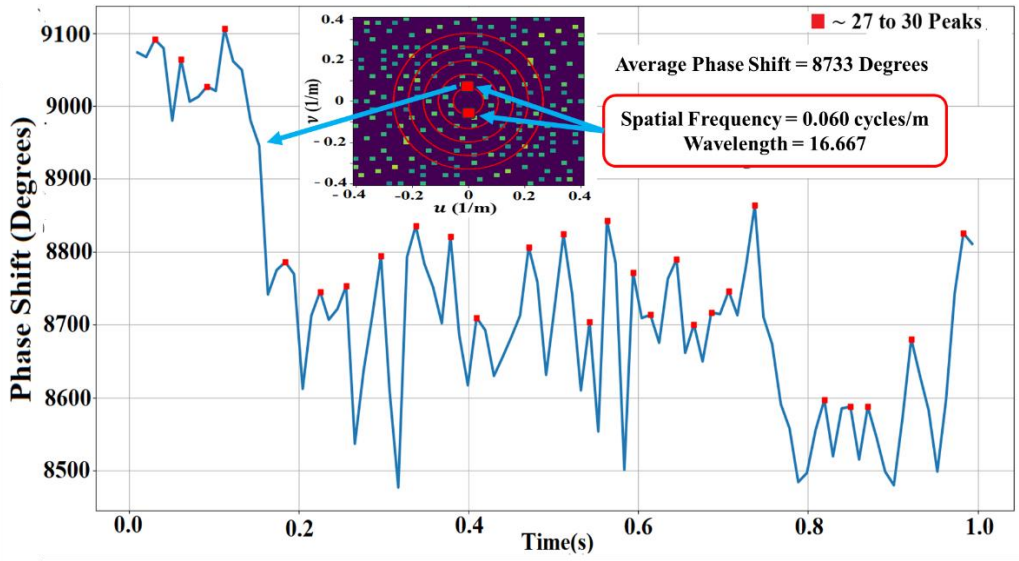

Figure 5.8 Phase shift measurements during one second of collection time having an average shift of 8707 degrees for the set of waves having 0.06 cycles /m.

The change in voltage of the capacitor was determined to be 1192 V. The current of the charge carried by the wave was determined to be 0.02468 A. The power of this set of waves was determined to be 14.7 W. This power increased to 15.3 W when translating it from the patch illuminated on the ionosphere to Albuquerque, a distance of 22 km, the source of the waves. A damping of 0.17/km was applied to the traveling wave determined from the reduction of the power of an ionospheric wave generated from the Nepali earthquake propagating to Taiwan and the Czech Republic [14].

The power density at Albuquerque was determined to be 0.018 W/m^2 from the power, 15.3 W per area, i.e., ($\pi \times \lambda^2$), where λ was taken from the wavelength of the ionospheric wave, i.e., 16.7 m. In a similar manner, the total power density of all the sets of waves revealed in the Fourier image of Figure 7, for which there were 177, resulted in a power density of 0.1 W/m^2 at the translated point of Albuquerque. This result is considered a low approximation since their sources of creation, which could be far and not local, were not determined.

5.3.3 Analysis of LWA-SV Spatial Frequency Results

Many local sources of power from generators within the state of New Mexico produce electromagnetic disturbances from their electric power stations and transmission lines. These disturbances were investigated for their power in context to the analysis of these results.

5.3.3.1 Local Power Generating Stations and Places of Measurements

Figure 9 displays the power generating stations around Albuquerque City and illustrates the expected measurement places between the transmitter in Santa Fe and the antenna arrays (LWA-SV and LWA-1).

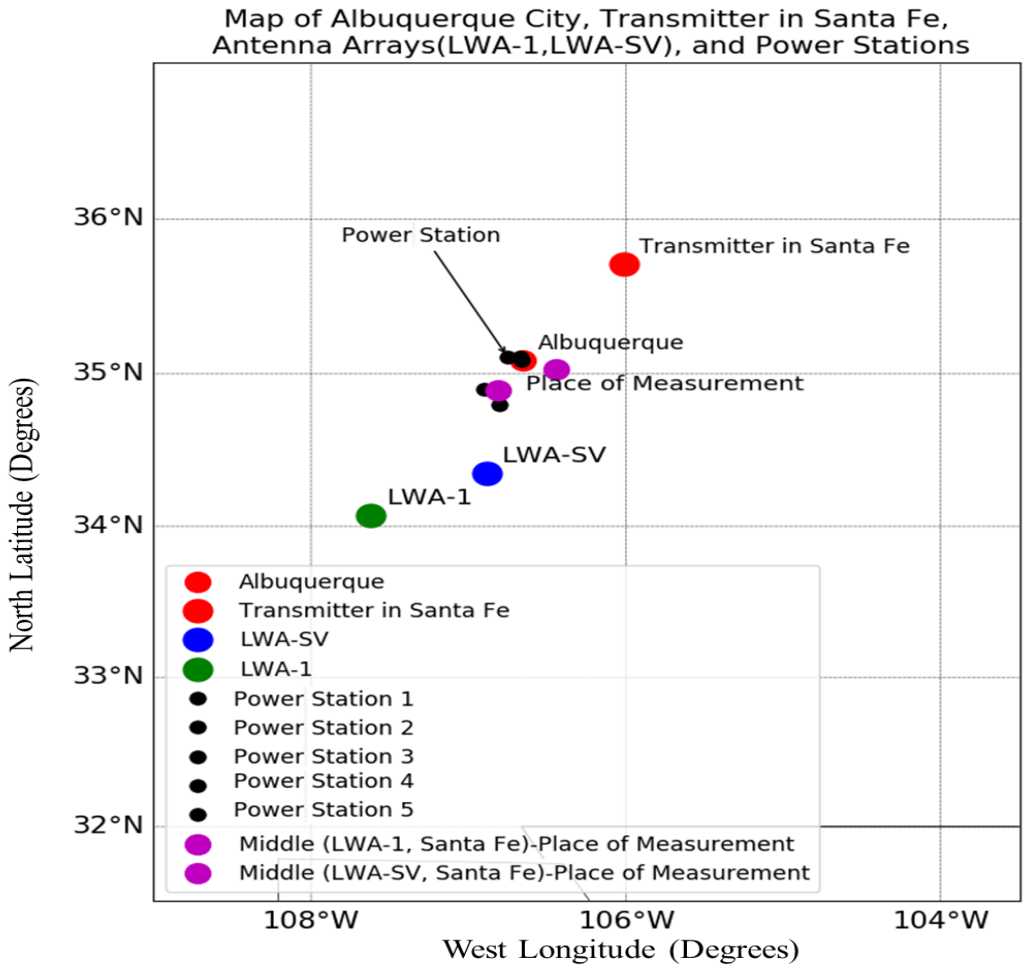

Figure 5.9 Map showing the power generating stations between the transmitter located in Santa Fe and LWA-SV and LWA-1.

The power, *I*, reaching the ionosphere generated by the power consumed from the local power generating stations around Albuquerque is given by

$$I = \frac{P}{\pi * \boldsymbol{r^2}} \tag{5.10}$$

where *I* is the proportional power, *P* is the initial power, and *r* is the distance from the surface of the Earth to the ionosphere, determined to be around 78 km. Two power stations with high generating capacities of 156×10^6 W each and three with low capacities for a total of 34.8×10^6 W produces a total of ~347.4 MW. The proportional power transferred to the ionosphere above Albuquerque is 0.018 W/m^2.

5.4 Discussion of LWA-1 and LWA-2 Spatial Imaging Results

The receiving antenna array functioned as a camera, with each antenna representing one pixel in the phase image; hence, the 256 antennas in the array represented 256 pixels in the phase image, which had sufficient spatial resolution to show many sets of ionospheric waves. These sets of waves were analyzed using Fourier imaging, which separated the sets of waves by their frequencies and wavevectors. The strongest set of peaks having a spatial frequency of 0.06 cycles/m with a wavelength of 16.667 m was chosen for analysis of its power using a capacitor model, which resulted in this set of waves having 14.7 W. Translation from the patch on the ionosphere where the measurement occurred to Albuquerque, the source of the waves**,** the power increased to 15.3 W, producing a power density of 0.018 W/m^2.

A calculation of the power density received by the ionosphere above Albuquerque produced from the total power of the local power generating stations was determined to be 0.018 W/m^2, which was in agreement with the experimentally measured value. This agreement may imply that the power being generated by our power generators and consumed by industry and our homes is not lost but captured by the Earth's ionosphere.

The experimentally measured power density from all 177 sets of waves was approximated to be 0.1 W/m^2, which still requires their sources to be determined and not provided in this study. In comparison to the solar constant of 1367 W/m^2, a power density of 0.1 W/m^2 is far less and may not significantly contribute to climate change even if it was linearly extrapolated to larger

metropolitan cities 30 times larger than Albuquerque, although its importance for understanding climate change warrants further investigation.

5.5 Conclusions

The SDR Earth Imager enables the measurement of the power of ionospheric waves from phase images generated using radio waves transmitted terrestrially through the atmosphere, reflected from the ionosphere, and then detected terrestrially by an antenna array. The most powerful set of waves found within the phase image was measured to have a power density of 0.018 W/m^2, which corresponded to the calculated power density of 0.018 W/m^2 produced by the local power generating stations around Albuquerque, the place of generation of this set of ionospheric waves.

5.6 Acknowledgments

Grants from the Natural Science and Engineering Research Council of Canada (NSERC) and the Support Program using LWA-1 and LWA-SV at the University of New Mexico have made this work possible. Support from Libya's Ministry of Higher Education and Scientific Research is gratefully appreciated.

Conflicts of Interest: The authors declare no conflict of interest.

5.7 Additional Information for Mathematical Models and Calculations

It is crucial to highlight that the published work, on which the rest of this chapter relies, does not contain section 5.7.

The purpose of this section is to provide additional information on a variety of subjects covered in chapter 5. This includes power station and transmission line losses, the mathematical model of a capacitor and voltage calculation, power of local disturbances, and temporal analysis of the size of waves on a Fourier image.

5.7.1 Mathematical Model Capacitor and Voltage Calculation

This section covers the relationship between electric power, voltage difference, and current, as well as the mathematical principles underlying capacitance.

Electric power in an electrical circuit can be determined by multiplying the difference in voltage (ΔV) across a component by the current (I) flowing through it. This relationship can be expressed as [125]:

Electric power = Voltage Difference x Current

Power = ΔV x I

The mathematical model of a capacitor is illustrated by the diagram (Figure 5.10), which depicts a parallel plate capacitor composed of two parallel metal plates separated by a distance (d). This capacitor has the ability to store electric charge and exhibits capacitance [126].

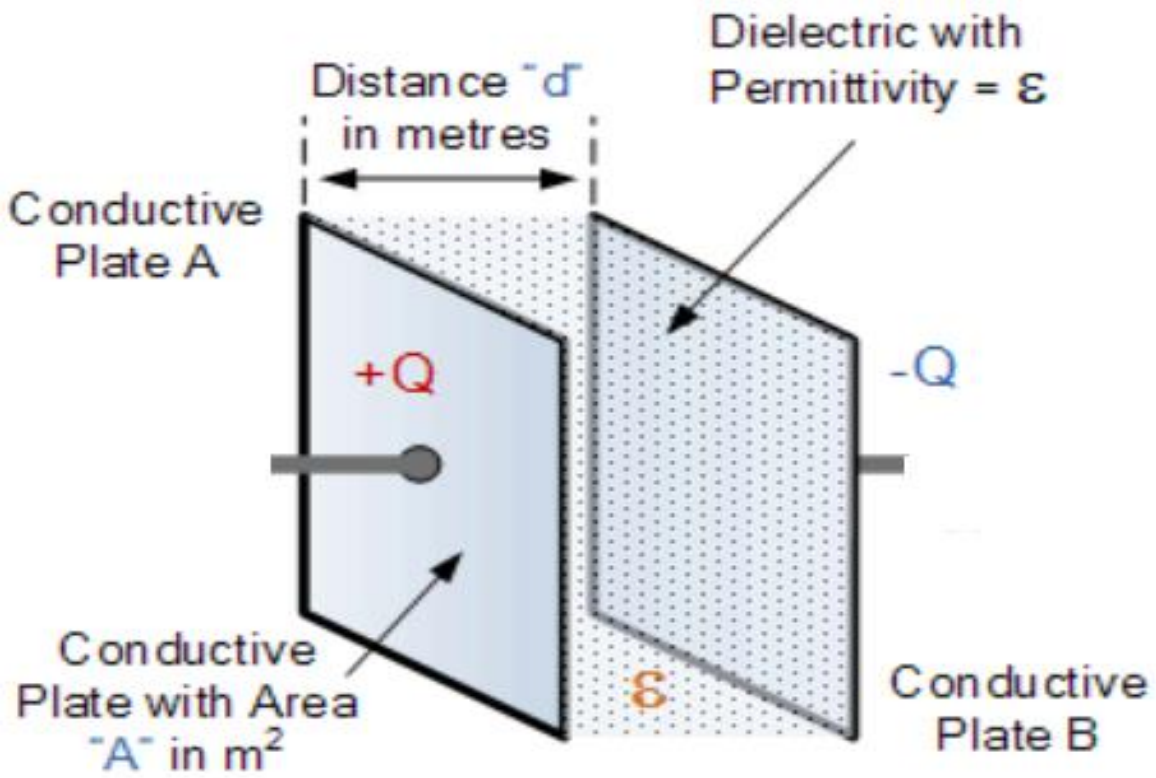

Figure 5.10 Capacitance of a Parallel Plate Capacitor *[127]*.

- Capacitance in Farads (C)

- Permittivity of dielectric ($\in_0$)
- Area of plate in square meters (A)
- Distance between plates in meters (d)

$$\Delta C = \frac{K * \in_0 * A}{\Delta d}$$

$$\Delta C = \frac{Q}{\Delta V}$$

The permittivity of a vacuum, $\in_0$, also known as the permittivity of free space, has the value of the constant 8.84 x 10^{-12} Farads per meter.

5.7.1.1 Determining Voltage from a Capacitor

The voltage from a capacitor can be determined by considering the size of the phase shift. The average amplitude of the phase shift at a spatial frequency of 0.06 cycles/m was found to be 8707 degrees, which can be converted to radians by multiplying it by π/180, resulting in 152 rad.

The number of cycles can be obtained by dividing the average phase shift in radians (152 rad) by 2π (rad), resulting in 24 cycles. The ionosphere phase shift (Δd) can then be calculated by multiplying the number of cycles (Δd_cycles) by the wavelength (λ) in meters. In this case, the ionosphere phase shift (Δd) is equal to 24 cycles multiplied by 16.667, resulting in 403 meters.

It is worth noting that the capacitance of a capacitor is defined as one Farad when one Coulomb of charge is stored on the plates by a voltage of one volt. The equation I=Q/t can be used to determine that 1 Ampere is equivalent to 1 Coulomb per second. This corresponds to approximately 6.25 x 10^{18} electrons. Additionally, it is stated that the ionosphere area is half the size of the area on Earth.

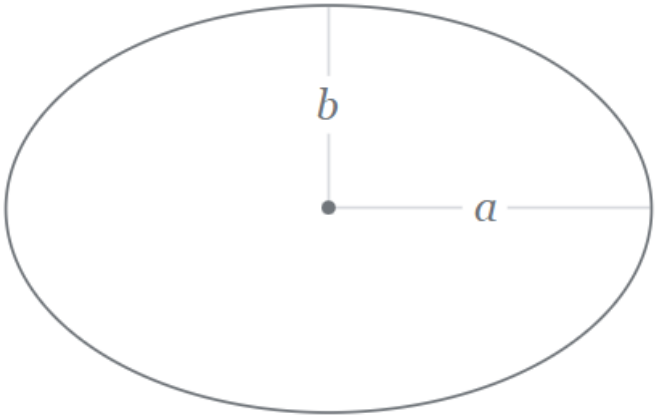

Figure 5.11 The area of the antenna array considered as Ellipse area

The following paragraph discusses various calculations and equations related to capacitance and electron density:

The constant K is set to 1, and the permittivity of free space (ε_0) is equal to 8.84 x 10^{-12} F/m. The area of the antenna array (A_t) considered as Ellipse ashown in Figure 5.11 is calculated as $\pi*(50/2)*(55/2)$, resulting in 2160 m^2. The phase shift (Δd) is determined to be 403 m. To calculate the change in capacitance (ΔC), the formula

($\Delta C = (K * \varepsilon_0 * A_t) / \Delta d$) is used. Substituting the given values, the change in capacitance is expressed as F (Farads).

In order to determine the maximum electron density, the formula $fc = 9\sqrt{Nmax}$ is utilized, where fc represents the critical frequency and Nmax indicates the maximum electron density per m^3. The equation $Nmax = (fc/9)^2$ is derived, and upon calculation, Nmax is found to be 3.5356 x 10^{11} electrons.

In a capacitor, capacitance is measured in farads, where one farad is equal to coulomb per volt (C/V). The change in capacitance (ΔC) is calculated to be 4.744 x 10^{-11} F, which can also be expressed as μF or μC/V.

By multiplying the change in capacitance (ΔC) by the approximate number of electrons (6.25 x 10^{18}), the value of ΔCe (change in charge per volt) is determined to be 296495858.242 e/V. The charge (Q) is given as 3.5356 x 10^{11} electrons. To calculate the voltage change (DV), the formula $DV = Q/\Delta Ce$ is used, where DV represents voltage per cubic meter. Substituting the values, DV is found to be 1192 V. Finally, the basic capacitance formula $Q = C * V$ is mentioned, which relates the capacitance (C) with the charge (Q) and the voltage (V) that creates the charge.

5.7.1.2 Current and Power Calculation

Current calculations can be derived from volume and power calculations by assuming the model is a half-cylinder. In this case, the radius (r) is equal to the lambda (λ) and the height (h) is equal to the change in distance (Δd). The volume of the half-cylinder can be calculated using the formula $V = (\pi * \lambda^2 * \Delta d) / 2$. By considering these parameters, the current can be determined based on the volume and power calculations.

The charge (Q) is given as 3.5356×10^{11} electrons. Additionally, Δd is calculated as half of 403, resulting in 201.5 m. The electron velocity (ve) is determined by multiplying λ by the number of cycles (30), resulting in 500 m/s. The time (t) is calculated as Δd divided by the electron velocity (L), resulting in 0.8 s. Using the formula Qt = Q/t, the average charge rate is calculated as 4.3855×10^{11} ele/s.

The power (P) can be found by using the formula P = V * I. The charge rate per Coulomb (Qt_col) is calculated by dividing Qt by the total number of electrons per Coulomb (6.25×10^{18}). This results in 1.403×10^{-7} col/s.

To calculate the current (I), Qt_col is multiplied by the volume, resulting in 0.0246 col/s. The power is obtained by multiplying I by the average voltage change (DV), which is 1192 V, resulting in 14.71 Watts. The area of the half-cylinder (A) is calculated as $\pi * (16.667)^2$, resulting in 872.69 m^2. The power density (S) is calculated by dividing the power (P) by the area (A), resulting in 0.0164 W/m^2.

5.7.1.3 Power of Local Disturbances

The power of local disturbances can be analyzed by considering various factors. The diagram illustrates the distance between the measurement location and the ionosphere area over Albuquerque. At the place of measurement, situated between LWA-SV and the transmitter, the power is recorded as 14.7 W. Damping (d(x)) is determined based on the Nepal earthquake, with a damping value of 0.173 per kilometer.

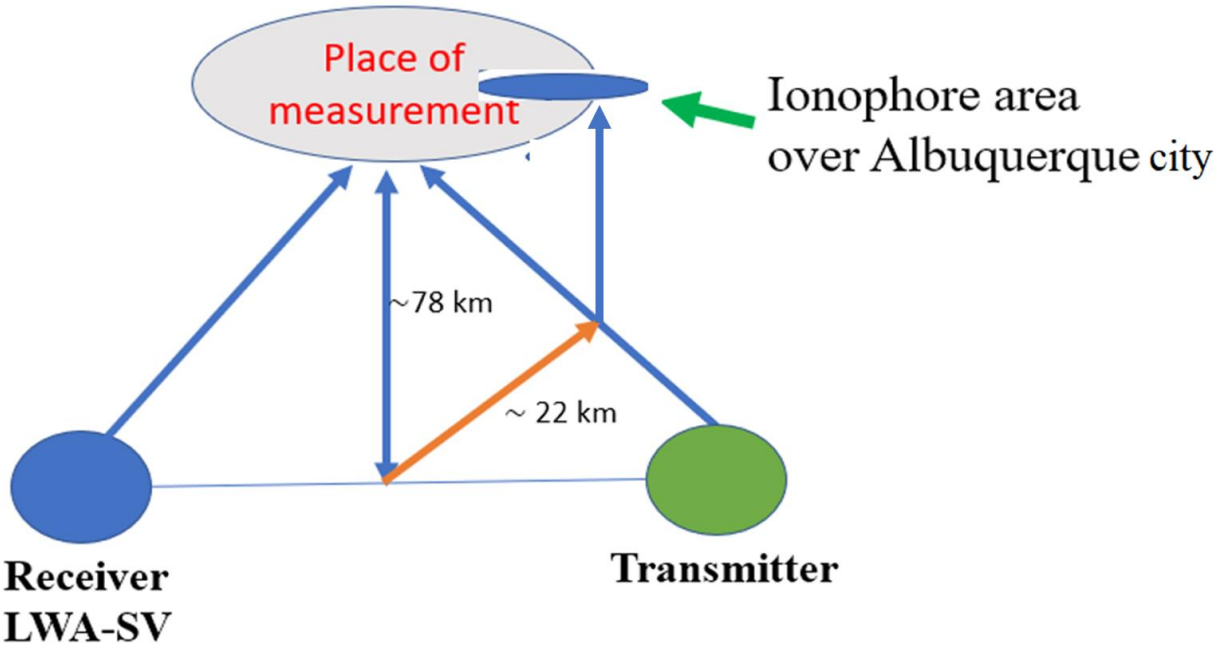

Figure 5.12 The diagram shows the height of the measurement location in the ionosphere

Considering a distance of 22 km (Figure 5.12) between the measurement location and Albuquerque, the power after damping is calculated as the product of the power and damping factor, resulting in 0.559 W. Thus, the power damping for a distance of 22 km is determined to be 0.5598 W. The total power of the disturbance source is calculated by adding the power measured at the place of measurement (14.7 W) and the power after damping (0.559 W), resulting in 15.26 W.

5.7.1.4 Power for Local Disturbances

The power for local disturbances can be calculated using the formula $I_p = P / (\pi * r^2)$, where I_p represents the proportional power of a wave, P represents the power of a wave, and r represents the radius of the wave. Applying this formula, the power of local disturbances is determined as follows:

$I_p = 15.26\ W / (\pi * (16.667)^2)$

$= 15.26\ W / (\pi * 277.79)$

$= 0.0174\ W/m^2$

It is commonly understood that any disturbances have a source as shown in Figure 5.13 and some properties can be used to distinguish these disturbances, such as their power, energy, and direction of movement.

Therefore, the power of local disturbances, calculated based on the given values, is found to be 0.0174 W/m^2. This value represents the proportional power of the wave in the specific situation being analyzed.

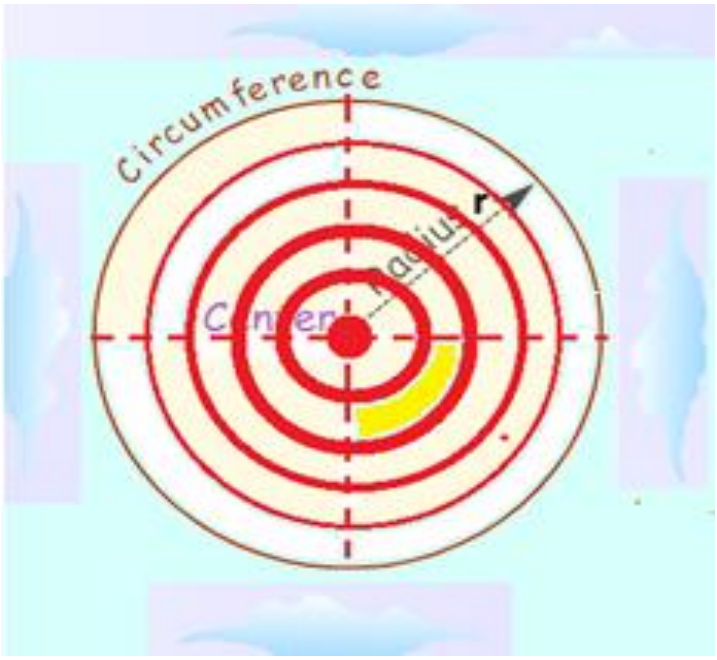

Figure 5.13 Power of local disturbances

The power of these waves was determined to be 14.7 W. At the source of the waves, the power is 15.3 W, as translated from the patch measured on the surface of the ionosphere layer to Albuquerque. This power produced a power density of all the sets of waves of 0.018 $\frac{W}{m^2}$ at Albuquerque city.

5.7.1.5 Power Station and Transmission Line Losses

Electricity transfer over long distances from power generating stations has several types of power losses. The transformers and the power lines are considered to have the largest power losses. The average values of power loss at various stages of transmission and distribution network are as follows. The first loss is at the step-up transformers from the power plant generator to the transmission line. It has a loss of 1-2%. The second loss is in the transmission line (s) having a loss of 2-4% and the third loss is the step-down transformers from the transmission line to the distribution network having a loss of 1-2% as shown in Figure 5.14. Thus, the distribution network transformers and cables have average total power losses of about

4- 6% [128], (International Electrotechnical Commission (IEC) Document) (1)(https://www.eia.gov/tools/faqs/faq.php?id=105&t=3). Another important consideration is the operation of all the power generators are synchronized, i.e., they are in phase with one another, having an alternating current (AC) of 60-Hertz over the complete interconnection [129].

This part discusses power capacity and losses in an electric transmission and distribution system, as well as the power remaining in the ionosphere.

Different power capacity and losses are taken into account in the schematic representation of an electric transmission and distribution system. The following are the capacity of power stations, expressed in megawatts (MW) [130], and the associated 6% losses:

- The first power plant has a capacity of 156 $\times 10^6$ W, and experiences loses 9,360,000.0 W.
- The second power plant has a capacity of 14.8 $\times 10^6$ W, and experiences loses 888,000.0 W.
- The third power plant has a capacity of 156.6 $\times 10^6$ W, and experiences loses 9,396,000.0 W.
- The fourth and fifth power plants have a capacity of 10 $\times 10^6$ W, and experience loses 600,000.0 W.

The total power losses in the system are calculated as 20,844,000.0 W. The radius of the wave is 78,000 m. Considering a coupling of 10%, the coupled power (Ic) is determined as 2,084,400.0 W. The remaining power (Ir) is obtained by subtracting Ic from P, resulting in 18,759,600.0 W.

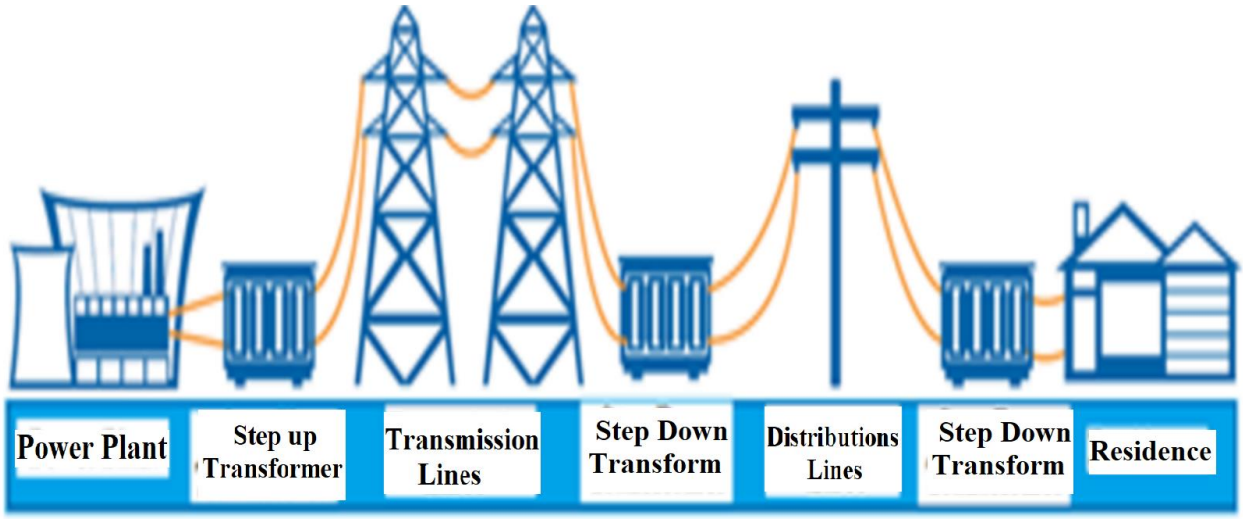

Figure 5.14 An electric transmission and distribution system is depicted in this simple schematic [131]

To calculate the proportional power of the wave (I), the formula $I = P / (\pi * r^2)$ is used, where P represents the power of the wave and r is the radius of the wave. Substituting the given values, I is

calculated as 0.000981 W/m^2. However, it is noted that the same damping factor cannot be applied in this case since this power is going from the Earth to the ionosphere.

The overall power is calculated to be 347.4 MW using the previously stated power capacity in megawatts. Utilizing the formula to calculate I, with the radius 78,000 m, I is found to be 0.0181 W/m^2. With a coupling of 10% (Ic = 0.00181 taken from the Nepal earthquake on April 2015), the power remaining in the ionosphere (I - Ic) is calculated as 0.0163 W/m^2, approximately equal to 0.016 W/m^2.

5.7.1.6 Temporal Analysis

The temporal analysis of the size of the wave on the Fourier image is presented in Appendix B. This analysis focuses on studying the variations and changes in the wave's size over time, as depicted in Figure 5.15.

5.7.1.6.1 Temporal analysis of Size of Wave on Fourier Image

A deep analysis of different time sequences shows that 32.55 hertz dominates all time sequences. These various frequencies exist because they are from interference effects due to the number of sources from all those power plants. Therefore, if they all act like a point source, their waves will interfere with each other, and they will create harmonics.

The radio wave emitted in Santa Fe the radio wave and reflected off the ionization layer at an angle. The detectors or the cameras (Antenna arrays: WA-SV and LWA-1) are on the other side of Albuquerque. The beam measured a patch on the surface of the ionization layer and tilted it as it reflected off the surface of that patch. And on that patch, all these waves are shown on the Fourier image. As the patch moves further away, the angle of the beam reflects off that patch becomes shallower and shallower. Therefore, waves of higher frequency can be seen. This is because the beam reflected off the surface of the ionization layer was tilted. That is why 32 and 64 appeared. If the reflected beam were straight up and down, we would expect 30 and 60 hertz.

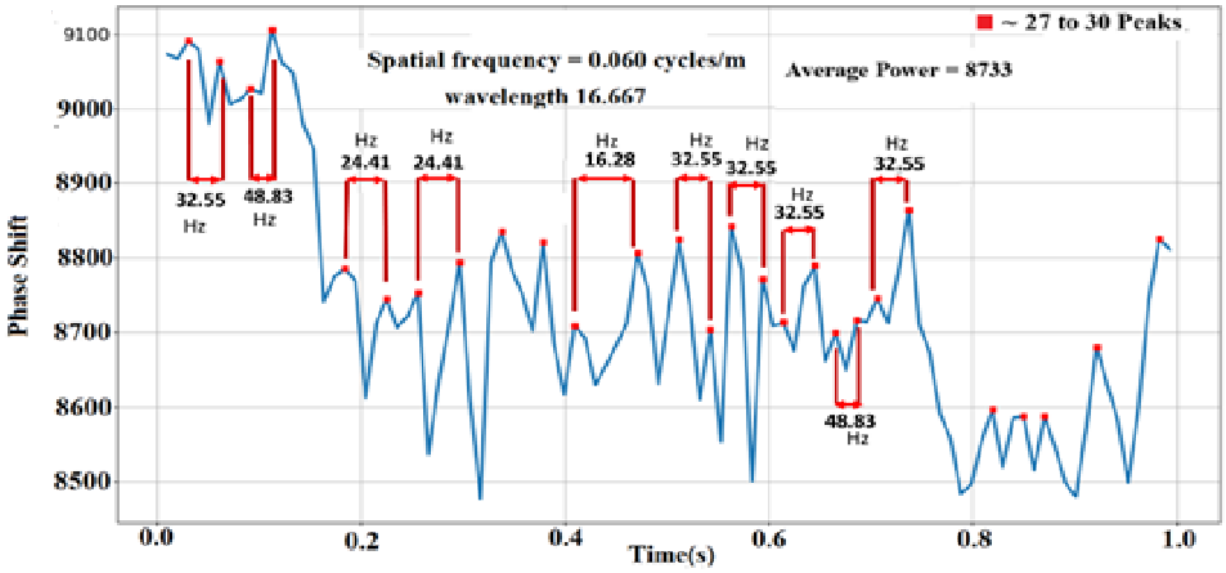

Figure 5.15 Power in Fourier image in one second illustrating the repetition of the frequency

The other complicating factor is that many sources can interact with these radios for disturbance and are close to each other. The disturbances are the power generators. They are all around Albuquerque, and Albuquerque itself is a big disturbance. Hence, a multi-source generation of these waves creates these other possible higher frequencies through interference.

Chapter 6 Conclusions and Future Work

6.1 Conclusions

The primary objective of this research is to focus on imaging ionospheric waves and relating them to the physically disturbing events that created them. These events could occur within the Earth's atmosphere, its mantle, and from space. Investigation of the amplitude, frequency, and wave vectors of the ionization surface waves provides a means to measure the properties of the Earth's disturbing events, such as their power, energy, location, and direction of movement.

The first experiments were conducted at DROA to attempt to image the ionosphere with The SDR Earth Imaging Device. The data was successfully gathered using only four receiving antennas. The results of the data analysis revealed two unique wave types: one with a constant frequency anticipating the loss of power in transmission lines and the other with a significant frequency spike that might correspond to earthquakes or lightning, as shown in chapter 3.

Chapter 4 illustrates that wavevectors for stations LWA-1 and LWA-SV were successfully applied to determine the intersection of wavevectors. The data analysis from the LWA-SV and LWA-1 stations showed that the wavevector of the strongest wave in one set, with 0.06 cycle/m, was tracked through time. The local power plants in and around Albuquerque are the most likely causes of this sequence of waves. Therefore, further research focused on identifying the wave vectors connecting the strength of the ionosphere waves to regional disturbances like the power generators in the Albuquerque area.

6.2 Future Work

The study conducted using the Software Defined Radio Earth Imager uncovered numerous waves in the ionosphere. This pioneering approach facilitates the determination of amplitudes, frequencies, and the origin of any disturbance caused by wave vectors. Nevertheless, based on the previous analysis and results, this research can be further improved and utilized by implementing the following enhancements:

Ideally, three or more SDR Earth Imagers would enable the precise localization of Earth's atmosphere-disturbing events by triangulating wave vectors Monitoring and measuring the disruptive occurrences of solar, geomagnetic, and meteorological Earth by using the device for

several days enable data analysis that could aid in comprehending each event's behavior.Conducting more measurements and then analyzing data for about 170 waves on a Fourier image could determine the power, energy, and location of Earth's disruptive events such as earthquakes, storms, and extreme local and global weather

Utilizing radio wave measurements of amplitudes, frequencies, and wave vectors of the waves present on the Earth's ionization layer or ionosphere can determine the Earth's refractive index from the surface to the upper atmosphere, providing a measurement of the temperatures, pressures, and compositions of the atmosphere.

In future measurements, it is hoped that techniques will be developed to enable the simultaneous measurement of the transmission time and received times at the antennas. This will facilitate the accurate determination of the reflection height of radio waves within the ionosphere. Furthermore, through the optimal alignment of the antenna array, it is anticipated that clearer ionospheric waves will be obtained, thereby contributing to the advancement of our understanding of this phenomenon.

Appendix

Appendix C provides further data related to the patent discussed in Chapter 4, author contributions, funding and data availability in Chapter 5.

Additional information, Chapter 4

Patent No: US 10,451,731 B2. Date: 22 October 2019. A Software Defined Radio Earth Atmosphere Imaging system with at least one imager that includes: a radio wave emitter configured to emit a sky wave, a ground wave, and a first line signal; radio wave detectors, including a radio wave detector with a two-dimensional array of radio wave receivers and a radio wave detector for receiving a carrier wave and a ground wave and transmitting a second-time signal; a vector network analyzer, including a Global Navigation Satellite System and at least one synchronization clock; a vector network analyzer in electrical communication with the radio emitter via a first wire and with the radio wave detector via a second wire with the wires used to transmit time signals; a software-defined radio in electronic communication with a vector network analyzer; and a computing device in electronic communication with the vector network analyzer.

Author Contributions: R.N.K.S. and R.H. are the main contributors to this research as they applied the idea, followed it up, and analyzed the dataset using a phase imager. P.D. is responsible for setting the time to conduct the experiments and designing the SDR. S.G.T. discussed the approach with us and the derivation of imaging the waves in the ionosphere. The concept of the approach was employed at Dominion Radio Astrophysical Observatory, Penticton, Canada under the supervision of S.H. Finally; all experiments were conducted by W.J. All authors have read and agreed to the published version of the manuscript.

Funding: Natural Science and Engineering Research Council (NSERC) of Canada (RGPIN-2017-03805), and the Ministry of Higher Education and Scientific Research of Libya scholarship.

Data Availability Statement: The dataset is available on Compute Canada Stores.

Acknowledgments: Grants from the Natural Science and Engineering Research Council (NSERC) of Canada, the opportunity to participate in the User Support Program of LWA-1 and LWA-SV at the University of New Mexico are gratefully appreciated. Thank the Ministry of Higher Education and Scientific Research of Libya for their support.

Conflicts of Interest: The authors declare no conflict of interest. We declare that we have no known competing financial interests or personal relationships that could have appeared to influence the work reported in this paper.

Additional information, Chapter 5

Author Contributions: Conceptualization, R.A.H; methodology, R.N.K.S; software, R.N.K.S and R.A.H; validation, R.N.K.S; formal analysis, R.N.K.S investigation, R.N.K.S; resources, R.A.H; data curation, R.N.K.S; writing—original draft preparation, R.A.H; writing—review and editing, R.N.K.S and R.A.H; visualization, R.A.H; supervision, R.A.H; project administration, R.A.H; funding acquisition, R.N.K.S. All authors have read and agreed to the published version of the manuscript.

Funding: Funding was obtained from the Natural Science and Engineering Research Council (NSERC) of Canada (RGPIN-2017-03805) and the Ministry of Higher Education and Scientific Research of Libya scholarship.

Data Availability Statement: The dataset is available on Compute Canada Stores.

Bibliography

[1] R. D. Hunsucker and J. K. Hargreaves, "Radio techniques for probing the ionosphere," in *The High-Latitude Ionosphere and its Effects on Radio Propagation*, Cambridge University Press, 2002, pp. 181–226. doi: 10.1017/CBO9780511535758.006.

[2] F. C. Judd, *Radio wave propagation:(HF bands); radio amateur's guide*. Heinemann, 1987.

[3] H. Rishbeth, "F-region links with the lower atmosphere?," *Journal of Atmospheric and Solar-Terrestrial Physics*, vol. 68, no. 3, pp. 469–478, Feb. 2006, doi: 10.1016/j.jastp.2005.03.017.

[4] R. A. Herring, K. McCaugherty, G. Odowichuk, and P. Driessen, "Software radio measurements of Earth atmosphere's refractive indices," in *Proceedings of 2011 IEEE Pacific Rim Conference on Communications, Computers and Signal Processing*, Victoria, BC, Canada: IEEE, Aug. 2011, pp. 815–817. doi: 10.1109/PACRIM.2011.6032999.

[5] T. Yamagami *et al.*, "Development of the highest altitude balloon," *Advances in Space Research*, vol. 33, no. 10, pp. 1653–1659, Jan. 2004, doi: 10.1016/j.asr.2003.09.047.

[6] X. Wang, D. Yang, D. Liu, and W. Chu, "Identifying a possible stratification phenomenon in ionospheric F2 layer using the data observed by the DEMETER satellite: method and results," *Ann. Geophys.*, vol. 37, no. 4, pp. 645–655, Jul. 2019, doi: 10.5194/angeo-37-645-2019.

[7] S. Pulinets, D. Ouzounov, A. Karelin, and D. Davidenko, "Lithosphere-Atmosphere-Ionosphere-Magnetosphere Coupling-A Concept for Pre-Earthquake Signals Generation," in *Geophysical Monograph Series*, D. Ouzounov, S. Pulinets, K. Hattori, and P. Taylor, Eds., Hoboken, NJ, USA: John Wiley & Sons, Inc., 2018, pp. 77–98. doi: 10.1002/9781119156949.ch6.

[8] J. F. Helmboldt *et al.*, "Passive all-sky imaging radar in the HF regime with WWV and the first station of the Long Wavelength Array," *Radio science*, vol. 48, no. 5, pp. 491–512, 2013, doi: 10.1002/rds.20056.

[9] R. Sharif, S. G. Tanyer, S. Harrison, P. Driessen, and R. Herring, "Monitoring Earth using SDR Earth Imager," *Journal of Atmospheric and Solar-Terrestrial Physics*, vol. 235, p. 105907, Sep. 2022, doi: 10.1016/j.jastp.2022.105907.

[10] R. Sharif, S. G. Tanyer, S. Harrison, W. Junor, P. Driessen, and R. Herring, "Locating Earth Disturbances Using the SDR Earth Imager," *Remote Sensing*, vol. 14, no. 24, Art. no. 24, Jan. 2022, doi: 10.3390/rs14246393.

[11] R. N. K. Sharif and R. A. Herring, "Measuring Power of Earth Disturbances Using Radio Wave Phase Imager," *Journal of Imaging*, vol. 9, no. 10, Art. no. 10, Oct. 2023, doi: 10.3390/jimaging9100228.

[12] G. Butcher, *Tour of the Electromagnetic Spectrum*. Government Printing Office, 2016.

[13] "LED Grow Light Spectrum & Charts: Full spectrum, white, and colored LEDs," 420 LED Guide. Accessed: May 30, 2023. [Online]. Available: https://www.420ledguide.com/led-grow-light-spectrum-charts-full-spectrum-white-and-colored-leds/

[14] J. Chum *et al.*, "Ionospheric signatures of the April 25, 2015 Nepal earthquake and the relative role of compression and advection for Doppler sounding of infrasound in the ionosphere," *Earth Planets Space*, vol. 68, no. 1, p. 24, Dec. 2016, doi: 10.1186/s40623-016-0401-9.

[15] "13.2 Wave Properties: Speed, Amplitude, Frequency, and Period - Physics | OpenStax." Accessed: Nov. 02, 2022. [Online]. Available: https://openstax.org/books/physics/pages/13-2-wave-properties-speed-amplitude-frequency-and-period

[16] S. Maharjan *et al.*, "Phase Unwrapping in Magnetic Resonance Elastography," *OJMI*, vol. 08, no. 04, pp. 111–125, 2018, doi: 10.4236/ojmi.2018.84014.

[17] W. Detmold, G. Kanwar, and M. L. Wagman, "Phase unwrapping and one-dimensional sign problems," *Physical review. D*, vol. 98, no. 7, pp. 074511-, 2018, doi: 10.1103/PhysRevD.98.074511.

[18] "The vertical structure of the atmosphere - PDF Free Download." Accessed: Apr. 25, 2023. [Online]. Available: https://docplayer.net/21470078-The-vertical-structure-of-the-atmosphere.html
[19] M. Moldwin, *An Introduction to Space Weather*. Cambridge: Cambridge University Press, 2008. doi: 10.1017/CBO9780511801365.
[20] B. Zolesi and L. R. Cander, "The General Structure of the Ionosphere," in *Ionospheric Prediction and Forecasting*, B. Zolesi and L. R. Cander, Eds., in Springer Geophysics. , Berlin, Heidelberg: Springer, 2014, pp. 11–48. doi: 10.1007/978-3-642-38430-1_2.
[21] A. RUSSELL, "The 'Kennelly-Heaviside' Layer," *Nature (London)*, vol. 116, no. 2921, pp. 609–609, 1925, doi: 10.1038/116609c0.
[22] E. V. APPLETON and M. A. F. BARNETT, "Local Reflection of Wireless Waves from the Upper Atmosphere," *Nature (London)*, vol. 115, no. 2888, pp. 333–334, 1925, doi: 10.1038/115333a0.
[23] K. Bibl, "Evolution of the ionosonde," *Annals of Geophysics*, vol. 41, no. 5–6, 1998, doi: 10.4401/ag-3810.
[24] S. Chapman, "Bakerian Lecture. Some Phenomena of the Upper Atmosphere," *Proceedings of the Royal Society A: Mathematical, Physical and Engineering Sciences*, vol. 132, no. 820, pp. 353–374, Aug. 1931, doi: 10.1098/rspa.1931.0105.
[25] H. W. NICHOLS and J. C. SCHELLENG, "The Propagation of Radio Waves over the Earth," *Nature (London)*, vol. 115, no. 2888, pp. 334–334, 1925, doi: 10.1038/115334a0.
[26] A. Ghasemi, A. Abedi, and F. Ghasemi, *Propagation Engineering in Wireless Communications*. New York, NY: Springer New York, 2012. doi: 10.1007/978-1-4614-1077-5.
[27] A. Saakian, *Radio Wave Propagation Fundamentals*. Norwood, UNITED STATES: Artech House, 2011. Accessed: May 29, 2023. [Online]. Available: http://ebookcentral.proquest.com/lib/uvic/detail.action?docID=1645674
[28] J. Dunder, "Principles of Radio Wave Propagation," p. 51.
[29] J. A. Richards, *Radio wave propagation an introduction for the non-specialist*. Berlin: Springer, 2008.
[30] A. Daniel, T. Woreta, and A. Teshager, "International Journal of Research Effect of Ionosphere on Radio Wave Propagation," May 2016.
[31] J. B. Andersen, "History of Communications/Radio Wave Propagation from Marconi to MIMO," *IEEE communications magazine*, vol. 55, no. 2, pp. 6–10, 2017, doi: 10.1109/MCOM.2017.7841460.
[32] "Antenna Theory - Terms in Wave Propagation." Accessed: Apr. 25, 2023. [Online]. Available: https://www.tutorialspoint.com/antenna_theory/antenna_theory_terms_in_wave_propagation.htm
[33] J. R. Machado-Fernández, "Software Defined Radio: Basic Principles and Applications/Software Defined Radio: Principios y aplicaciones básicas/Software Defined Radio: Princípios e Aplicações básicas," pp. 79–96, 2015, Accessed: Feb. 21, 2024. [Online]. Available: https://www.proquest.com/docview/1865436944?pq-origsite=primo
[34] J. J. Carr, "Chapter 16 - Radio Receiver Basics," in *The Technician's EMI Handbook*, J. J. Carr, Ed., Woburn: Newnes, 2000, pp. 163–195. doi: 10.1016/B978-075067233-7/50016-8.
[35] P. Cruz, H. Cravo Gomes, and N. Carvalho, "Receiver Front-End Architectures Analysis and Evaluation," 2010. doi: 10.5772/8744.
[36] Y.-I. Chen, J.-Y. Liu, Y.-B. Tsai, and C.-S. Chen, "Statistical Tests for Pre-earthquake Ionospheric Anomaly," *Terr. Atmos. Ocean. Sci.*, vol. 15, no. 3, p. 385, 2004, doi: 10.3319/TAO.2004.15.3.385(EP).
[37] A. Trigunait, M. Parrot, S. Pulinets, and F. Li, "Variations of the ionospheric electron density during the Bhuj seismic event," *Annales Geophysicae*, vol. 22, pp. 4123–4131, Dec. 2004, doi: 10.5194/angeo-22-4123-2004.
[38] S. A. Pulinets, T. B. Gaivoronska, A. L. Contreras, and L. Ciraolo, "Correlation analysis technique revealing ionospheric precursors of earthquakes," *Natural Hazards and Earth System Sciences*, vol. 4,

no. 5/6, pp. 697–702, Jan. 2004, Accessed: Jan. 12, 2022. [Online]. Available: http://www.nat-hazards-earth-syst-sci.net/4/697/2004/nhess-4-697-2004.pdf
[39] S. Pulinets and K. Boyarchuk, *Ionospheric precursors of earthquakes*. Berlin ; New York: Springer, 2004.
[40] W. Thatcher, "Strain accumulation on the northern San Andreas Fault Zone since 1906," *J. Geophys. Res.*, vol. 80, no. 35, pp. 4873–4880, Dec. 1975, doi: 10.1029/JB080i035p04873.
[41] V. P. Kim, V. V. Khegai, and P. V. Illich-Svitych, "On one possible ionospheric precursor of earthquakes," p. 4.
[42] S. Pulinets and D. Davidenko, "Ionospheric precursors of earthquakes and Global Electric Circuit," *Advances in Space Research*, vol. 53, no. 5, pp. 709–723, Mar. 2014, doi: 10.1016/j.asr.2013.12.035.
[43] R. G. Harrison, K. L. Aplin, and M. J. Rycroft, "Atmospheric electricity coupling between earthquake regions and the ionosphere," *Journal of Atmospheric and Solar-Terrestrial Physics*, vol. 72, no. 5–6, pp. 376–381, Apr. 2010, doi: 10.1016/j.jastp.2009.12.004.
[44] M. I. Karpov, O. V. Zolotov, and A. A. Namgaladze, "Modeling of the ionosphere response on the earthquake preparation," vol. 15, no. 2, p. 6, 2012.
[45] S. A. Pulinets, K. A. Boyarchuk, V. V. Hegai, and A. V. Karelin, "Conception and model of seismo-ionosphere-magnetosphere coupling," *Seismo-Electromagnetics: Lithosphere-Atmosphere-Ionosphere Coupling*, pp. 353–361, 2002, Accessed: Feb. 21, 2024. [Online]. Available: https://www.academia.edu/download/41891505/Conception_and_model_of_seismo-ionospher20160202-25639-j6bw2c.pdf
[46] P. E. Nikolopoulos D, "Electromagnetic Pre-earthquake Precursors: Mechanisms, Data and Models-A Review," *J Earth Sci Clim Change*, vol. 06, no. 01, 2015, doi: 10.4172/2157-7617.1000250.
[47] Y.-Y. Sun *et al.*, "Ionospheric F_2 region perturbed by the 25 April 2015 Nepal earthquake: IONOSPHERE PERTURBED BY NEPAL EARTHQUAKE," *J. Geophys. Res. Space Physics*, vol. 121, no. 6, pp. 5778–5784, Jun. 2016, doi: 10.1002/2015JA022280.
[48] S. Tulasi Ram, P. S. Sunil, M. Ravi Kumar, S. -Y. Su, L. C. Tsai, and C. H. Liu, "Coseismic Traveling Ionospheric Disturbances during the M_w 7.8 Gorkha, Nepal, Earthquake on 25 April 2015 From Ground and Spaceborne Observations," *J. Geophys. Res. Space Physics*, vol. 122, no. 10, p. 10,669-10,685, Oct. 2017, doi: 10.1002/2017JA023860.
[49] S. Dorbolo, N. Vandewalle, E. Reyssat, and D. Quéré, "Vita brevis of antibubbles," *Europhysics News*, vol. 37, no. 4, pp. 24–25, Jul. 2006, doi: 10.1051/epn:2006406.
[50] E. Astafyeva, "Ionospheric Detection of Natural Hazards," *Reviews of Geophysics*, vol. 57, no. 4, pp. 1265–1288, 2019, doi: 10.1029/2019RG000668.
[51] G. G. Bowman, "Some Effects of Nuclear Explosions on the Ionosphere," *Aust. J. Phys.*, vol. 15, no. 3, pp. 405–419, 1962, doi: 10.1071/ph620405.
[52] J. Laštovička, "Forcing of the ionosphere by waves from below," *Journal of Atmospheric and Solar-Terrestrial Physics*, vol. 68, no. 3–5, pp. 479–497, Feb. 2006, doi: 10.1016/j.jastp.2005.01.018.
[53] H. Rothkaehl *et al.*, "17 Ionospheric disturbances generated by different natural processes and by human activity in Earth plasma environment," p. 11.
[54] C. Zhang and Q. Ma, "Influences of radiation from terrestrial power sources on the ionosphere above China based on satellite observation," *IOP Conf. Ser.: Earth Environ. Sci.*, vol. 153, p. 042002, May 2018, doi: 10.1088/1755-1315/153/4/042002.
[55] M. Parrot and Y. Zaslavski, "Physical mechanisms of man-made influences on the magnetosphere," *Surv Geophys*, vol. 17, no. 1, pp. 67–100, Jan. 1996, doi: 10.1007/BF01904475.
[56] H. Volland, "Handbook of Atmospheric Electrodynamics: Volume II (1995)," p. 42.

[57] R. A. Helliwell, J. P. Katsufrakis, T. F. Bell, and R. Raghuram, "VLF line radiation in the Earth's magnetosphere and its association with power system radiation," *J. Geophys. Res.*, vol. 80, no. 31, pp. 4249–4258, Nov. 1975, doi: 10.1029/JA080i031p04249.

[58] J. P. Luette, C. G. Park, and R. A. Helliwell, "Longitudinal variations of very-low-frequency chorus activity in the magnetosphere: Evidence of excitation by electrical power transmission lines," *Geophys. Res. Lett.*, vol. 4, no. 7, pp. 275–278, Jul. 1977, doi: 10.1029/GL004i007p00275.

[59] C. G. Park and T. R. Miller, "Sunday decreases in magnetospheric VLF wave activity," *J. Geophys. Res.*, vol. 84, no. A3, p. 943, 1979, doi: 10.1029/JA084iA03p00943.

[60] J. P. Matthews and K. Yearby, "Magnetospheric VLF line radiation observed at Halley, Antarctica," *Planetary and Space Science*, vol. 29, no. 1, pp. 97–106, Jan. 1981, doi: 10.1016/0032-0633(81)90142-2.

[61] R. A. Helliwell, "POWER LINE RADIATION IN THE MAGNETOSPHERE," p. 15.

[62] K. Bullough, A. R. L. Tatnall, and M. Denby, "Man-made e.l.f./v.l.f. emissions and the radiation belts," vol. 260, p. 3, 1976.

[63] O. Molchanov and M. Parrot, "PLHR emissions observed on satellites," *Journal of Atmospheric and Terrestrial Physics*, vol. 57, no. 5, pp. 493–505, Apr. 1995, doi: 10.1016/0021-9169(94)00077-2.

[64] Y. Ando, M. Hayakawa, and O. A. Molchanov, "Theoretical analysis on the penetration of power line harmonic radiation into the ionosphere," *Radio Science*, vol. 37, no. 6, pp. 5-1-5–12, 2002, doi: 10.1029/2001RS002486.

[65] J. Wu, Q. Guo, X. Yan, and C. Zhang, "Theoretical Analysis on Affecting Factors of Power Line Harmonic Radiation," *IEEE Trans. Plasma Sci.*, vol. 47, no. 1, pp. 770–775, Jan. 2019, doi: 10.1109/TPS.2018.2865827.

[66] C. Zhang and Q. Ma, "Influences of radiation from terrestrial power sources on the ionosphere above China based on satellite observation," *IOP Conf. Ser.: Earth Environ. Sci.*, vol. 153, p. 042002, May 2018, doi: 10.1088/1755-1315/153/4/042002.

[67] "Ionosphere and Weather | Nature." Accessed: Nov. 23, 2021. [Online]. Available: https://www-nature-com.ezproxy.library.uvic.ca/articles/165038a0

[68] B. Zolesi and L. R. Cander, *Ionospheric Prediction and Forecasting*. Berlin, Heidelberg: Springer Berlin Heidelberg, 2014. doi: 10.1007/978-3-642-38430-1.

[69] S. Pulinets and K. Boyarchuk, Eds., "Ionospheric Precursors of Earthquakes as they are seen from the Ground and from Space," in *Ionospheric Precursors of Earthquakes*, Berlin, Heidelberg: Springer, 2005, pp. 49–88. doi: 10.1007/3-540-26468-X_2.

[70] H. Rothkaehl *et al.*, "Ionospheric disturbances generated by different natural processes and by human activity in Earth plasma environment," *Annals of geophysics*, vol. 47, no. 2-3 Sup., 2009, doi: 10.4401/ag-3295.

[71] K. Bullough, A. R. L. Tatnall, and M. Denby, "Man-made e.l.f./v.l.f. emissions and the radiation belts," *Nature*, vol. 260, no. 5550, pp. 401–403, Apr. 1976, doi: 10.1038/260401a0.

[72] J. B. Malins, K. S. Obenberger, G. B. Taylor, and J. Dowell, "Three-Dimensional Mapping of Lightning-Produced Ionospheric Reflections," *Radio Science*, vol. 54, no. 11, pp. 1129–1141, 2019, doi: 10.1029/2019RS006857.

[73] "FCCdata.org - powered by REC." Accessed: Aug. 12, 2023. [Online]. Available: https://fccdata.org/?canam=CKOR

[74] N. Bruce, S. Harrison, R. Herring, and P. Driessen, "Development of a phased-array ionospheric imaging system," IEEE, 2019, pp. 1–8. doi: 10.1109/PACRIM47961.2019.8985050.

[75] "Ionosonde," *Wikipedia*. Jul. 21, 2019. Accessed: Nov. 19, 2020. [Online]. Available: https://en.wikipedia.org/w/index.php?title=Ionosonde&oldid=907168976

[76] M. Piersanti *et al.*, "Magnetospheric–Ionospheric–Lithospheric Coupling Model. 1: Observations during the 5 August 2018 Bayan Earthquake," *Remote sensing (Basel, Switzerland)*, vol. 12, no. 20, pp. 3299-, 2020, doi: 10.3390/rs12203299.

[77] W. Li *et al.*, "Analysis of ionospheric disturbances associated with powerful cyclones in East Asia and North America," *Journal of Atmospheric and Solar-Terrestrial Physics*, vol. 161, pp. 43–54, Aug. 2017, doi: 10.1016/j.jastp.2017.06.012.

[78] S. Priyadarshi, J. Yang, M. Werner, and M. Kryza, "Ionospheric perturbations initiated due to the forest-fire over Greece as a consequence of lithosphere-atmosphere-ionosphere coupling," *Geomatics, Natural Hazards & Risk*, vol. 11, no. 1, pp. 2411–2430, Jan. 2020, doi: 10.1080/19475705.2020.1842810.

[79] J. W. Dungey, "Interplanetary Magnetic Field and the Auroral Zones," *Phys. Rev. Lett.*, vol. 6, no. 2, pp. 47–48, Jan. 1961, doi: 10.1103/PhysRevLett.6.47.

[80] J. Liu *et al.*, "Profiles of ionospheric storm-enhanced density during the 17 March 2015 great storm," *Journal of geophysical research. Space physics*, vol. 121, no. 1, pp. 727–744, 2016, doi: 10.1002/2015JA021832.

[81] W. Wang *et al.*, "Thermosphere and ionosphere response to subauroral polarization streams (SAPS): Model simulations," *Journal of Geophysical Research: Space Physics*, vol. 117, no. A7, 2012, doi: 10.1029/2012JA017656.

[82] S.-R. Zhang *et al.*, "Observations of ion-neutral coupling associated with strong electrodynamic disturbances during the 2015 St. Patrick's Day storm," *Journal of Geophysical Research: Space Physics*, vol. 122, no. 1, pp. 1314–1337, 2017, doi: 10.1002/2016JA023307.

[83] J. Liu *et al.*, "Solar flare effects in the Earth's magnetosphere," *Nat. Phys.*, vol. 17, no. 7, Art. no. 7, Jul. 2021, doi: 10.1038/s41567-021-01203-5.

[84] E. Aa *et al.*, "Pronounced Suppression and X-Pattern Merging of Equatorial Ionization Anomalies After the 2022 Tonga Volcano Eruption," *Journal of Geophysical Research: Space Physics*, vol. 127, no. 6, p. e2022JA030527, 2022, doi: 10.1029/2022JA030527.

[85] S.-R. Zhang *et al.*, "2022 Tonga Volcanic Eruption Induced Global Propagation of Ionospheric Disturbances via Lamb Waves," *Frontiers in Astronomy and Space Sciences*, vol. 9, 2022, Accessed: Nov. 21, 2022. [Online]. Available: https://www.frontiersin.org/articles/10.3389/fspas.2022.871275

[86] B. J. Harding *et al.*, "Impacts of the January 2022 Tonga Volcanic Eruption on the Ionospheric Dynamo: ICON-MIGHTI and Swarm Observations of Extreme Neutral Winds and Currents," *Geophysical Research Letters*, vol. 49, no. 9, p. e2022GL098577, 2022, doi: 10.1029/2022GL098577.

[87] D. R. Themens *et al.*, "Global Propagation of Ionospheric Disturbances Associated With the 2022 Tonga Volcanic Eruption," *Geophysical Research Letters*, vol. 49, no. 7, p. e2022GL098158, 2022, doi: 10.1029/2022GL098158.

[88] O. Pokhotelov, M. Parrot, E. Fedorov, V. Pilipenko, V. Surkov, and V. Gladychev, "Response of the ionosphere to natural and man-made acoustic sources," *Annales geophysicae (1988)*, vol. 13, no. 11, pp. 1197–1210, 1995, doi: 10.1007/s00585-995-1197-2.

[89] E. N. Fedorov, N. G. Mazur, V. A. Pilipenko, and V. V. Vakhnina, "Modeling ELF Electromagnetic Field in the Upper Ionosphere From Power Transmission Lines," *Radio Science*, vol. 55, no. 7, p. e2019RS006943, 2020, doi: 10.1029/2019RS006943.

[90] K. S. Obenberger, D. C. Bowman, and E. Dao, "Identification of Acoustic Wave Signatures in the Ionosphere From Conventional Surface Explosions Using MF/HF Doppler Sounding," *Radio Science*, vol. 57, no. 3, p. e2021RS007413, 2022, doi: 10.1029/2021RS007413.

[91] W. J. Burke, C. Y. Huang, F. A. Marcos, and J. O. Wise, "Interplanetary control of thermospheric densities during large magnetic storms," *Journal of Atmospheric and Solar-Terrestrial Physics*, vol. 69, no. 3, pp. 279–287, Mar. 2007, doi: 10.1016/j.jastp.2006.05.027.

[92] T. J. Fuller-Rowell, M. V. Codrescu, R. J. Moffett, and S. Quegan, "Response of the thermosphere and ionosphere to geomagnetic storms," *Journal of Geophysical Research: Space Physics*, vol. 99, no. A3, pp. 3893–3914, 1994, doi: 10.1029/93JA02015.

[93] C.-S. Huang, "Continuous penetration of the interplanetary electric field to the equatorial ionosphere over eight hours during intense geomagnetic storms," *Journal of Geophysical Research: Space Physics*, vol. 113, no. A11, 2008, doi: 10.1029/2008JA013588.

[94] G. Garipov, A. Grigoriev, B. Khrenov, P. Klimov, and M. Panasyuk, "High-Energy Transient Luminous Atmospheric Phenomena: The Potential Danger for Suborbital Flights," in *Extreme Events in Geospace*, Elsevier, 2018, pp. 473–490. doi: 10.1016/B978-0-12-812700-1.00019-4.

[95] S. S. Varghese, K. S. Obenberger, J. Dowell, and G. B. Taylor, "Detection of a Low-frequency Cosmic Radio Transient Using Two LWA Stations," *ApJ*, vol. 874, no. 2, p. 151, Apr. 2019, doi: 10.3847/1538-4357/ab07c6.

[96] "LWA - about," The Long WavelenThe Long Wavelength Array. Accessed: May 02, 2022. [Online]. Available: http://www.phys.unm.edu/~lwa/abouthome.html

[97] P. Henning *et al.*, "The First Station of the Long Wavelength Array," *arXiv:1009.0666 [astro-ph]*, Sep. 2010, Accessed: Nov. 09, 2021. [Online]. Available: http://arxiv.org/abs/1009.0666

[98] J. Dowell, D. Wood, K. Stovall, P. S. Ray, T. Clarke, and G. Taylor, "The Long Wavelength Array Software Library," *J. Astron. Instrum.*, vol. 01, no. 01, p. 1250006, Dec. 2012, doi: 10.1142/S2251171712500067.

[99] "Ionospheric Detection of Natural Hazards - Astafyeva - 2019 - Reviews of Geophysics - Wiley Online Library." Accessed: Mar. 13, 2022. [Online]. Available: https://agupubs-onlinelibrary-wiley-com.ezproxy.library.uvic.ca/doi/full/10.1029/2019RG000668

[100] E. N. Fedorov, N. G. Mazur, and V. A. Pilipenko, "Electromagnetic Response of the Mid-Latitude Ionosphere to Power Transmission Lines," *Journal of Geophysical Research: Space Physics*, vol. 126, no. 10, p. e2021JA029659, 2021, doi: 10.1029/2021JA029659.

[101] Y. Liu, C. Zhou, Q. Tang, G. Chen, and Z. Zhao, "Geomagnetic conjugate observations of ionospheric disturbances in response to a North Korean underground nuclear explosion on 3 September 2017," *Annales Geophysicae*, vol. 37, pp. 337–345, May 2019, doi: 10.5194/angeo-37-337-2019.

[102] G. Crowley, "Doppler radar studies of the Antarctic ionosphere.," Ph.D., University of Leicester, 1985. Accessed: Apr. 11, 2023. [Online]. Available: https://ethos.bl.uk/OrderDetails.do?uin=uk.bl.ethos.353168

[103] G. Crowley and I. W. McCrea, "A synoptic study of TIDs observed in the United Kingdom during the first WAGS campaign, October 10-18, 1985," *Radio science*, vol. 23, no. 6, pp. 905–917, 1988, doi: 10.1029/RS023i006p00905.

[104] G. Crowley and F. S. Rodrigues, "Characteristics of traveling ionospheric disturbances observed by the TIDDBIT sounder: TIDS FROM TIDDBIT SOUNDER," *Radio Sci.*, vol. 47, no. 4, Aug. 2012, doi: 10.1029/2011RS004959.

[105] G. Crowley, T. B. Jones, and J. R. Dudeney, "Comparison of short period TID morphologies in Antarctica during geomagnetically quiet and active intervals," *Journal of atmospheric and terrestrial physics*, vol. 49, no. 11, pp. 1155–1162, 1987, doi: 10.1016/0021-9169(87)90098-5.

[106] J. A. Waldock and T. B. Jones, "Source regions of medium scale travelling ionospheric disturbances observed at mid-latitudes," *Journal of atmospheric and terrestrial physics*, vol. 49, no. 2, pp. 105–114, 1987, doi: 10.1016/0021-9169(87)90044-4.

[107] J.-Y. Liu, C.-H. Chen, C.-H. Lin, H.-F. Tsai, C.-H. Chen, and M. Kamogawa, "Ionospheric disturbances triggered by the 11 March 2011 M 9.0 Tohoku earthquake: BRIEF REPORT," *Journal of Geophysical Research: Space Physics*, vol. 116, no. A6, p. n/a, 2011, doi: 10.1029/2011JA016761.

[108] T. Tsugawa *et al.*, "Ionospheric disturbances detected by GPS total electron content observation after the 2011 off the Pacific coast of Tohoku Earthquake," *Earth, Planets and Space*, vol. 63, no. 7, pp. 875–879, 2011, doi: 10.5047/eps.2011.06.035.
[109] M. Nishioka, T. Tsugawa, M. Kubota, and M. Ishii, "Concentric waves and short-period oscillations observed in the ionosphere after the 2013 Moore EF5 tornado: IONOSPHERIC WAVES AFTER THE EF5 TORNADO," *Geophysical research letters*, vol. 40, no. 21, pp. 5581–5586, 2013, doi: 10.1002/2013GL057963.
[110] G. Crowley and I. Azeem, "Chapter 23 - Extreme Ionospheric Storms and Their Effects on GPS Systems," in *Extreme Events in Geospace*, Elsevier Inc, 2018, pp. 555–586. doi: 10.1016/B978-0-12-812700-1.00023-6.
[111] S. Selman, "TRAVELING IONOSPHERIC DISTURBANCE (TIDs) CHARACTERISTICS ESTIMATION FROM GPS-TEC OVER ETHIOPIAN LONGITUDINAL SECTOR," Thesis, 2018. Accessed: Apr. 14, 2023. [Online]. Available: http://ir.bdu.edu.et//handle/123456789/9142
[112] X. Pi, A. J. Mannucci, U. J. Lindqwister, and C. M. Ho, "Monitoring of global ionospheric irregularities using the Worldwide GPS Network," *Geophysical research letters*, vol. 24, no. 18, pp. 2283–2286, 1997, doi: 10.1029/97GL02273.
[113] F. Dos Santos Prol, M. Hernández-Pajares, M. Tadeu de Assis Honorato Muella, and P. De Oliveira Camargo, "Tomographic Imaging of Ionospheric Plasma Bubbles Based on GNSS and Radio Occultation Measurements," *Remote Sensing*, vol. 10, no. 10, Art. no. 10, Oct. 2018, doi: 10.3390/rs10101529.
[114] G. Crowley *et al.*, "Analysis of traveling ionospheric disturbances (TIDs) in GPS TEC launched by the 2011 Tohoku earthquake," *Radio science*, vol. 51, no. 5, pp. 507–514, 2016, doi: 10.1002/2015RS005907.
[115] R. D. Hunsucker and J. K. Hargreaves, "Basic principles of the ionosphere," in *The High-Latitude Ionosphere and its Effects on Radio Propagation*, Cambridge University Press, 2002, pp. 1–60. doi: 10.1017/CBO9780511535758.003.
[116] C. O. Hines, "INTERNAL ATMOSPHERIC GRAVITY WAVES AT IONOSPHERIC HEIGHTS," *Canadian journal of physics*, vol. 38, no. 11, pp. 1441–1481, 1960, doi: 10.1139/p60-150.
[117] K. C. Yeh and C. H. Liu, "Acoustic-gravity waves in the upper atmosphere," *Rev. Geophys. Space Phys., v. 12, no. 2, pp. 193-216*, vol. 12, no. 2, pp. 193–216, 1974, doi: 10.1029/RG012i002p00193.
[118] S. H. Francis, "Global propagation of atmospheric gravity waves: A review," *Journal of atmospheric and terrestrial physics*, vol. 37, no. 6, p. 1011,IN9,1031-1030,IN9,1054, 1975, doi: 10.1016/0021-9169(75)90012-4.
[119] Etc and H. Volland, *Handbook of atmospheric electrodynamics. Volume I*. Bosa Roca: CRC Press, 1995.
[120] M. Parrot and Y. Zaslavski, "Physical mechanisms of man-made influences on the magnetosphere," *Surv Geophys*, vol. 17, no. 1, pp. 67–100, Jan. 1996, doi: 10.1007/BF01904475.
[121] R. A. Helliwell, J. P. Katsufrakis, T. F. Bell, and R. Raghuram, "VLF line radiation in the Earth's magnetosphere and its association with power system radiation," *Journal of Geophysical Research (1896-1977)*, vol. 80, no. 31, pp. 4249–4258, 1975, doi: 10.1029/JA080i031p04249.
[122] J. P. Matthews and K. Yearby, "Magnetospheric VLF line radiation observed at Halley, Antarctica," *Planetary and Space Science*, vol. 29, no. 1, pp. 97–106, Jan. 1981, doi: 10.1016/0032-0633(81)90142-2.
[123] J. P. Luette, C. G. Park, and R. A. Helliwell, "Longitudinal variations of very-low-frequency chorus activity in the magnetosphere: Evidence of excitation by electrical power transmission lines," *Geophysical Research Letters*, vol. 4, no. 7, pp. 275–278, 1977, doi: 10.1029/GL004i007p00275.
[124] C. G. Park and T. R. Miller, "Sunday decreases in magnetospheric VLF wave activity," *Journal of Geophysical Research: Space Physics*, vol. 84, no. A3, pp. 943–950, 1979, doi: 10.1029/JA084iA03p00943.

[125] confused_learner, "Power = Voltage x Current," Electrical Engineering Stack Exchange. Accessed: Dec. 19, 2023. [Online]. Available: https://electronics.stackexchange.com/q/586368
[126] pani, "Current-Voltage relationship in Capacitor," Electronics Tutorials. Accessed: Dec. 19, 2023. [Online]. Available: https://electronicspani.com/current-voltage-relationship-in-capacitor/
[127] W. Storr, "Introduction to Capacitors, Capacitance and Charge," Basic Electronics Tutorials. Accessed: Aug. 13, 2023. [Online]. Available: https://www.electronics-tutorials.ws/capacitor/cap_1.html
[128] P. Tallapragada V. S.N., M. Shkaratan, A. K. Izaguirre, J. Helleranta, S. Rahman, and S. Bergman, "Monitoring Performance of Electric Utilities : Indicators and Benchmarking in Sub-Saharan Africa," World Bank, Washington, DC, 2009. Accessed: Nov. 22, 2021. [Online]. Available: http://openknowledge.worldbank.org/handle/10986/13030
[129] National Research Council, National Academy of Engineering, National Academy of Sciences, Division on Engineering and Physical Sciences, and Committee on America's Energy Future, *America's Energy Future: Technology and Transformation*. Washington, D.C., UNITED STATES: National Academies Press, 2010. Accessed: Oct. 28, 2021. [Online]. Available: http://ebookcentral.proquest.com/lib/uvic/detail.action?docID=3378569
[130] J. Desjardins, "Mapped: Every Power Plant in the United States," Visual Capitalist. Accessed: Dec. 29, 2023. [Online]. Available: https://www.visualcapitalist.com/mapped-every-power-plant-in-the-united-states/
[131] Q. Alsafasfehh, "0. Reduce Losses in the Transmission and Distribution System", Accessed: Dec. 30, 2023. [Online]. Available: https://www.academia.edu/34621315/0_Reduce_Losses_in_the_Transmission_and_Distribution_System